12-2020

Optical Properties of Ultrathin In(Ga)As/GaAs and In(Ga)N/GaN Quantum Wells

Yurii Maidaniuk
University of Arkansas, Fayetteville

Optical Properties of Ultrathin In(Ga)As/GaAs and In(Ga)N/GaN Quantum Wells

A dissertation submitted in partial fulfillment
of the requirements for the degree of
Doctor of Philosophy in Microelectronics-Photonics

by

Yurii Maidaniuk
Taras Shevchenko National University of Kyiv
Bachelor of Science in Physics, 2011
Taras Shevchenko National University of Kyiv
Master of Science in Physics, 2014

December 2020
University of Arkansas

This dissertation is approved for recommendation to the Graduate Council.

Gregory Salamo, Ph.D.
Dissertation Director

Huaxiang Fu, Ph.D.
Committee Member

Min Zou, Ph.D.
Committee Member

Morgan Ware, Ph.D.
Committee Member

Rick Wise, Ph.D.
Ex-Officio Member

The following signatories attest that all software used in this dissertation was legally licensed for use by Yurii Maidaniuk for research purposes and publication.

Mr. Yurii Maidaniuk, Student	Dr. Gregory Salamo, Dissertation Director

This dissertation was submitted to http://www.turnitin.com for plagiarism review by the TurnItIn company's software. The signatories have examined the report on this dissertation that was returned by TurnItIn and attest that, in their opinion, the items highlighted by the software are incidental to common usage and are not plagiarized material.

Dr. Rick Wise, Program Director	Dr. Gregory Salamo, Dissertation Director

Abstract

Recently, structures based on ultrathin quantum wells (QWs) began to play a critical role in modern devices, such as lasers, solar cells, infrared photodetectors, and light-emitting diodes. However, due to the lack of understanding of the formation mechanism of ultrathin QWs during the capping process, scientists and engineers cannot fully explore the potential of such structures. This study aims to investigate how structural parameters of ultrathin QWs affect their emission properties by conducting a systematic analysis of the optical properties of In(Ga)As/GaAs and In(Ga)N/GaN ultrathin QWs. Specifically, the analysis involved photoluminescence measurements combined with effective bandgap simulation, x-ray diffraction, and transmission electron microscopy characterization. By controlling the growth temperature, indium content depth profile modifications were achieved for the In(Ga)As/GaAs QWs, leading to substantial changes in the emission properties. The analysis was supported by the effective bandgap simulation, which allowed not only to probe the exact shape of the indium depth profile but also to predict and design the structures with the desired optical characteristics. In the case of In(Ga)N/GaN ultrathin QWs, the growth temperature change affected the total indium incorporation within the QW. Further analysis suggested that the total amount of indium is the dominant factor when dealing with optical emission from ultrathin QWs. The ultimate goal of this research was to characterize, understand, and control ultrathin QW structures in various applications.

Acknowledgements

I would like to express my sincere gratitude and appreciation to many that offer help during my Ph.D. journey. First, I wish to thank my major professor, Dr. Salamo. I could never finish my dissertation without his support and guidance. Besides, I want to thank Dr. Wise for diligently going over my dissertation and all the constructive feedback. Last but not least, Dr. Mazur, not only serves as my research advisor but also as my mentor. I truly appreciate your wisdom and support during this five-year journey and wish our collaboration can last even after my graduation.

This research was financially supported by the Institute of Nanoscale Science and Engineering, University of Arkansas, and the National Science Foundation (NSF) (Grant No. 1809054).

Table of Contents

List of Figures

List of Tables

Chapter 1: Introduction

Over the past decades, researchers and engineers have been driven by the desire to better understand fundamental physical properties of structures exploiting quantum confinement effect as well as to develop more efficient novel devices based on such structures. At the present time, structures based on quantum wells (QW), quantum wires, and quantum dots are key components of a variety of devices including photodetectors [1], [2], light emitting diodes [3]–[5], lasers [6]–[10], and other optoelectronic applications. [11]–[15] In order to engineer high efficiency devices, one should make sure that all the components are developed with high accuracy. For instance, the small variation of QW thickness can potentially lead to a significant change in emission energy. Moreover, while the nominal QW thickness is getting smaller, the effect of fabrication errors becomes more noticeable. Consequently, any alterations from the nominal designed parameters for the edge case of one atomic layer (monolayer) QW thickness will have a huge impact on the desired properties of the system.

Recent advances in growth methods allows scientists to investigate physical properties of monolayer or sub-monolayer materials embedded in various semiconductors. [16]–[20] The structures based on embedding of sub-monolayers into the matrix show unique and useful properties as shown in the numerous sources from the past decade. [21]–[28] However, the optoelectronic properties of such systems are not well-understood because of the technical limitation of the analysis of such structures. [29]–[34] For example, by performing the content analysis of nominal 1 ML of InAs, one can use different methods including XRD and TEM characterization. Both methods rely on the smallest variations of the vertical lattice parameter from which the indium content can be estimated.

The InGaAs/GaAs quantum structures were thoroughly investigated in recent years. The

applications based on these structures include lasers,[35] solar cells,[36] and high electron mobility transistors.[37] Recently, a sub-monolayer (SML) quantum dot (QD) cascade mid-infrared photodetector was suggested as a promising replacement of the more matured QD-based devices.[27] One of the advantages of using SML growth is the complete absence of a wetting layer that is responsible for carrier trapping resulting in diminishing device performance.[28] However, the exact mechanism of indium agglomeration formation is not well-understood.[38] It is assumed that the islands with one monolayer height are formed during nominal sub-monolayer growth. According to numerous sources, these islands preserve their shape after being capped.[39], [40] Since the size of an island and distance between them is smaller than the exciton Bohr radius, the structure shows optical properties indistinguishable from an equivalent InGaAs quantum well (QW) with the same amount of indium.[41] On the contrary, lateral and vertical indium segregation must occur during the capping process as shown in recent works.[42], [43] In general, the segregation is one of the critical components in forming the composition profiles in thin layers of InGaAs.[44]

Given the importance of indium segregation on device performance, this process was widely studied both experimentally and theoretically.[45], [46] There are two most accepted models of indium segregation. The first theoretical model was proposed by Moison, et al.[47] in 1989. The foundation of their theory is the thermodynamical equilibrium. However, this model failed to explain experimental results that show increasing segregation with increasing growth temperature. The second empirical model was developed by Muraki, et al.[48] in 1992. Their photoluminescence (PL) and secondary ion mass spectrometry (SIMS) data show that the growth temperature is the primary component that determines the segregation level. In describing the indium concentration profile, the Muraki model provides better agreement with experimental

data and, therefore, is mostly used nowadays. The correctness of the given model was proved experimentally for the InGaAs/GaAs QWs with various growth conditions.[49]–[51]

As for the second part of the current study, the ultrathin InN/GaN QWs were investigated. Recently, the gallium nitride (GaN) based material is gaining popularity and beginning to play an important role in modern devices, such as high-frequency electronic circuit elements,[19] power supplies,[52] and optical emitters/detectors.[3], [17], [53]–[55] Admittedly, one of the drawbacks of the GaN-based devices is the high dislocation density.[54], [56]–[59] Nevertheless, such a drawback can be counteracted by the effective performance such as high carrier mobility and elevated radiative recombination rate.[22], [23], [60], [61] Given the importance of GaN material, the last part of this work mainly focuses on the optical properties of ultrathin indium nitride (InN) quantum wells that are embedded within a GaN matrix. Potentially, such incorporation allows engineers to cover all visible spectrum range given the special characteristics of GaN and InN materials. More specifically, GaN material has a wide bandgap, which equates to 3.4 eV at room temperature while the InN semiconductor has the relatively small band gap of 0.65 eV at room temperature. Therefore, InGaN/GaN device solutions theoretically allow engineers to cover all the visible spectrum range.[53], [56], [57] However, one possible challenge is the difference of temperature requirements for these two specific materials. The GaN material requires high temperature while the InN solution only grows at low temperature. One traditional way to deal with such difficulty is to use the intermediate temperature that falls between the range requirements for GaN and InN materials. However, such practice might lead to failure of the growth of InN of more than two monolayers (MLs). Hence, given the growth limitation of InN, ultrathin quantum wells were utilized as the study context with the goal of understanding how the changes of the growth temperature can

affect the emission properties of the studied structures. By using the photoluminescence, X-Ray Diffraction (XRD) technique, and Transmission Electron Microscope (TEM) analysis, it was found that the indium content within the quantum well can be effectively changed by only altering the growth temperature.[56] One avenue for future research is to explore ultrathin quantum wells based on other materials such as InAs/(Al)GaAs and GaN/AlN.[17], [18], [55], [62], [63] Moreover, the interest for this study also lies in understanding the electronic properties of an InN monolayer as the 2-D material given its increased popularity.[64], [65] The experimental results from a few research groups show that the maximum indium content in the one monolayer QW is limited to about 30%.[66]–[69] The exact mechanism of such limitation can include indium desorption, segregation, and In/Ga inter-diffusion.

The ultimate goal of this project is to characterize, understand, and control ultrathin multi quantum well devices for potential use in covering the green gap.[53] This study is motivated by the desire to convert the emission of GaN-based structures into the visible green area.

Chapter 2: Effective Bandgap Simulation

While analyzing the PL data, it is essential to be able to reconstruct structural characteristics of the system such as material content analysis and thicknesses of individual layers. The experimental data extracted from the PL are not sufficient to provide the information about important structural parameters. However, PL results, in combination with the energy bandgap simulation, provide a useful and non-destructive technique to quantitatively characterize the given structure with high accuracy.

This chapter focuses on basic a description of the effective bandgap calculations that were used throughout the entire project to confirm that designed growth parameters are matching with the actual ones or to provide the possible growth deviations that led to inconsistencies. Additionally, the simulation can be also applied at the design of structures stage in order to predict the growth parameters needed to meet specific requirements.

2.1 Regular QW vs. ultrathin QW

In order to explore the difference between the regular and the ultrathin QWs, the energy level and the corresponding wave function of the InAs/GaAs conduction band were calculated. The resulting energy diagram is shown in Figure 2.1. The conduction band offset was set to be equal to 0.6 eV. The effective mass was chosen to be equal $0.15 \cdot m_e$, as an average between the barrier (GaAs) and the QW (InAs). Admittedly, the QW thickness of 5 nm of InAs embedded in the GaAs matrix is not physically possible due to the critical thickness of 1.6 ML. However, the simulation was performed for the purpose of a demonstration and is sufficient to observe the difference between the regular and the ultrathin QWs.

By integrating the wave function over the GaAs barrier and InAs QW regions separately,

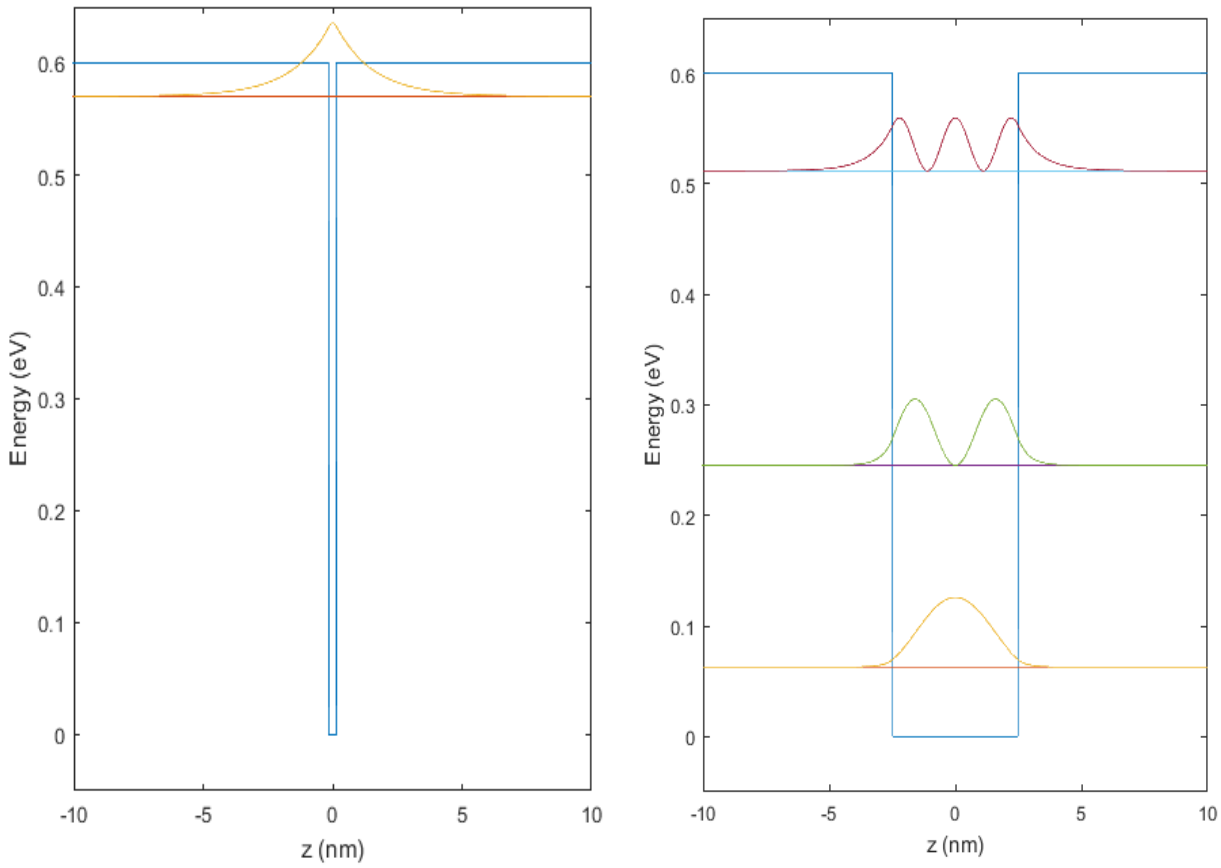

Figure 2.1. Energy band diagram with corresponding energy levels and wave functions plotted for (a) 1 ML and (b) 5 nm of InAs/GaAs quantum well.

it can be found that approximately 95% of the electrons are localized in the barrier in case of ultrathin QW. In contrast, over 97% of the electrons are localized within the QW, while considering its thickness to be more than 4 nm. Therefore, the overall quality of the barrier surrounding the QW plays the major role on the value of transition energy and emitting properties of the structure.

2.2. Numerical calculation of the effective bandgap with arbitrary profile of the potential energy

While trying to explain the PL results, it is often crucial to provide the modeled structure

that satisfy the experimental properties of the system. The modeling involves the solution of Schrodinger's equation with the structure related potential. One such model is Numerov's method for solving differential equation of the second order in general. The necessity of a numerical solution can be explained by the impossibility to find an analytical solution to Schrodinger's equation for most real potentials. Numerov's method is a well-suited technique for solving Schrodinger's equation since it provides a self-correlated approximation to the real solution while finding energy levels and wave functions simultaneously. The above explanation will become clearer after the exact mathematical description of the method followed by the example of the finite potential well.

Originally, the Numerov's method is a well-established technique for solving the differential equations of the form:

$$\frac{d^2\psi}{dx^2} = -f(x)\psi(x) \qquad \text{(Equation 2.1)}$$

In the case of time-independent Schrodinger's equation $f(x) = -\frac{2m(E-V(x))}{h^2}$, and $\psi(x)$ is the wave function corresponding to the certain discrete energy E. Approximating the second derivative as a small finite ratio and applying matrix notation, Schrodinger's equation can be rewritten as:

$$-\frac{2m}{h^2}B^{-1}A\psi + V\psi = E\psi \qquad \text{(Equation 2.2)}$$

where $A = (I_{-1} - 2I_0 + I_1)/d^2$, $B = (I_{-1} - 10I_0 + I_1)/12$, and $V = diag(V_1, V_2, ..., V_n)$.

Therefore, the problem was reintroduced in terms of matrix notation instead of a differential equation. The reason for such transformation lies within the architecture of numerical solutions performed on a computer. The validity of the described method can be

demonstrated by the example. Assuming a 10 nm GaN/AlN quantum well, one can build potential energy on a discrete coordinate grid from -40 nm to 40 nm along z-coordinate with a step-size of 0.02 nm resulting in a 4001 by 4001 Hamiltonian matrix dimension. Solving the eigenvalues problem for this matrix leads to the energy band diagram shown in Fig. 2.2.

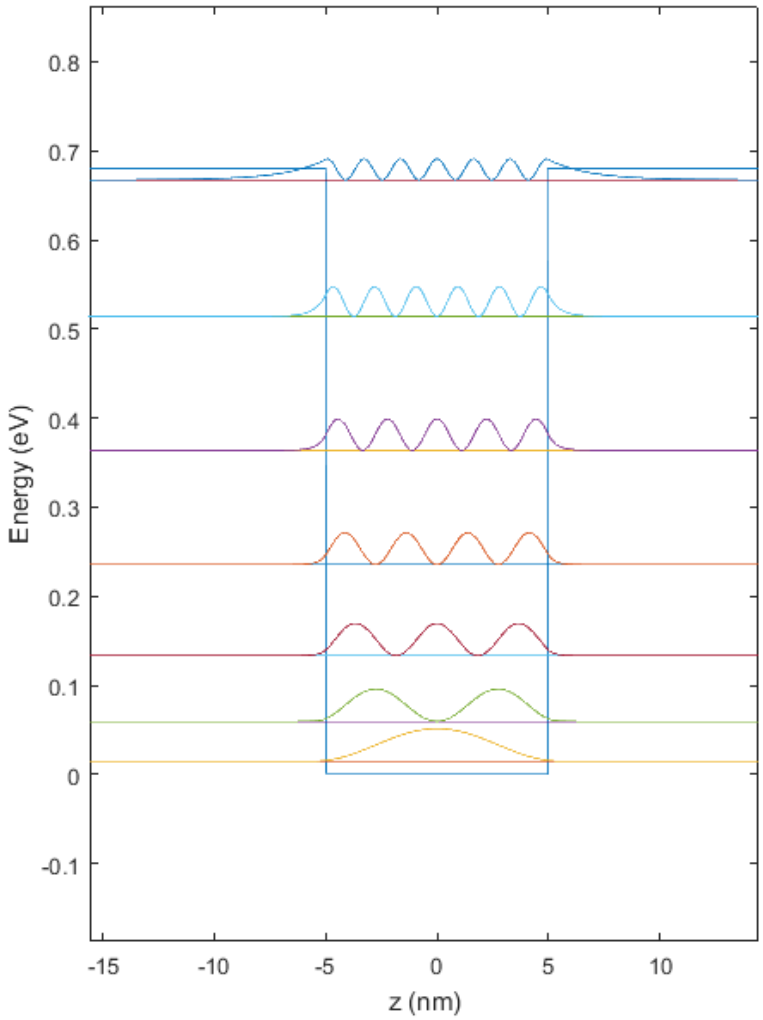

Figure 2.2. Energy band diagram with corresponding energy levels and wave functions plotted as a solution for the 10 nm GaN/AlN quantum well.

The actual matrix dimension for which eigen values must be found depends on the grid

accuracy. In other words, it is the smallest distance between two neighboring grid lines. The exact solution for the finite QW is a well-known problem that can be solved as follows. Considering the BenDaniel-Duke's boundary conditions, the full set of energy levels can be derived from the following equations:

$$\tan(k_A \frac{L}{2}) = \frac{m_A^*}{m_B^*}\frac{k_B}{k_A}, \text{ for the even states} \qquad \text{(Equation 2.3)}$$

$$-\cot(k_A \frac{L}{2}) = \frac{m_A^*}{m_B^*}\frac{k_B}{k_A}, \text{ for the odd states} \qquad \text{(Equation 2.4)}$$

where $k_A = \sqrt{\frac{2m_A^*}{h^2}E}$ is a wavenumber of the particle within the QW boundaries and L is the width of the QW. After simplifying the equations, substituting values for the GaN/AlN QW, and putting $x = k_A \frac{L}{2}$, the problem will reduce to finding the zeroes of the functions:

$$f(x) = 0.86\frac{\sqrt{89.24 - x^2}}{x} + \cot x \qquad \text{(Equation 2.5)}$$

$$g(x) = 0.86\frac{\sqrt{89.24 - x^2}}{x} - \tan x \qquad \text{(Equation 2.6)}$$

The intersection points are shown in Fig. 2.3 as open circles. From the figure, the intersections and the corresponding energy levels were obtained:

$$x = k_A \frac{L}{2} = 1.3986, 2.796, 4.1905, 5.5786, 6.9528, 8.2929, 9.4442$$

$$E_n = \frac{2h^2}{m_A^* L^2}x_n^2 \qquad \text{(Equation 2.7)}$$

The obtained intersection values can be used to determine the corresponding energy levels. Comparing the values of energy levels calculated by using two different numerical

approaches, the accuracy within 0.1% was obtained. This shows that Numerov's method provides sufficient accuracy and can be used for finding energy levels of QWs with more complex energy profiles. This method is already in-built into the software package, nextnano (München, Germany), that has been used to calculate energy band diagrams and corresponding energy levels/wave functions for different types of structures in this dissertation.

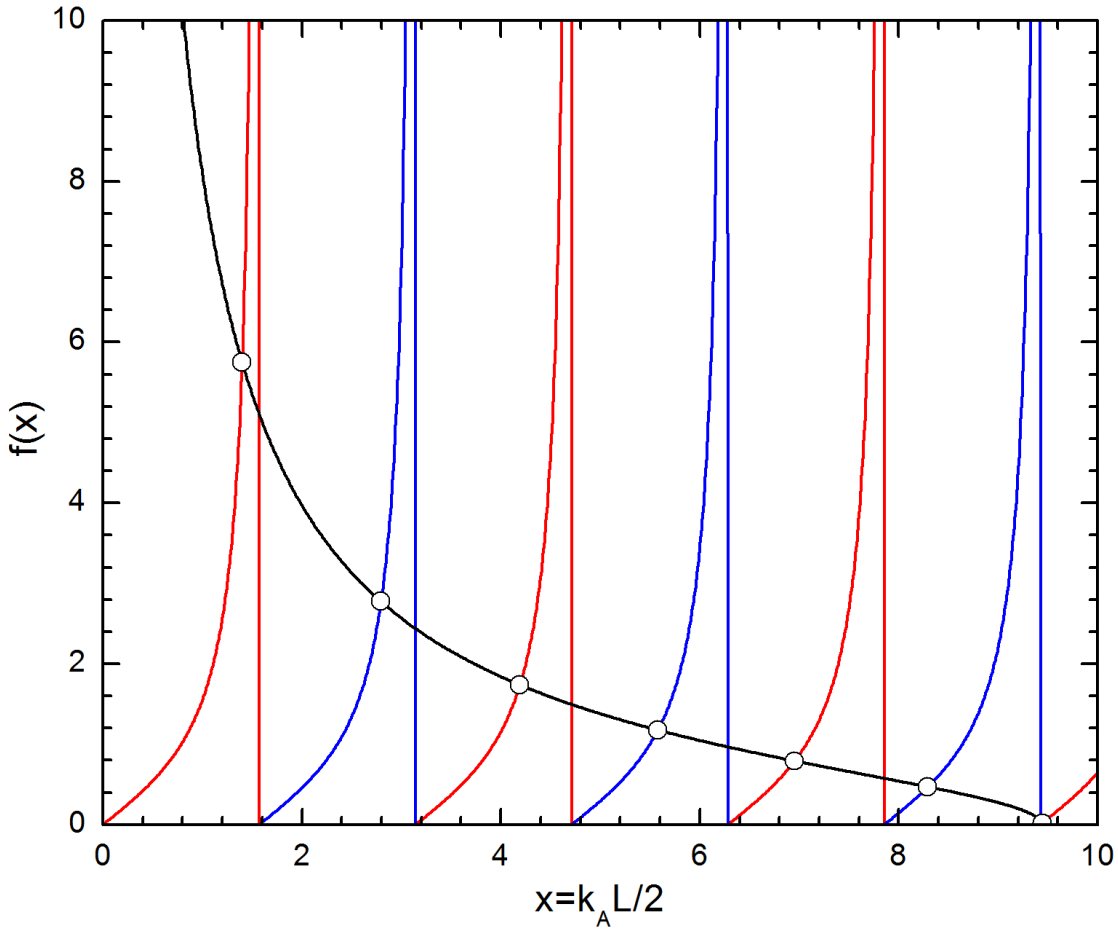

Figure 2.3. Numerical solution graph for the finite QW problem.

Chapter 3: Samples and Experimental Methods

3.1 Single monolayer In(Ga)As/GaAs QW: design and growth

For the in-depth analysis of formation of an ultrathin In(Ga)As single QW embedded into the GaAs matrix, a series of samples were grown. The structures were designed with the intention to provide the complete proof of the indium segregation during the GaAs capping process. Specifically, the thickness of QW was varied alongside with the indium content within the QW in order to maintain the total indium content on a constant level. Additionally, the thickness of the low temperature GaAs cap layer was varied for the separate structures which, ultimately, was introduced to present a possibility to control the indium segregation.

Samples were grown by a conventional MBE technique on semi-insulating GaAs (001) substrates. The typical common structure of the grown samples is shown in Fig. 3.1. The growth parameters for each sample are summarized in Table 3.1. At the start of the growth, the

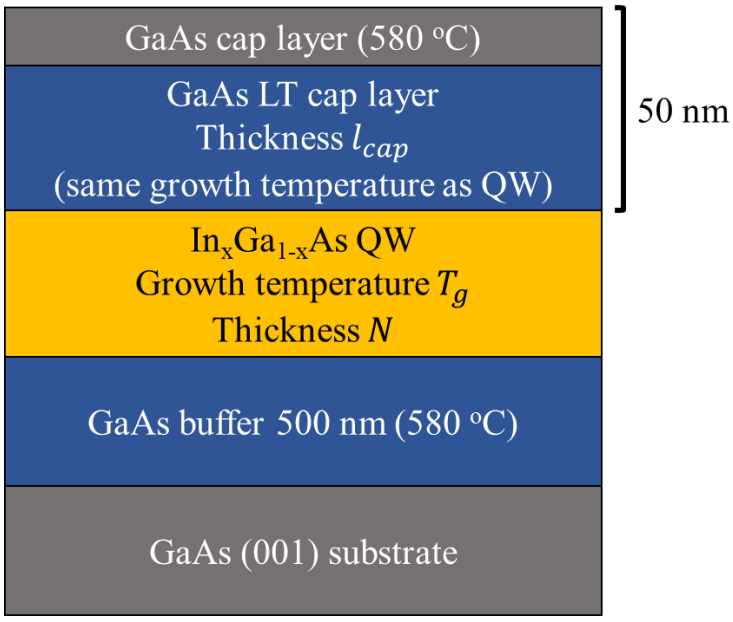

Figure 3.1. Schematic structure of GaAs-based ultrathin QW samples.

substrate was annealed at 600°C for 10 minutes under the presence of As_2 flux in order to remove the oxide layer on a substrate surface. Afterwards, a 500 nm thick GaAs buffer layer was deposited at the thermocouple temperature of 580 °C. Subsequently, the substrate temperature was decreased to T_g (temperature varied depending on the structure) for $In_xGa_{1-x}As$ QW deposition. As a result, the $In_xGa_{1-x}As$ single ultra-thin layer with thickness of N monolayers were deposited onto the smoothed buffer surface. After the deposition of QW, a 10 seconds growth interruption was introduced followed by a low-temperature (LT) cap layer of GaAs grown at T_g. The substrate temperature was then increased to 580 °C and a GaAs layer was grown. The total thickness of the GaAs cap layer (both low and high temperature) was nominally set to 50 nm.

Table 3.1. Growth conditions and design parameters of the GaAs-based samples used in the present work.

Sample ID	Indium composition (x_0)	$In_xGa_{1-x}As$ thickness, N (ML)	LT GaAs cap thickness, l_{cap} (ML)	$In_xGa_{1-x}As$ growth temperature, T_g (°C)
S1	1.0	1	35	460
S2	0.5	2	35	460
S3	0.33	3	35	460
S4	0.25	4	35	460
S5	1.0	1	35	380
S6	1.0	1	35	420
S7	1.0	1	4	460
S8	1.0	1	4	380
S9	1.0	1	4	420

3.2 RHEED analysis

Reflection high energy electron diffraction (RHEED) was used to monitor the growth in real time. This method can provide valuable information about the surface reconstruction during layer deposition. Whereas, surface reconstruction directly relates to the indium content in the topmost layer which, in fact, can be up to three top surface layers. Throughout the growth, a streaky RHEED pattern indicated that the two-dimensional (2D) growth was maintained.

Figure 3.2 shows a general RHEED intensity variation of specular reflection in [110] azimuthal direction during and after InAs growth on the GaAs (001) surface.

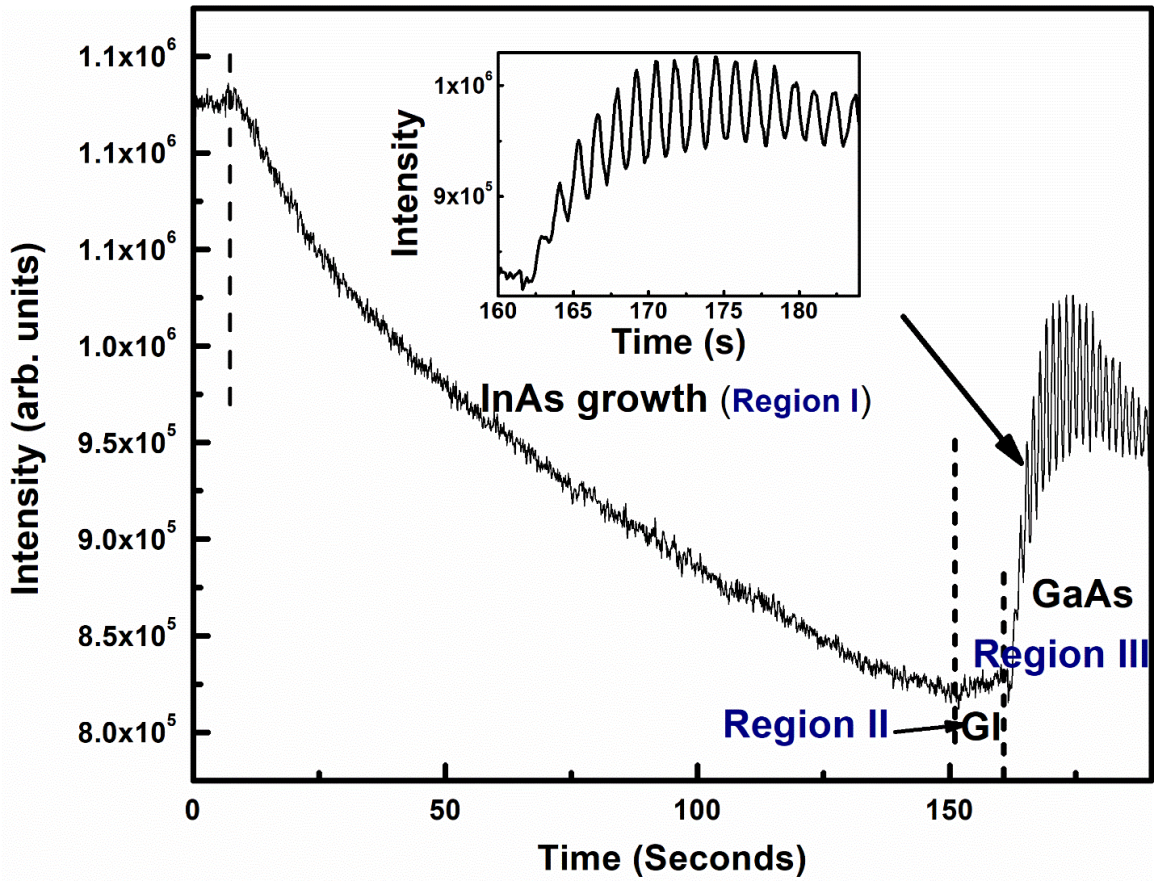

Figure 3.2. RHEED intensity variation of specular reflection in [110] azimuthal direction.

Region I represents the RHEED intensity decay during InAs growth on GaAs surface. The decaying behavior of RHEED intensity as opposed to normally observed oscillating pattern might lead to the following possible explanations:

- The surface reconstruction changed during InAs growth.
- InAs was not growing layer-by-layer. Instead, InAs islands formation is suggested.
- There was a presence of droplets or liquid form of indium on the growth surface.
- Reflectivity of electron beam for indium atoms on a InAs surface is not as strong as from Ga atoms on a GaAs surface.

Region II corresponds to the growth interruption period which lasted for ten seconds. The RHEED intensity slowly recovers in this region suggesting the surface recovery process was taking place. Region III shows the intensity oscillation during GaAs cap growth (inset in the figure shows this behavior). Intensity increased exponentially during the start of cap layer growth which shows the usual damping behavior due to growth front roughening.

3.3 Structural characterization of ultrathin In(Ga)As/GaAs samples

For successful simulation of any nanometer scale structures, the information about chemical profile and individual size of each layer is vital. As the size of quantum layers become smaller, a small deviation from the intended chemical and geometrical profiles can cause a large divergence from the desired physical properties of the system. From the device fabrication perspective, such structural inconsistencies must be minimized so that the negative effect on potential device performance could be diminished. The size and chemical inconsistency effects are especially strong when the size of the quantum system is comparable to the distance between atoms. Therefore, studying structural characteristics of ultrathin quantum active layers and their

effect on optical properties of the system was the main goal of current work. However, the physical size limitation of one atomic layer made the structural analysis of such structures challenging.

To directly observe and analyze structural properties of one monolayer InAs/GaAs QW, transmission electron microscopy (TEM) technique was used as a primary tool. This method not only allows the user to directly observe individual atoms in a particular crystalline orientation, but also to examine the quality of interfaces between QW and a barrier, measure the thicknesses of the key layers in the structure, and perform Fourier analysis to determine lattice parameter consistency.

All TEM related measurements were performed using a FEI (Hillsboro, Oregon) Titan 80-300 TEM with the addition of Cs-corrector (CEOS) and a Gatan (Pleasanton, California) Tridiem image filtering system. The whole TEM measurement procedure can be divided into three steps. The most tedious and time-consuming step is the TEM sample preparation. Having a well-prepared sample is 80% of success toward the best quality TEM image. Samples were prepared by gluing surface-to-surface two pieces of a sample following the standard mechanical polishing (the polishing planes were perpendicular to the surface of a sample to observe the whole grown structure in a cross-sectional view) to reach 20 μm in thickness. This step, however, requires precise mechanical manipulation since the sample at this stage is very fragile. The next step was the ion milling procedure performed on Fischione (Export, Pennsylvania) Ion Mill 1010. The low angle ($5 – 10^{o}$) Ar^{+} ion-milling allows one to reach 100 – 200 nm TEM suitable thickness. The energy of the ion beam was set in the optimal range to avoid thermal damage of the near-surface structure of interest. The prepared sample, then, was loaded into the TEM machine for further analysis. The mounting stage was cooled down by liquid nitrogen to

enable a cold trap mechanism for preventing main column contamination. The sample was bombarded by high energy (300 keV) electrons. The corresponding de Broglie wavelength for such high energy electrons is roughly equal to 0.02 Å. This wavelength makes it possible to observe structure features in extremely high resolution which is unreachable even for x-ray wavelengths. Another advantage of high energy electrons is the large penetration depth which enables the possibility to collect structural data from the large area of interest. Penetrating through the sample, the electrons lose part of their well-calibrated initial energy. The CCD camera is set to record the energy deviations and digitize them as the brightness variation in the image.

The mounted sample was oriented along the [110] crystallographic direction. At this orientation, the (001) and (111) family of planes become observable. Under mentioned conditions, the bright-field overview image of the sample with 1 ML InAs/GaAs QW is shown in Fig. 3.3.

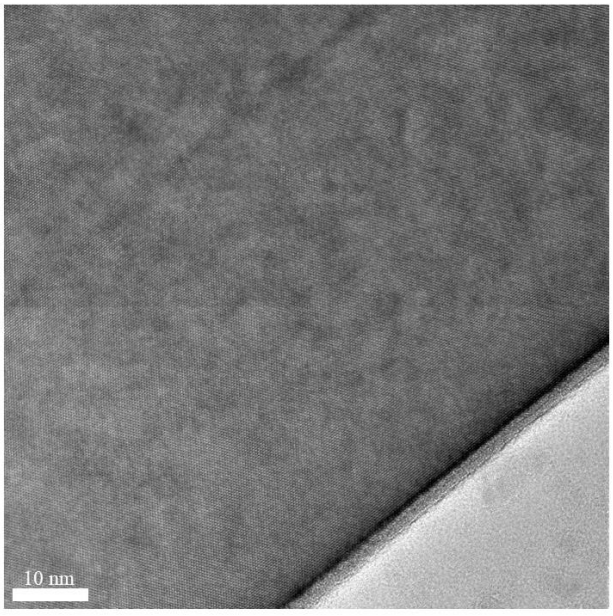

Figure 3.3. Cross-sectional TEM image of 1 ML InAs/GaAs QW sample.

The image contains visual information about the GaAs cap layer, which can be directly measured by using the calibrated scale. The GaAs cap layer thickness obtained from the TEM image is roughly equal to 48 nm. This confirms a well-calibrated GaAs growth rate since the intended cap thickness was set to 50 nm, which resulted in overall thickness accuracy of within 5%. Given the high growth rate of GaAs at 580 °C, the resulting GaAs cap thickness was within the acceptable range. The direct thickness measurement became possible due to the partially observable boundaries of InAs QW. Generally, under the perfectly focused condition, the contrast difference between the ultrathin InAs and GaAs layers is not sufficient to separate them without further image filtering. Therefore, the image above was recorded in under-focused condition which, however, suffered in terms of resolution.

In contrast, a cross-sectional in-focus TEM image of the region that contains the ultrathin InAs QW layer is shown in Fig. 3.4 (a). Even though each atom in the lattice is directly observable, it is impossible to determine the position of the InAs layer. To address this issue, the colored map of vertical lattice parameter was calculated as follows. First, the secondary image was generated using the Fourier filtering concentrating on the (002) family of planes. As the second step, the distances between all neighboring planes along the axis perpendicular to the InAs layer was calculated. The resulting matrix of distances was digitized as the color map shown in Fig. 3.4 (b). This map directly shows the trace of InAs layer in a red color as the increased distances between atomic planes (the lattice mismatch between InAs and GaAs is 7.2%). However, it is important to note that lattice distances map is not directly linked to the real indium redistribution within the QW region. In contrary, this map is associated with the strain field. Therefore, it can be concluded that the one monolayer of InAs/GaAs QW induces a strained region of 5 MLs thickness.

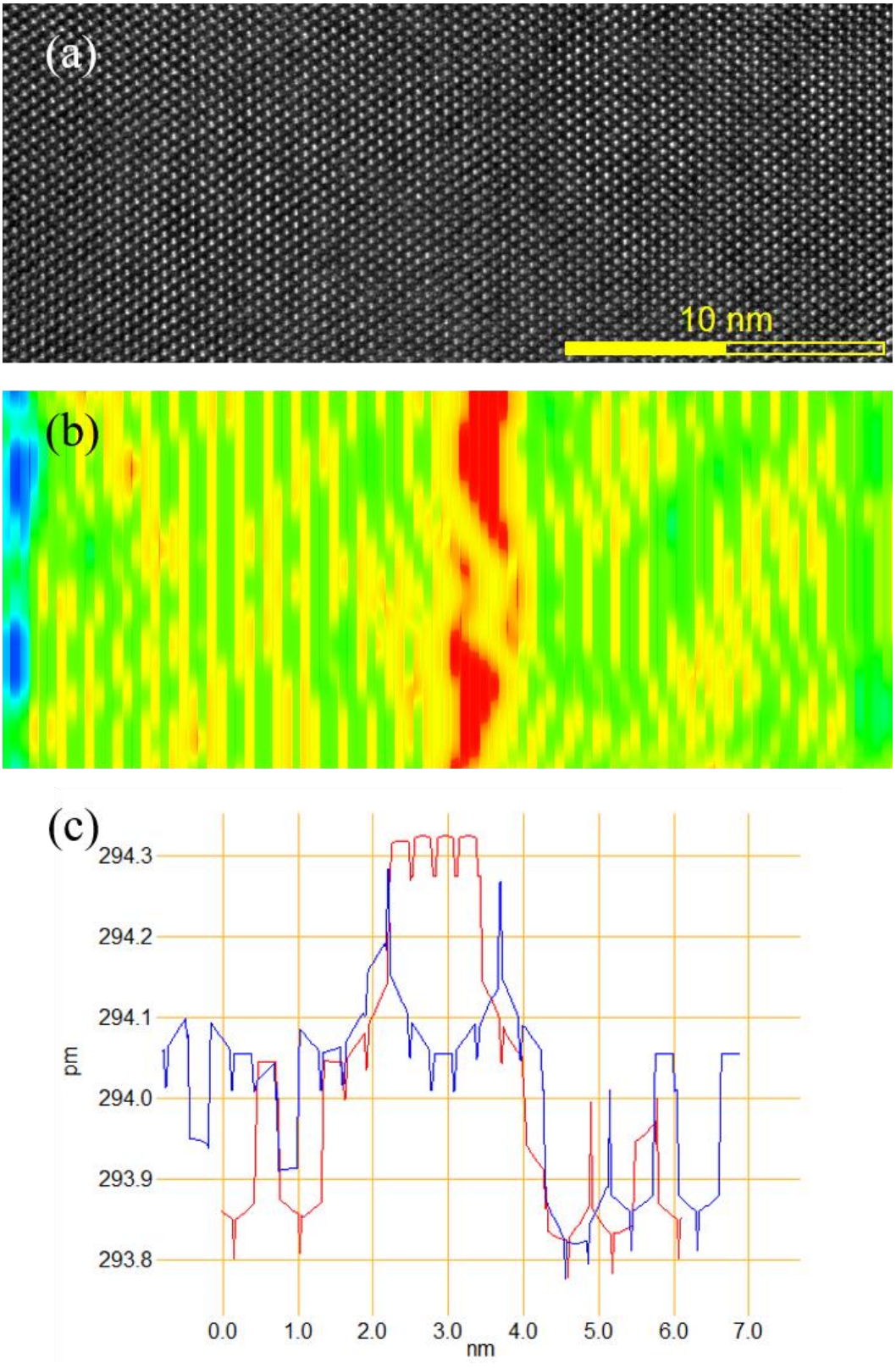

Figure 3.4. TEM data and analysis performed on 1 ML InAs/GaAs QW.

3.4 Continuous-wave (CW) PL measurement system for GaAs-based structures

All PL related measurements of the GaAs-based samples were performed on a custom-built PL setup which, for simplicity, is referred as PLS1. The schematic diagram of PLS1 is shown in Fig. 3.5. This system was used for intensity and temperature continuous wave PL

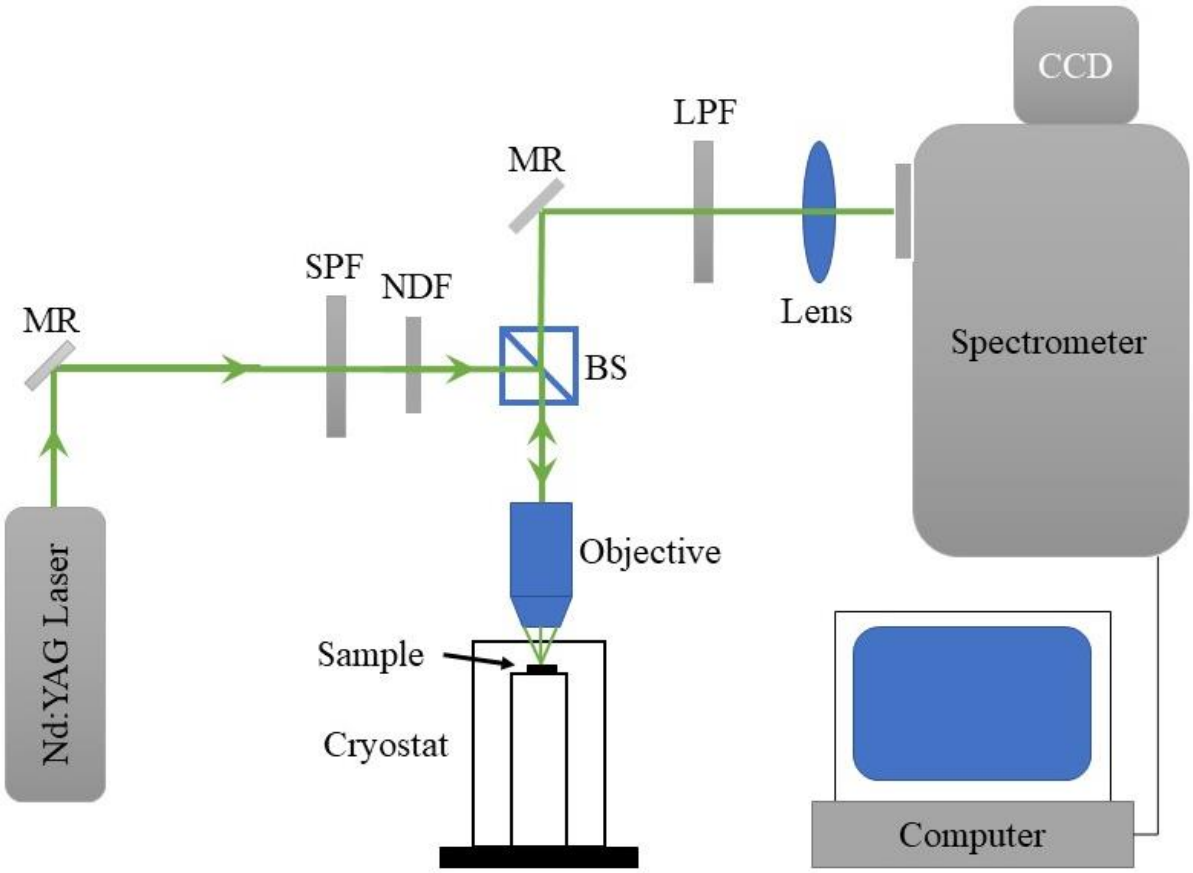

Figure 3.5. Schematic diagram of the experimental setup PLS1 used to perform PL measurements on GaAs-based structures.

measurements. The studied sample was attached by using thermal paste to the cold finger located inside the closed-cycle helium cryostat under a vacuum of 10^{-6} Torr. The cold finger was cooled by an APD Cryogenics (Shinagawa City, Tokyo, Japan) HC-4 MK2-1 Helium Compressor. The temperature was manipulated by a Lakeshore (Carson, California) 330 auto-

tuning temperature controller. As a result, the sample could reach and stabilize temperatures as low as 10 K and up to 300K (room temperature).

For PL excitation, a frequency-doubled 532 nm line of Nd:YAG (neodymium-doped yttrium aluminum garnet) laser (Coherent Verdi-V10) was used. The photon energy, which corresponds to the laser wavelength, was equal to 2.33 eV. This energy was sufficient to generate an electron-hole pair in bulk GaAs, which bandgap is equal to 1.518 eV at 10 K. The laser beam power was set to 200 mW. The beam from the laser was guided onto the short-pass filter (SPF) by the set of mirrors (MR). The purpose of this filter is to cut-off the part of spectra which is higher than 750 nm since the laser generates additional lines at 808 and 1064 nm. The following neutral density filter (NDF) serves as the laser beam intensity regulator. Fractional transmittance of each filter depends only on optical density D of a filter and calculated by formula:

$$\text{Fractional transmittance} = I / I_0 = 10^{-D}, \qquad \text{(Equation 3.1)}$$

where I_0 is the intensity before filter and I is the intensity after the filter. The set of ND filters allows the user to vary laser beam power over the range from 10^{-4} to 10^{2} mW. The beam-splitter (BS), following the filters, serves the purpose of guiding the beam through the 50x objective which focuses the beam on a surface of the studied sample. The resulting excitation spot size was about 20 μm. Such a tiny excitation spot made it possible to reach up to $3 \times 10^4 \frac{W}{cm^2}$ in power density (intensity). The sample holder could be moved in three degrees of freedom. The x- and y- movements in a plane perpendicular to the beam line allowed the user to control excitation spot position on a sample without adjusting other elements of the system. The z-movements served the purpose of finding the optimal focus plane of the objective and reaching the maximum excitation intensity.

The generated PL from the sample was collected by the same objective, passed through the beam-splitter, and directed onto the long-pass filter (LPF) with cut-on wavelength of 780 nm to remove the strong laser line from the spectrum. The following ND filters controlled the intensity of the incoming light to the spectrometer which prevented its saturation by decreasing incoming intensity.

The final element of PLS1 was a spectrometer. The light passing through the small slit fell on a parabolic mirror which collimated the light and directed it onto a diffraction grating. The diffraction grating, which acted as the dispersion element, spatially separated the wavelengths of the incoming light. The light then collected by a liquid nitrogen cooled InGaAs charge coupling device (CCD) array, which converted the incident photons into an electric signal. Finally, the digital spectrum was recorded by a software WinSpec32 for further analysis.

3.5 Time resolved PL measurement system

The PL carrier dynamics were studied in terms of time resolved PL measurements (TRPL). More specifically, carrier lifetime and excitation evolution were analyzed. The experimental setup is shown in Fig. 3.6. Generally, PLS1 and TRPL setup are very similar. The major differences between these two systems are the excitation and detection. For the excitation, Ti:Sapphire laser optically pumped by Coherent (Santa Clara, California) Verdi-V10 laser was used in a pulse mode (mode-locked regime). The excitation wavelength was set to 750 nm. By default, the laser generates two picosecond pulses with 76 MHz frequency.

3.6 Continuous-wave (CW) PL measurement system for GaN-based structures

Photoluminescence from GaN-based materials was studied on a different setup named

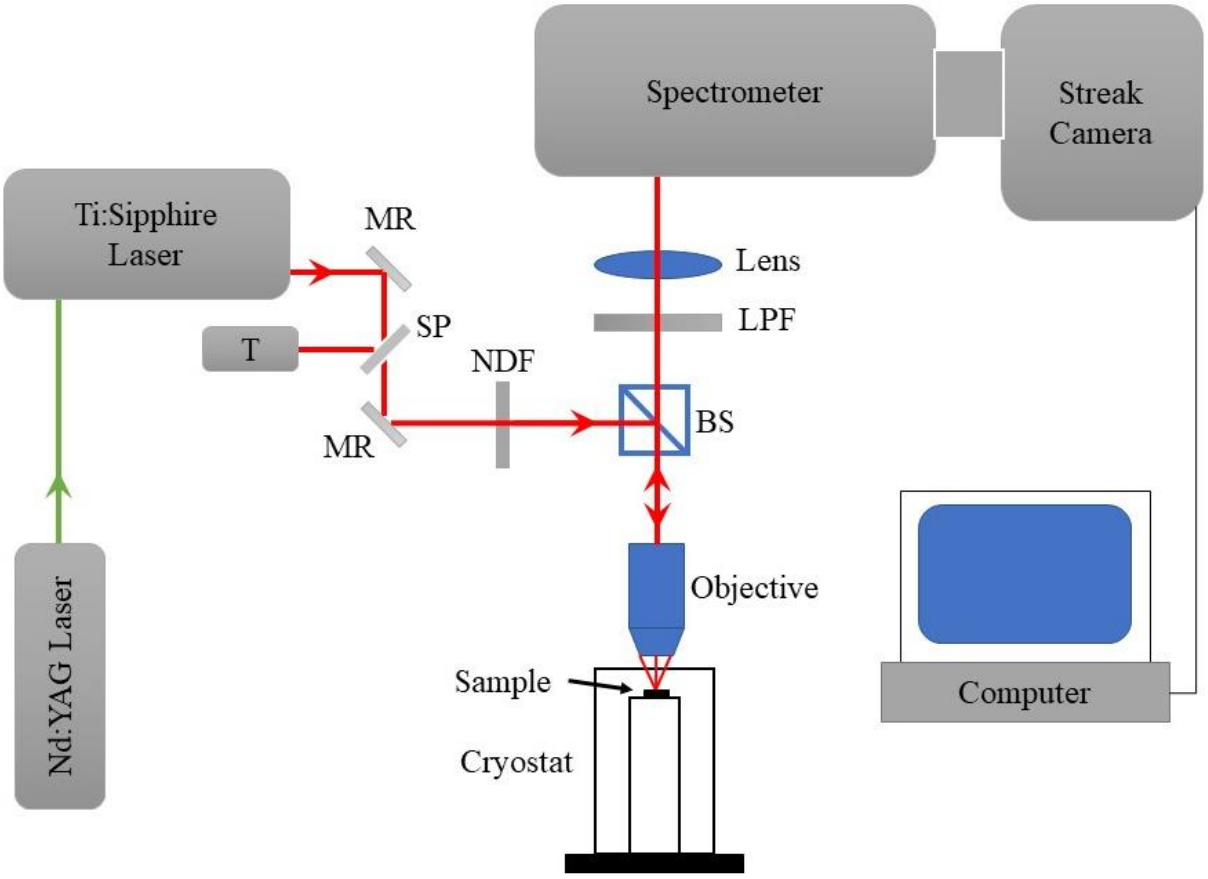

Figure 3.6. Schematic diagram of the experimental setup used to perform TRPL measurements on GaAs-based structures.

PLS2 for convenience. The sketch of the key elements of the PLS2 is shown in Fig. 3.7. The required excitation energy must be higher than 3.5 eV (energy bandgap of GaN at 10 K). Therefore, the set of mirrors, lenses, and filters are designed for the ultraviolet (UV) spectrum range. The higher excitation energy was reached by frequency doubling unit (FDU) which generated photons with energy 4.66 eV (266 nm) from the main line of Verdy-V10. Unlike the PLS1, the PLS2 exploited the property of PL to emit light in all directions with an angle excitation design which has its own advantages and disadvantages. The major advantage is the unnecessity of a beam splitter and a long pass filter for the laser line.

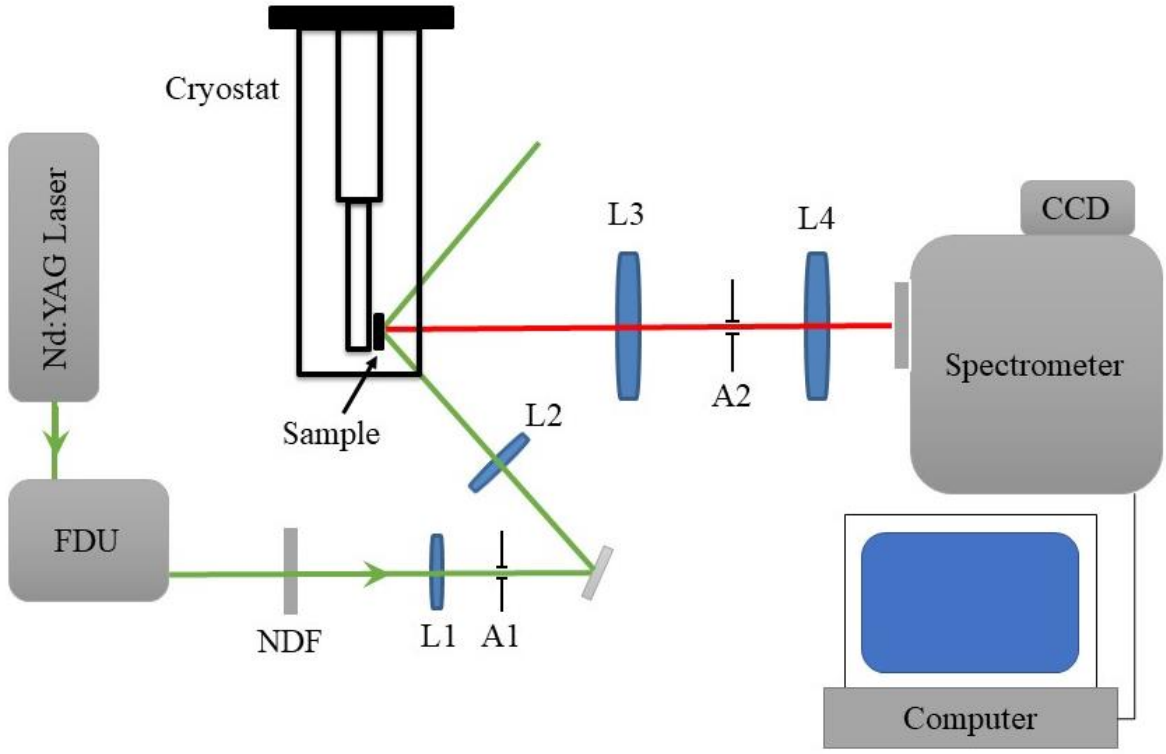

Figure 3.7. Schematic diagram of the experimental setup PLS2 used to perform PL measurements on GaN-based structures.

Chapter 4: Optical Properties of Ultrathin In(Ga)As/GaAs QW. The Effect of QW Thickness

Recent advances in MBE growth methods and precision controls allow growers to control the individual layer thickness down to its physical limit of a single atomic layer. However, the lack of understanding of the structural and physical characteristics of such structures prevents engineers from designing and producing effective devices based on the ultrathin layers embedded in a structure. As a result, such devices cannot compete with the devices based on well-established growth methods such as SK QDs and relatively thick QWs.

The aim of the research described in this chapter was to analyze and explain the optical data that were obtained from sub-monolayer InAs/GaAs QWs as well as InGaAs QWs with fixed total amount of indium. The provided discussion is mainly based on the work by Kumar et al.[31] The samples and analysis were structured in a way to solve the discrepancy in literature about the nature of formation of ultrathin InAs/GaAs QW during and after the capping process. The two contradicting models are islands or sub-monolayer QDs and gradient InGaAs layers formed by a segregation mechanism. The data were analyzed based on both perspectives. The major questions that were attempted to be answered are:

- How does the segregation affect the optical characteristics of a structure?
- Is there any non-destructive method of analysis which is suitable to determine indium redistribution within the QW?
- Does XRD analysis provide sufficient results to determine the physical structure of ultrathin In(Ga)As/GaAs QW?

4.1 Effect of InAs/GaAs QW thickness

In the first part of the study, the thickness of InAs/GaAs QW was varied from 0.5 ML to

1.4 ML. A total of five structures were analyzed with QW thickness of N = 0.5, 0.75, 1.0, 1.2, and 1.4 ML. For simplicity, the QW thickness was introduced in a sample reference. For instance, S0.5ML corresponds to InAs QW thickness of 0.5 ML. The upper limit of 1.4 ML helped to ensure the total grown thickness was below the critical thickness which, in case of pure InAs, roughly equals to 1.5 ML. Growing a thicker layer would result in InAs QDs formation via the Stansky – Krastanov (SK) method. Therefore, the analysis was focused strictly on a 2D grown mode of the InAs QW embedded in the GaAs matrix.

Based on the island formation model, one can expect 50% of the surface coverage in case of S0.5 ML. Indeed, the literature suggests the formation of islands of 5 – 6 nm in diameter with height of 1 ML. However, the analysis was performed on an uncapped surface and all further discussion is based on an assumption that each individual island preserved its shape after the GaAs capping process. The amount of a sub-monolayer coverage affects the size of islands as well as reduces the average distance between them. Since the average distance between the islands is much smaller than an exciton Bohr radius (for InAs $a_B \approx 15$ nm), the wave functions of each island overlap. From a quantum mechanics perspective, the closely arranged InAs islands are indistinguishable from the InGaAs alloy with the random atom arrangement. Considering the structure with 1 ML InAs, the complete layer coverage was taking place. Therefore, the classic InAs/GaAs with thickness of 0.3 nm (corresponds to the atomic layer thickness for InAs) was considered as a model. The analysis for samples S1.2ML and S1.4ML was performed in the following way:

- The total QW thickness was set to 2 MLs.
- The first monolayer corresponded to pure InAs.
- The indium content in the second monolayer was set to 20% and 40% for S1.2ML and

S1.4ML, respectively.

Using the described structure, the energy band diagram of, potentially, a 3D structure (due to the system of islands in the second layer) can be analyzed as its 1D analogy. The second layer due to the wave functions coupling can be modeled as InGaAs alloy with corresponding indium content in analogy to sub-monolayer structures. The resulting step-like energy band diagram is shown in Fig. 4.1. In addition, the cross-section of the possible structure is presented on the right. The blue color corresponds to the GaAs matrix, and the yellow is the InAs layer with the islands on top of it.

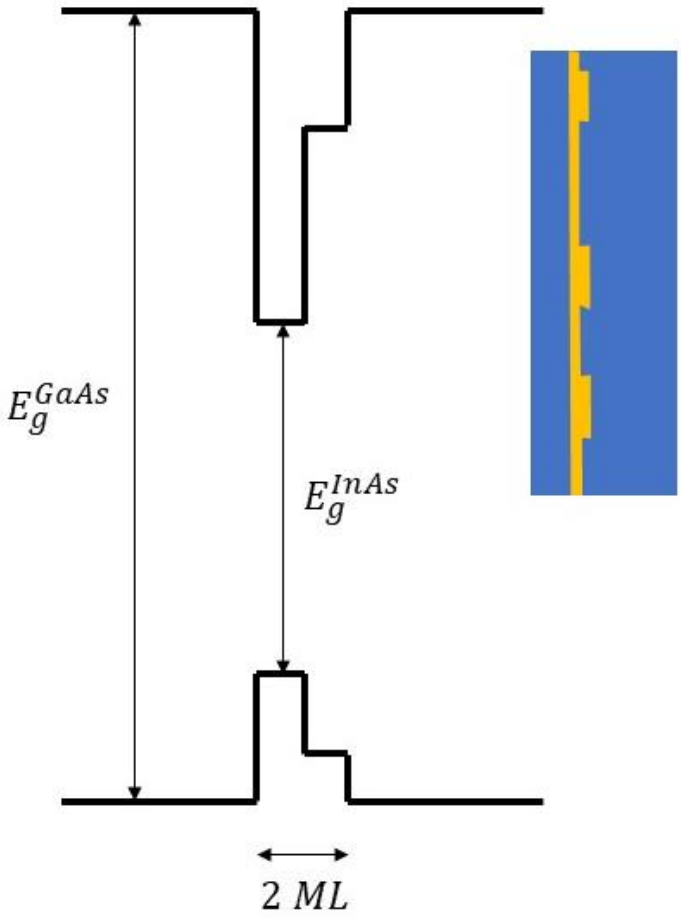

Figure 4.1. Schematic energy band diagram of InAs/GaAs QW structure for the QW thicknesses exceeding 1 ML.

4.2 XRD analysis of samples with varied InAs/GaAs QW thickness

The structural properties of the given samples were analyzed by means of XRD. The expected accuracy can reach 0.1 ML, which makes XRD an exceptional tool for the non-destructive structural analysis of ultrathin QWs. The experimental XRD data for each sample as well as simulation are shown in Fig. 4.2. Since the contribution of an ultrathin layer to the overall x-ray diffraction pattern is minimal, a different approach of analysis was established. Specifically, the diffraction pattern was formed by GaAs buffer layer (underneath of InAs QW) and GaAs cap layer. Therefore, the effective thickness of the InAs layer was the separation between two GaAs blocks.

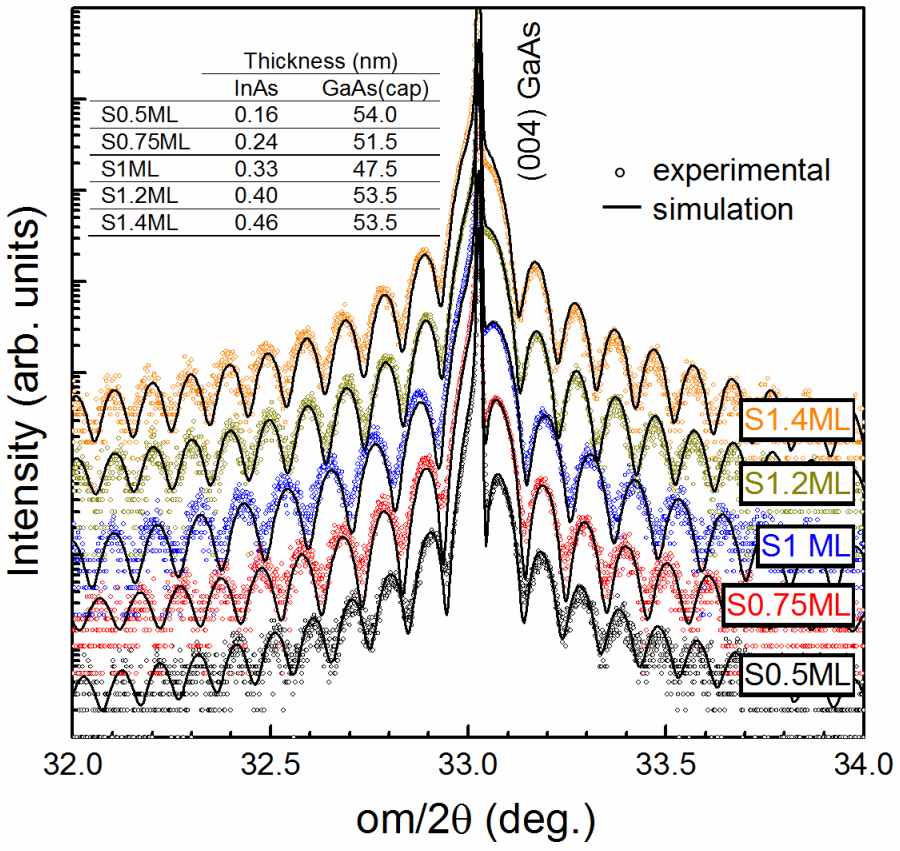

Figure 4.2. Experimental XRD data (empty circles) and corresponding simulations (black solid lines) taken along [004] crystallographic direction.

The large number of pandelösung fringes in the XRD spectra points to the high crystal quality for all given samples. The "best fit" for the experimental x-ray diffraction data reveals the thicknesses of the GaAs cap layer and InAs QW. The thickness of InAs layer was calculated assuming an abrupt rectangular shape of the indium content profile. Additionally, it is worth mentioning that simulation neglected indium and gallium intermixing within the QW and GaAs cap layer regions. Simulating the same experimental data assumed the In/Ga intermixing effect would result in a thicker InGaAs QW region. Table 4.1 summarizes the layer thicknesses considering a fully strained system. Despite the 5% thickness variation for the GaAs cap layer (the designed GaAs cap thickness is 50 nm), the InAs QW thickness agreed exceptionally well with the intended QW thickness calibrated based on the RHEED data.

Table 4.1. Key layer thicknesses retrieved from the XRD simulation.

	Thickness (nm)	
	InAs	GaAs (cap)
S0.5ML	0.16	54.0
S0.75ML	0.24	51.5
S1ML	0.33	47.5
S1.2ML	0.40	53.5
S1.4ML	0.46	53.5

4.3 Photoluminescence analysis of samples with varied InAs/GaAs QW thickness

Photoluminescence analysis was performed on all five samples as the convenient non-

destructive method of probing optical properties of the system. The general normalized PL results measured under medium excitation intensity are presented in Fig. 4.3. All experimental data shown as empty circles were fitted using Gaussian curve shape calculated by equation:

$$I_{PL} = \exp(-\frac{(PE - PE_{peak})^2}{2\omega^2}), \qquad \text{(Equation 4.2)}$$

where I_{PL} is the normalized PL intensity which corresponds to photon energy PE, PE_{peak} is the photon energy in the peak of PL signal, and ω is the standard deviation, which directly

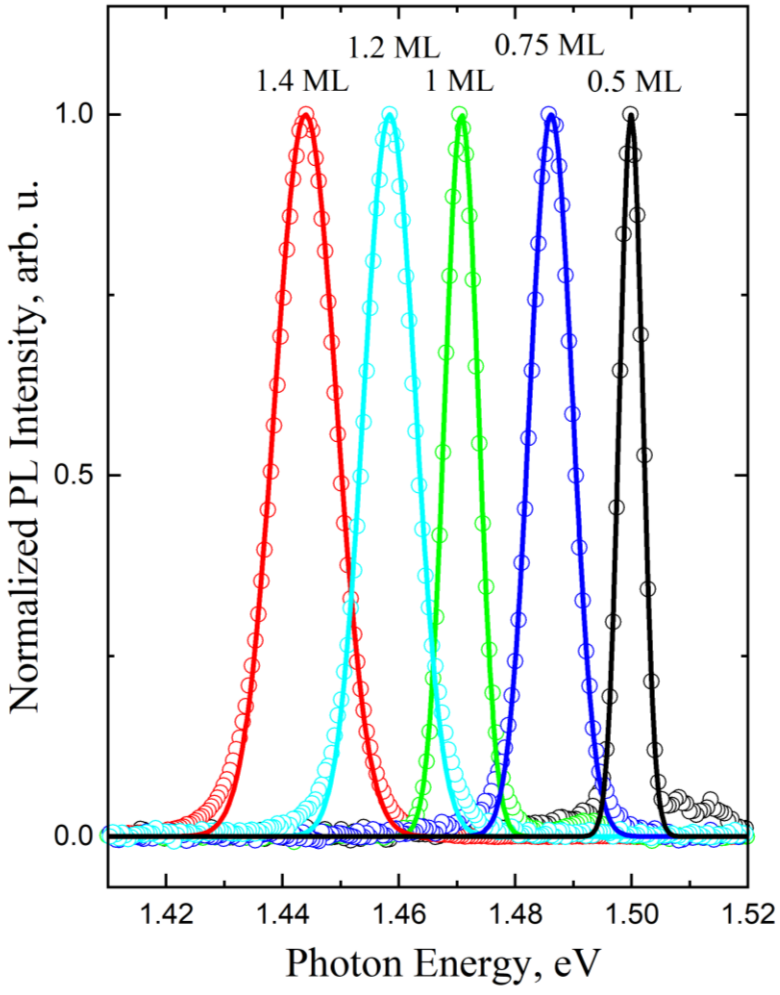

Figure 4.3. Normalized low temperature experimental (10 K) PL results (empty circles) and Gaussian fitting (solid lines) measured for different thicknesses of InAs/GaAs QWs.

corresponds to the full width at half maximum (FWHM) used later in the chapter by the relation:

$$\mathrm{FWHM} = 2\sqrt{\ln 4}\,\omega, \qquad \text{(Equation 4.3)}$$

As can be deduced from Fig. 4.3, the PL from the sample S1.0ML follows nearly perfect Gaussian shape. The PL from the rest of the four samples was characterized by the prominent low-energy tail. A heavy-hole (hh) InAs QW transition generally forms an asymmetric PL line. However, in case of low thermal energy, the PL line becomes thinner and widening of the Gaussian shape is the result of overall crystal quality (density of the defects), QW/barrier interfaces consistency, and chemical homogeneity within active layers.

Initially, when the samples were designed, it was assumed that sample S0.5ML, S0.75ML, and S1.0ML generate PL peak with the same spectral position. According to the island formation model, the three given structures form 1 ML high InAs islands. The spacing between them is filled with the GaAs. Since the lateral size of each island is much larger than its height, the overall quantum confinement of any individual island is mostly affected by its height. The S1.0ML sample is the extreme case of 1ML islands formation. In this case complete layer of InAs was formed which can be treated as one big island. The PL peak intensity would directly correspond to the island coverage reaching a maximum for sample S1.0ML. The same discussion can be applied for the S1.2ML and S1.4ML structures. However, instead of one peak corresponding to the 1ML InAs emission, two peaks would be formed as an analogy to the well-known PL emission from InAs QDs where one peak corresponds to the wetting layer and the second to the QDs. However, for InAs coverage higher than one monolayer but less than the critical thickness, the second peak would correspond to the 2 ML InAs/GaAs QW. This emission model is shown in Fig. 4.4. The PL peaks correspond to the PL emission from two spatially separated regions. The intensity ratio between PL1.0ML and PL2.0ML is directly

proportional to the total indium deposition since it affects the density and size of the islands in the second layer.

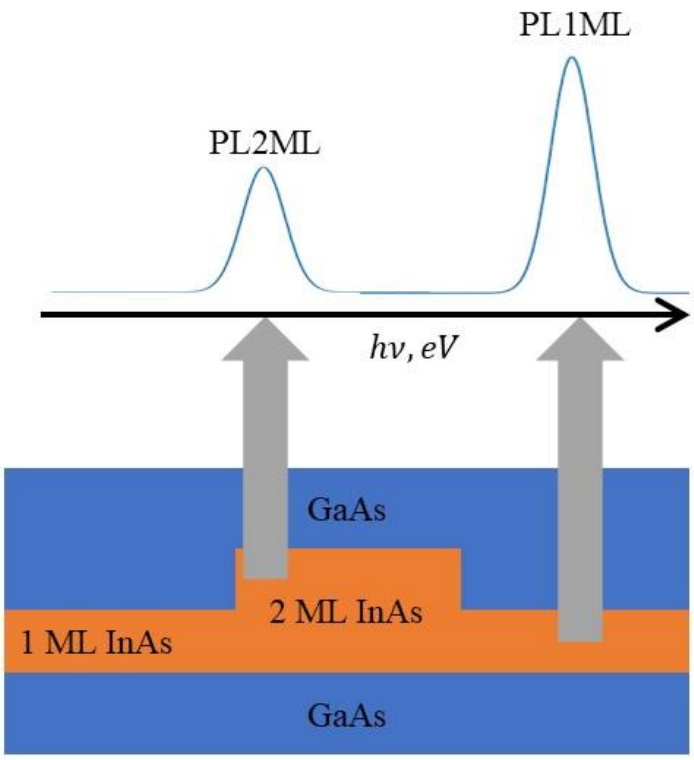

Figure 4.4. Schematic representation PL emission from the InAs/GaAs QW structure with the QW thickness more than 1 ML.

The discussion above is a plausible model of PL emission, and the same type of analysis was applied for explaining PL of In(Ga)As QDs. However, observing the continuous PL peak shift, one can make a conclusion that the mentioned model is not suitable for the InAs deposition of less than critical thickness. The PL peak energy for given samples as a function of InAs deposition thickness is shown in Fig. 4.5. As can be observed from the graph, the PL emission energy decreases following linear tendency with increasing InAs/GaAs QW thickness. Similar observations were previously reported in the literature. The explanations provided by previous studies are not consistent since the observed behavior can be explained by two mutually

exclusive models. The first model is based on the mentioned in-plane 1 ML InAs islands formation with the lateral diameter from 2 to 4 nm.

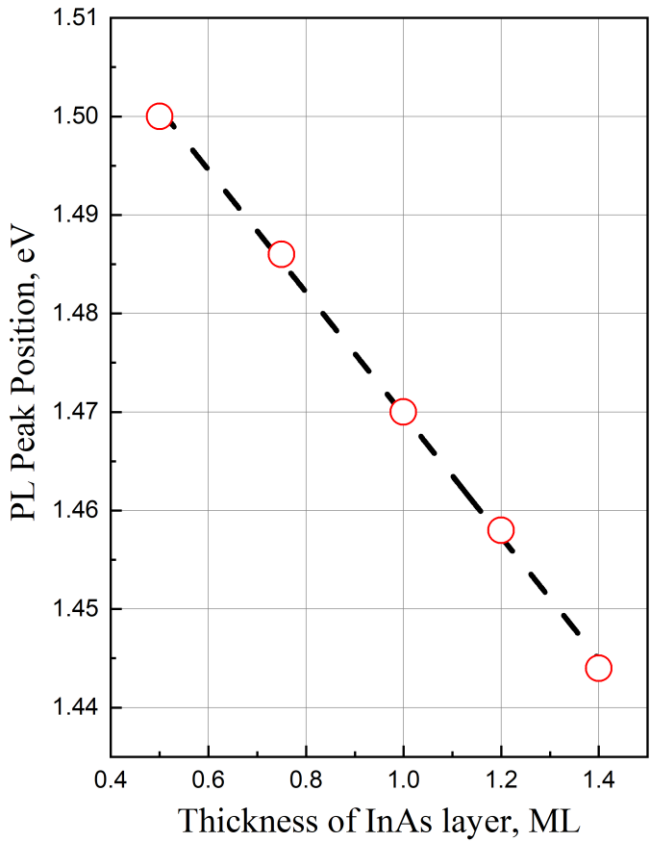

Figure 4.5. PL peak emission energy as a function of InAs/GaAs QW effective thickness (empty circles) and linear fitting (black dashed line).

This model, however, assumes the strong quantum coupling between islands since the exciton Bohr radius is larger than the sizes and distances between islands. Unlike the individual islands model, the coupling between islands provides explanation of the linear trend of the PL emission energy shift. While increasing the InAs deposition from 0.5 to 1 ML, the effective in-plane amount of GaAs within the QW region decreases, which leads to the gradual transition energy reduction. This behavior can be demonstrated as an analogy to the double quantum well system shown in Fig. 4.6, where the 3 nm wide InAs wells represent islands and the separation

between them is determined by the barrier thickness between the QWs. To simplify the analysis, the many island scenario was reduced to the two islands quantum interaction. Introducing more islands will make the emission energy shift more prominent (keeping the general trend the same). Admittedly, the analogy between the double QWs and in-plane island is oversimplified due to the following reasons:

- Each individual island has its own shape and size, which affects the corresponding QW width.
- Quantum interaction between more than two islands was neglected.
- The 1D double QW simulation does not include 2D quantum confinement effect within an island as well as in-plane 2D coupling effect.

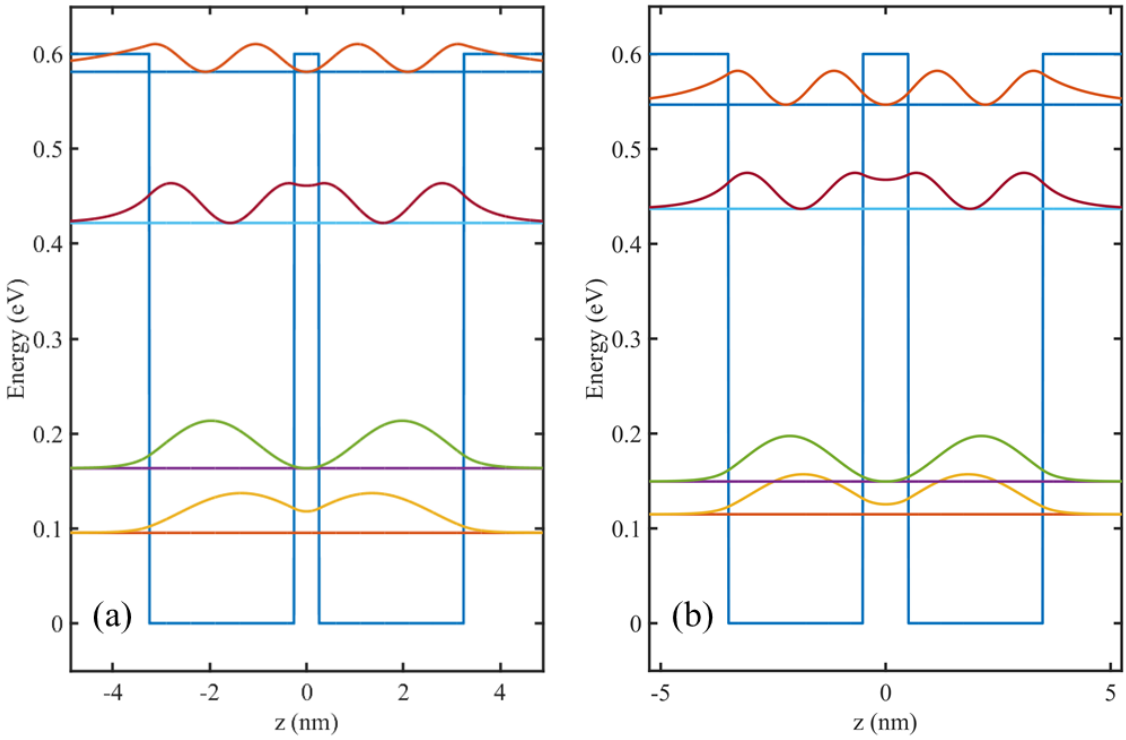

Figure 4.6. The double 3 nm InAs/GaAs QW system with the barrier thickness changed from 0.5 nm (a) to 1 nm (b).

The two double QW systems shown in Fig. 4.6 differ by the barrier thickness, which was obtained from the total in-plane coverage. Sample S0.5ML with 50% of coverage corresponds to the 1 nm barrier thickness between 3 nm QWs, and sample S0.75ML corresponds to the 0.5 nm barrier. The conduction band ground state energy shift extracted from the figure roughly equals to 10 meV. With the contribution of the valence band energy shift (not shown in the figure), the total shift is equal to 13 meV. This value is in good agreement with the actual emission energy shift of 14 meV for samples S0.5ML and S0.75ML. Despite the obvious flaws of the double QW model, the continuous PL emission shift can be explained by the coupling effect. However, experimental data alone are not sufficient to make a conclusion whether or not the coupling is related to the chemical intermixing.

Another important parameter that can be extracted from PL data in Fig. 4.3 is the FWHM (also referred as PL linewidth) calculated using the fitted curves and Equation 4.3. The resulting PL linewidth variation as a function of InAs deposition is shown in Fig. 4.7. Comparing the observed data with the linewidth results extracted from the literature (high quality InGaAs/GaAs QWs), the linewidth variation in the range from 4 to 13 meV indicates high structural quality of the InAs/GaAs QW. Also, such sharp PL lines are easily distinguishable from one another given the tight spectral locations of the PL peaks for all five structures.

The gradual linewidth rise with the InAs thickness increase is observed for samples with an incomplete InAs layer. In contrast, the FWHM for sample S1ML shows different behavior as it is considerably smaller than for the neighboring InAs depositions. There are a few possible explanations of such observation including different InAs layer formation models discussed above. One possible cause of line broadening can be related to the interface roughness, which naturally increases with the active layer coverage. The second possibility is due to the

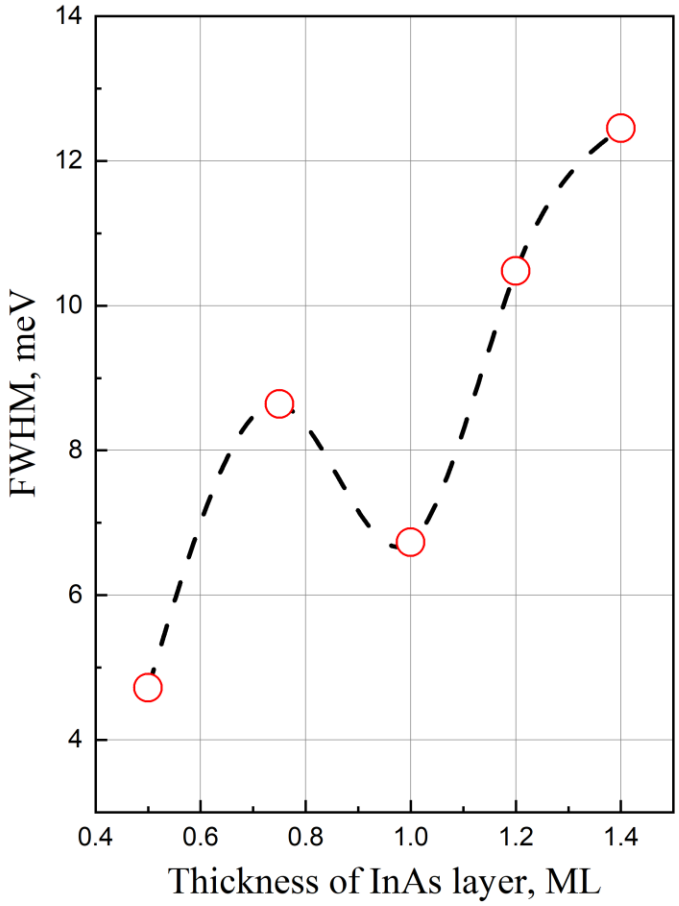

Figure 4.7. PL emission linewidth (FWHM) as a function of InAs/GaAs QW effective thickness (empty circles) and eye-guiding spline (black dashed line).

broadening of the island distribution curves in terms of shape and size. Larger InAs layer depositions lead to the nucleation of new islands while the formed islands might overlap forming more complex shapes. This causes the broadening of the energy states shared by the islands. Moreover, this explanation is well-aligned with the special case of S1ML where all islands are merged into one homogeneous layer. The PL broadening of such complete layer can only be caused by the roughness of interfaces. The third possibility is related to the In/Ga intermixing (indium segregation) during the GaAs capping process. Relaying on the idea of indium segregating in all directions with the same rate, the final InGaAs layer will have strongly

inhomogeneous content. As a result, the more indium introduced to the QW, the more indium content inhomogeneity it will cause.

All previous data were based on the PL measurements with fixed excitation intensity. The following analysis will focus on the intensity dependent PL measured under low temperature at 10 K. This type of analysis is capable of providing valuable information about the state filling effect in the system. For the measurement, the excitation intensity was varied by six orders of magnitude based on the well-calibrated neutral density filter set. The resulting spectra for each sample are summarized in Fig. 4.8. Under higher excitation intensities, the GaAs related peaks can be observed. The bulk GaAs free-exciton transition at 1.518 eV along with its impurity related emission at 1.495 eV were underlined with the vertical dashed lines to distinguish them from the InAs QW related emission.

For all samples, strong heavy-hole (hh) emission was observed. In addition to the hh emission, the spectra for sample S0.5ML also contain lite-hole (lh) related emission around 1.51 eV. This value was extracted from the deconvoluted spectrum of sample S0.5ML recorded under medium excitation intensity shown in Fig. 4.9. The appearance of the lh emission for the sub-monolayer InAs coverage was confirmed by the literature. This observation is explained by the reduced density of states which leads to the state filling effect for hh transition making lh and bulk GaAs related transitions more prominent. Another possibility is the increased probability of the carrier escape to the GaAs barrier due to the lower activation energy (comparing with the higher InAs coverage of one and above ML). It also should be noted that relative intensity of the bulk GaAs is often hidden in the device noise (as can be observed in Fig. 4.8 at 1.52 eV) as compared to the main InAs peak intensity. However, for the highest excitation intensities, the distinct GaAs related peak can be clearly observed.

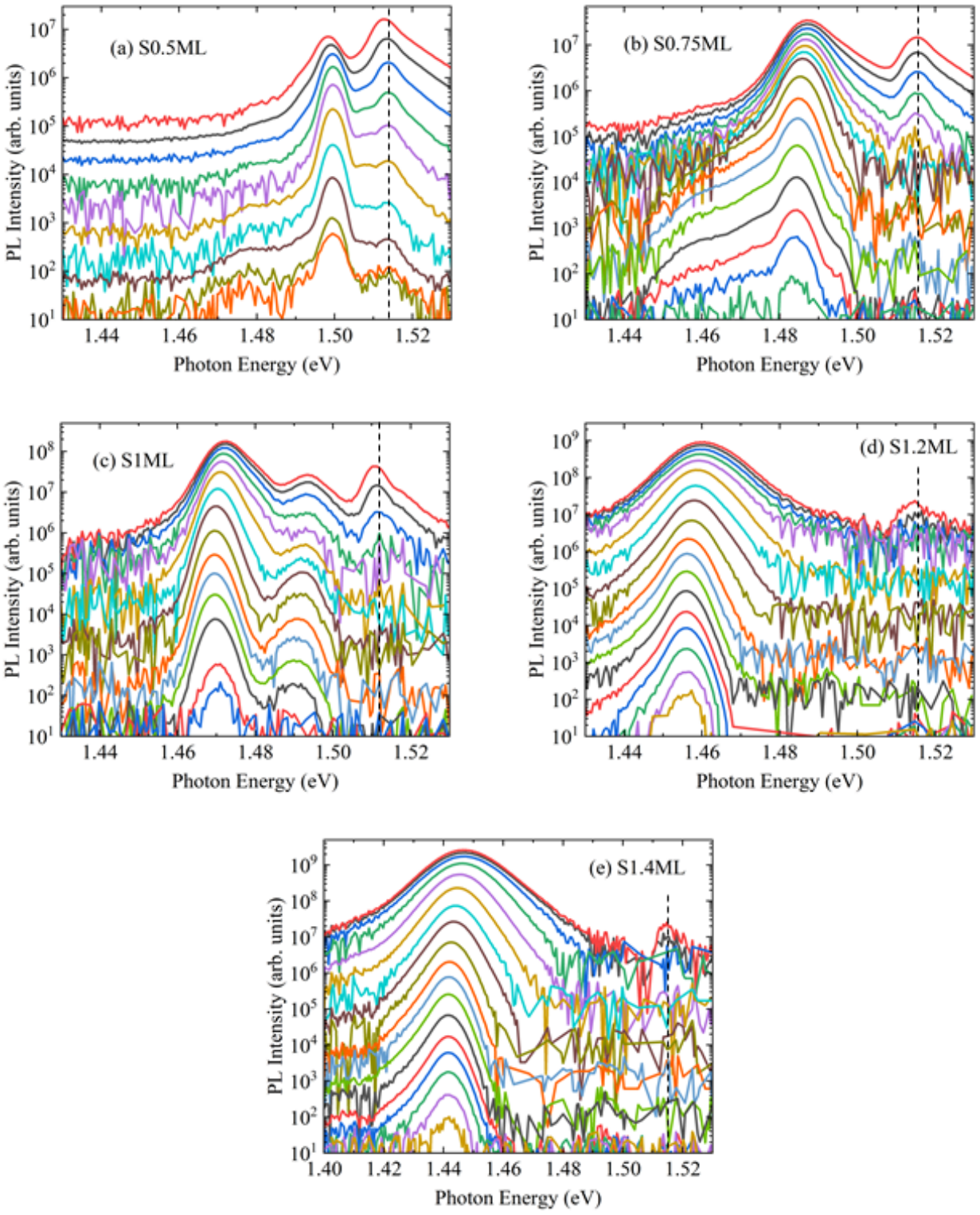

Figure 4.8. Power dependent PL spectra of InAs/GaAs QW measured and plotted in log-scale format for all samples. The dashed black vertical line shows the expected spectral position of GaAs bulk emission.

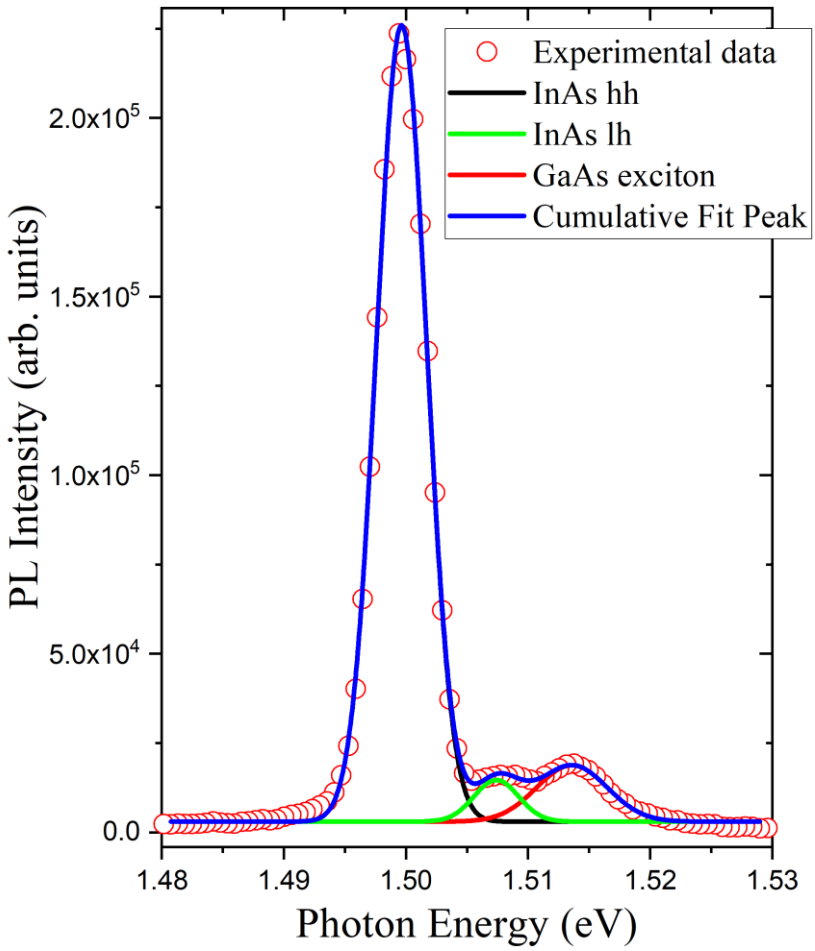

Figure 4.9. Deconvolution (shown as solid lines) performed on PL data for sample S0.5ML.

From the intensity dependent measurements, there are a few noticeable characteristics that are common for all given structures that can be observed:

- In general, the PL peak position experiences blue-shift under the increasing excitation intensity.
- The FWHM increases with excitation power.
- Naturally, the integrated InAs emission peak follows the power law relation with the excitation intensity.
- The asymmetric behavior of the InAs peak vanishes with increasing excitation power.

In order to explore these observations in more detail, the PL peak position, linewidth, and integrated intensity as a function of incident excitation intensity were plotted for each sample. Before discussing each feature of the given samples, the general power dependence trend has to be explained. Considering the simplified energy band diagram in a k-space (momentum) shown in Fig. 4.10, electron-hole pairs generated by incident photons will first occupy the lowest energy state, which corresponds to the lowest kinetic energy of the carriers ($k = 0$). While increasing the excitation intensity (effectively increasing the supply of electron-hole pairs per second), the minimum of the conduction band and the maximum of the valence band become populated with the carriers. Therefore, due to the relatively short lifetime of the electrons in the conduction band, electron-hole pairs start to occupy higher energy states ($k \neq 0$). In terms of the effect on PL spectra, it means increasing linewidth with excitation power. This effect is also known as

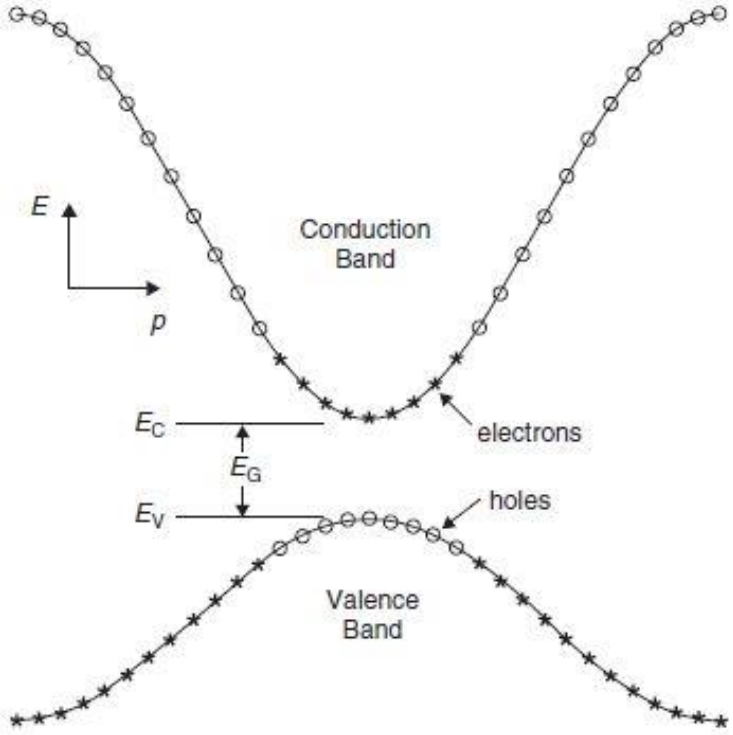

Figure 4.10. Energy band gap illustration shown in k-space (momentum).

the Burstein–Moss shift, which corresponds to the absorption edge shift to the higher energies due to the state filling effect.

Similar reasoning can be applied to the PL peak position dependence on the excitation power. While generating more electron-hole pairs per unit of time, the quasi Fermi levels of the conduction and valence band become more separated. This effectively leads to the carrier population redistribution within the conduction and valence band. Therefore, population of the carriers will only depend on the probability of occupying the state (Fermi – Dirac distribution) modified by the number of the available energy states (density of states). The resulting population density curve will have a maximum which does not coincide with the conduction or valence band edges. As a result, the higher separation of the quasi Fermi levels leads to the higher electron-hole recombination energies. Therefore, it is expected that the PL peak position would experience the blue-shift with increasing the excitation power.

The actual PL peak position and linewidth are shown in Fig. 4.11 and Fig. 4.12, respectively. The PL linewidth (FWHM) for each given sample exactly follows the trend described above. As can be deduced from Fig. 4.12, the FWHM roughly doubles in terms of energy while changing the excitation intensity from lowest to highest possible value for each individual sample. The PL peak position power dependence, however, reveals two anomalies which cannot be addressed using the provided explanation. The first anomaly is the slight PL peak red-shift at low excitation powers followed by blue-shift at higher intensities for sample S1ML. The second anomaly is the continuous red-shift of the peak with increasing the excitation power.

The unusual PL peak behavior of sample S1ML can be explained in terms of interplay between free electron-hole and exciton related recombination as follows. At low temperature

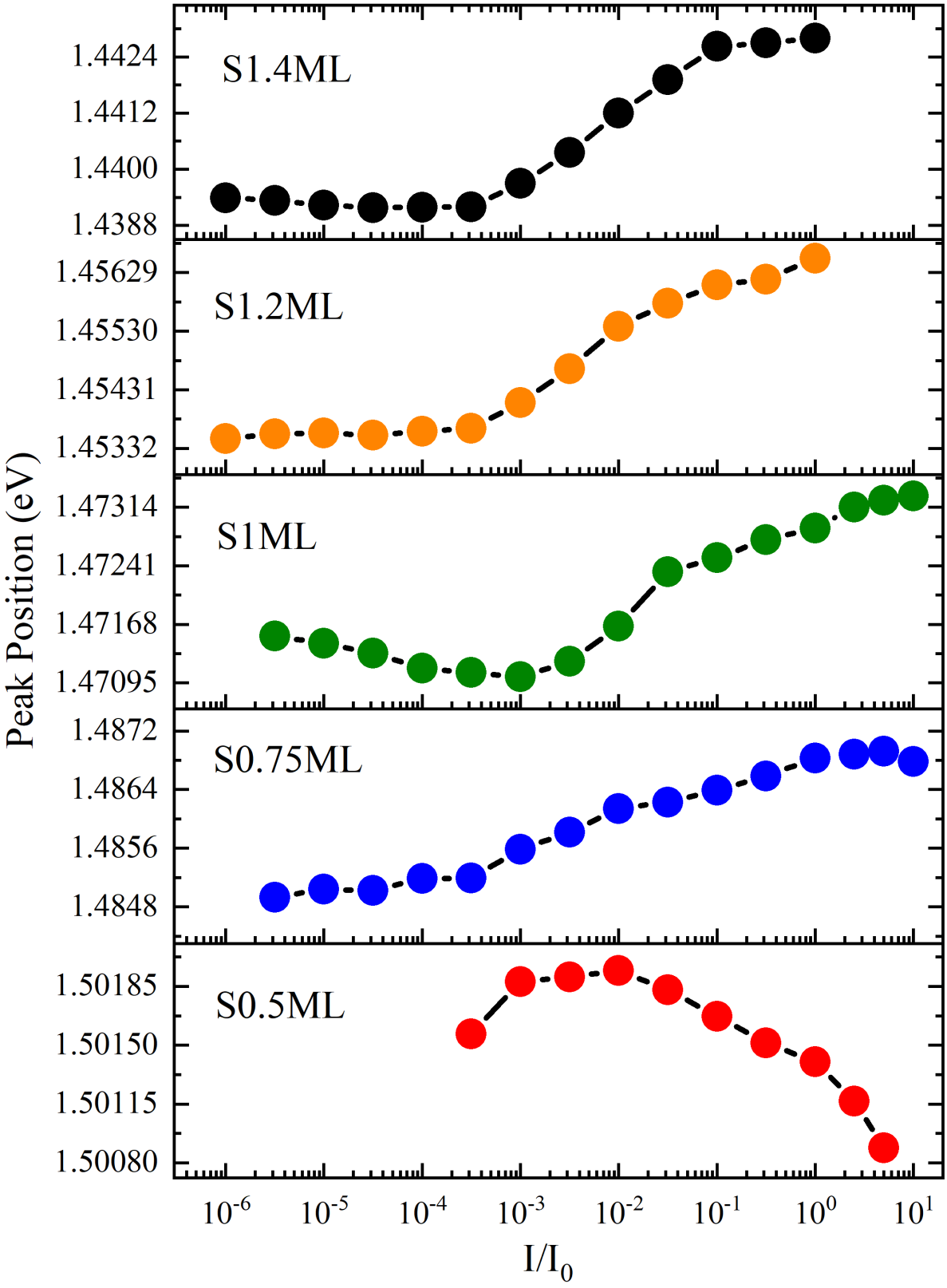

Figure 4.11. Power dependence of the PL peak position for samples with different InAs/GaAs QW thicknesses. I_0 = 1000 W/cm^2, T = 10 K.

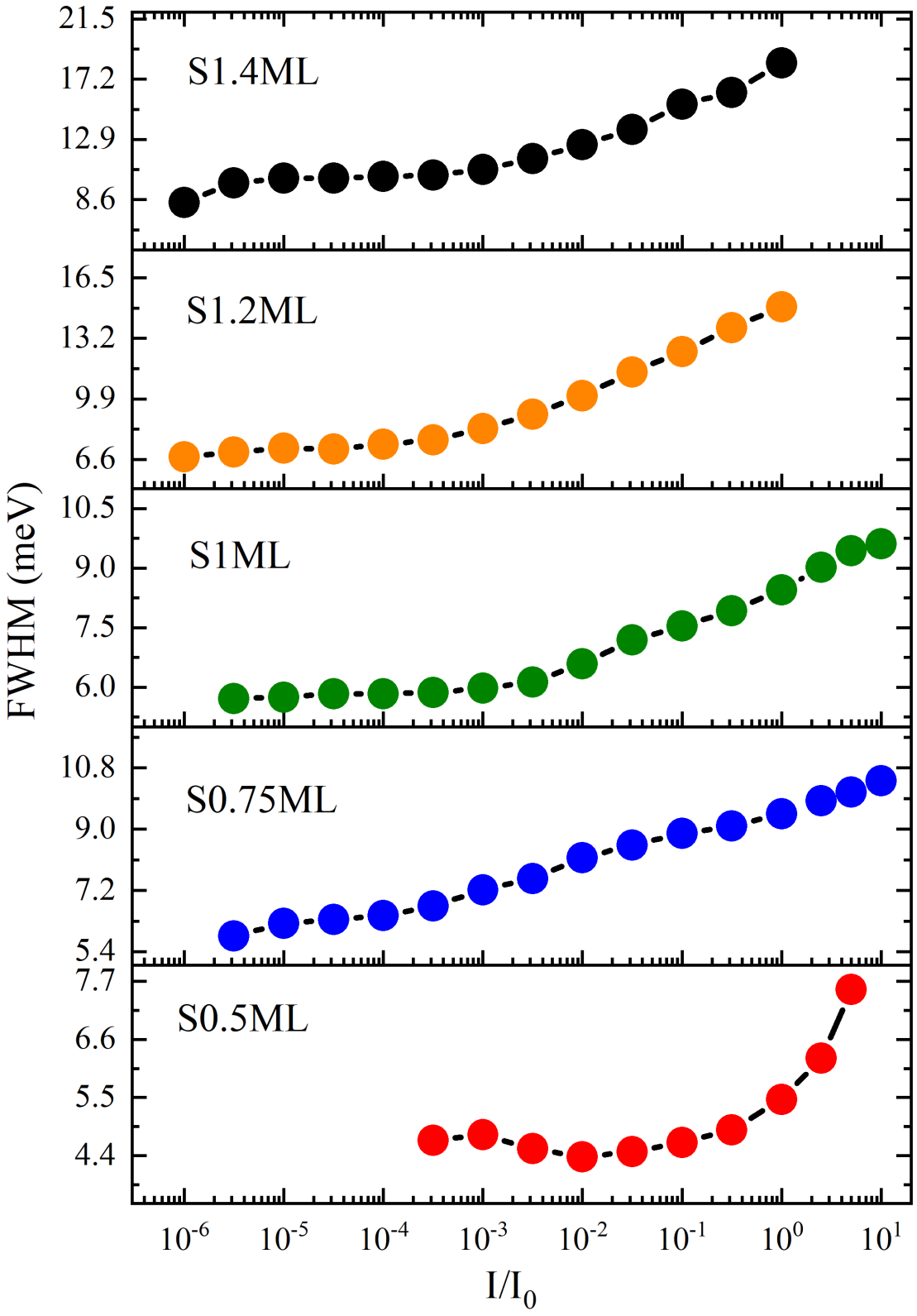

Figure 4.12. Power dependence of the PL linewidth (FWHM) for samples with different InAs/GaAs QW thicknesses. I_0 = 1000 W/cm^2, T = 10 K.

and excitation power, the probability of electron and hole interaction is small due to the low density and mobility of either. Given this notion, the recombination due to the free electron-hole pairs will be more prominent than exciton related transition. While increasing the excitation power, the influence of exciton related transition becomes stronger as was previously reported for a non-resonant excitation. The photon generated from the exciton recombination has slightly smaller energy than the one generated from a free (not bounded) electron-hole pair. The reason for this is Coulomb's interaction between charged carriers, which effectively reduces the exciton recombination energy by 5 – 10 meV. Therefore, the PL peak behavior for sample S1ML at low excitation powers can correspond to the increased probability of the excitonic transitions. The following blue-shift of the PL peak is related to the state filling effect described earlier. This effect becomes dominant at higher excitation intensities. This behavior, however, was not observed for samples S0.75ML, S1.2ML, and S1.4ML. One possible reason is that these structured had an increased number of localized energy states due to the higher roughness of the interfaces as followed from analyzing the PL peak linewidth and its asymmetry behavior. As a result, at low range excitation intensities, the recombination process occurred through localize channels (trapped carriers), increasing the probability of exciton formation.

The PL peak behavior of sample S0.5ML does not follow the same logic. In this case, the observed red-shift can be attributed to the local hitting effect and carriers escaping to the barrier. The combination of these processes effectively decreases the recombination energy with increasing excitation power. The carrier escape to the barrier is more prominent for sample S0.5ML due to the low activation energy. The generated carrier has more non-radiative recombination channels in GaAs, which potentially increases the local lattice temperature resulting in narrowing of the effective band gap.

The overall PL emission efficiency was analyzed in terms of integrated area under the corresponding curves recorded at the same excitation intensity. The resulting integrated PL intensity as a function of InAs/GaAs QW thickness is shown in Fig. 4.13. The integrated PL intensity follows an increasing trend (shown as dashed black line in Fig. 4.13) with the nominal InAs QW thickness. The PL efficiency starts to be saturated after the thickness of InAs QW exceeds 1 ML. Moreover, samples S1.2ML and S1.4 ML show almost equal PL efficiency. The three orders of magnitude efficiency increase was observed while the nominal thickness of the InAs QW was increased from 0.5 to 0.75 ML. All in all, the general behavior of the integrated PL intensity is quite predictable since the activation energy increases with the InAs QW increase.

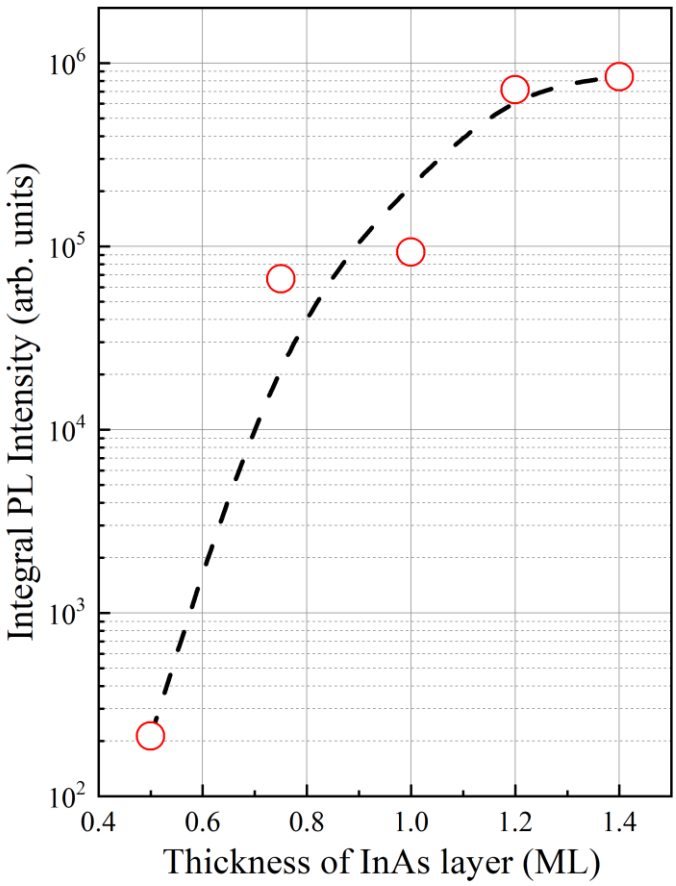

Figure 4.13. Integrated PL emission as a function of InAs/GaAs QW effective thickness (empty red circles) and eye-guiding spline (black dashed line).

As a result, the integrated PL has nearly exponential behavior following the linear trend of activation energy increase (deduced from Fig. 4.5 as the change in activation energy is inversely proportional to the change in transition energy).

The power dependence of the integrated PL peak area is shown in Fig. 4.14. Generally, the integrated PL increases with excitation intensity by the following power law:

$$I_{PL} = \eta I_{exc}^{\alpha}, \qquad \text{(Equation 4.4)}$$

where I_{PL} is the area under the PL peak corresponding to the specific excitation intensity I_{exc}, η is the constant factor, and α is the exponent factor, which holds valuable information about the

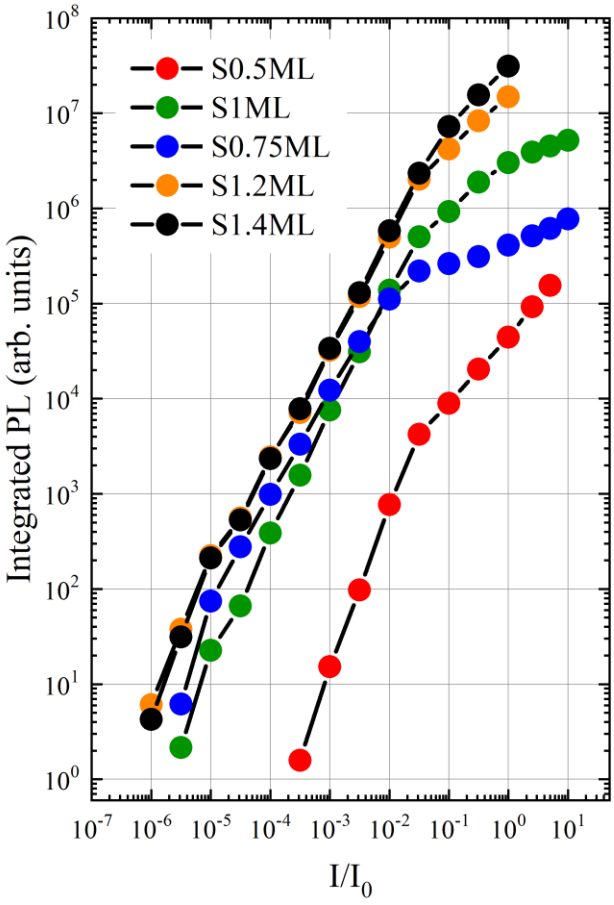

Figure 4.14. Power dependence of the integrated PL peak area for samples with different InAs/GaAs QW thicknesses. I_0 = 1000 W/cm^2, T = 10 K.

type of radiative recombination mechanism. The purely excitonic recombination corresponds to linear integrated PL power dependence ($\alpha = 1$). In contrast, the free electron-hole pair recombination process leads to the quadratic dependence ($\alpha = 2$). For the real integrated PL measurements, the exponent factor belongs to the range from 1 to 2 indicating mixed recombination mechanism. Considering Equation 4.4, it is useful to plot the power dependence of the integrated PL in log-log scale leading to the following relation:

$$\log I_{PL} = \log \eta + \alpha \log I_{exc}, \qquad \text{(Equation 4.5)}$$

from which the exponential factor (α) can be easily retrieved from Fig. 4.14 as the slope of the linear fitting.

After the experimental data fitting, the exponent factor was found to be close to one for low – middle range excitation intensity (10^{-3} – 10 W/cm^2), except for S0.5ML, which demonstrated quasi quadratic behavior with the exponential factor equal to 1.79. This indicates domination of free electron-hole over excitonic recombination types. Also, the small activation energy (barrier escape threshold) can effectively modify the exponential factor increasing it toward quasi quadratic power law. Particularly, the relatively large exponential factor of S0.5ML can be related to the lowest activation energy among all five structures in focus.

The integrated PL dependence at high excitation power (more than 30 W/cm^2) does not follow the power law due to the state filling effect. This can be considered by introducing excitation power dependence of quantum efficiency hidden in a constant factor η from Equations 4.4 and 4.5. However, the exact dependence of $\eta = \eta\left(I_{exc}\right)$ for $I_{exc} > 30\,\frac{W}{cm^2}$ does not contain information about the recombination type, but rather information about the excitation intensity value starting from when the conduction and valence bands become saturated with carriers.

4.4 Temperature dependent PL of samples with varied InAs/GaAs QW thickness

In order to find the accurate value of activation energy, the temperature dependent PL measurements were performed for each of the samples. The excitation intensity was kept constant to ensure each structure was measured under equivalent conditions. As an example, the raw temperature dependent PL data for sample S1ML is shown in Fig. 4.15. Temperature was varied from 10 to 300 K (room temperature). In this temperature range, PL spectra were recorded every 10 K. The data presented in Fig. 4.15 and similar spectra recorded for the rest of four samples (not shown here) were analyzed in terms of peak position and integrated PL as a

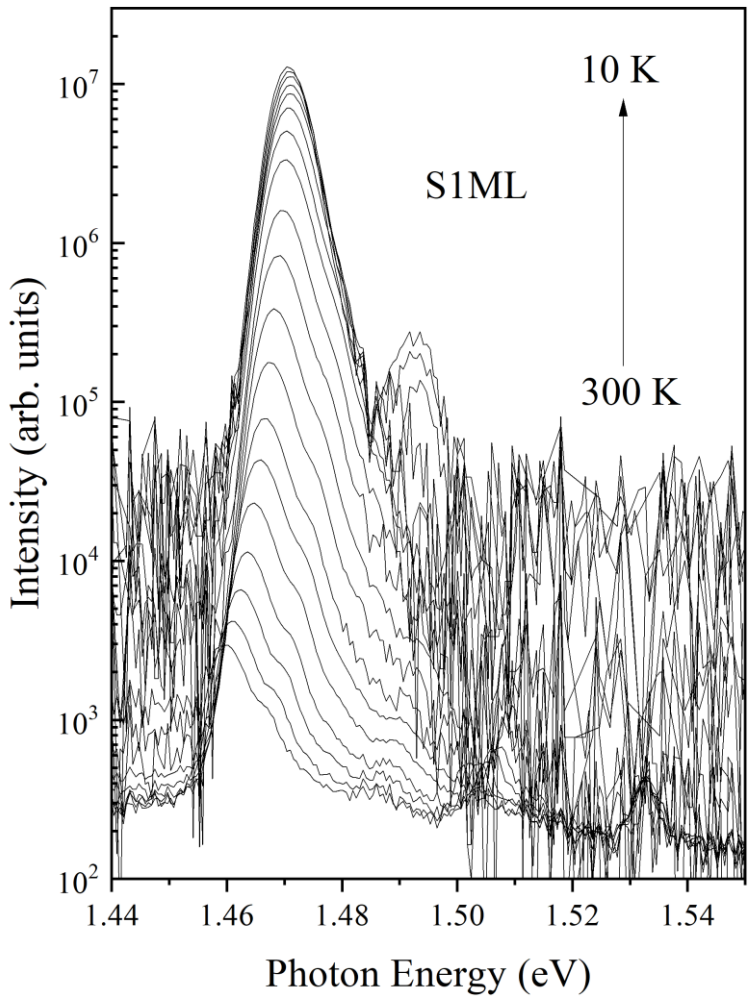

Figure 4.15. Temperature dependent PL spectra evolution for sample S1ML.

function of temperature.

The temperature dependence of the peak position can be analyzed following empirical Varshni formula:

$$E_g(T) = E_g(0) - \frac{\alpha T^2}{T + \beta}, \qquad \text{(Equation 4.6)}$$

where α and β are Varshni parameters that can be varied in order to achieve the best fit. Admittedly, other, more physically accurate, temperature dependent relations have been developed. However, the Varshni formula is more widely accepted, and the Varshni parameters are well documented for the huge variety of semiconductors giving the possibility of direct comparison with the data in this work. Moreover, the Varshni parameters for InAs are calculated with great precision and taken from comprehensive review by Vurgaftman et al.[70] The empirical Equation 4.6 is only valid for the bulk semiconductor. However, it can be applied to the effective bang gap temperature dependence of the InAs QW assuming that the ground states of the conduction and valence bands are constant and do not depend on the slight changes of the InAs and GaAs band offsets. Therefore, the effective band gap of InAs/GaAs QW will take the following form:

$$E_g^{eff} = E_g + \Delta E_{e1} + \Delta E_{hh1}, \qquad \text{(Equation 4.7)}$$

where E_g is the energy bandgap of bulk InAs, and ΔE_{e1} and ΔE_{hh1} are the first conduction and valence band energy levels, respectively. As a result, the effective bang gap should follow the same dependence as the corresponding bulk material. The difference between those two dependences should be constant as follows from Equation 4.7. Practically, it means that the calculated band gap temperature dependence can be shifted by a constant factor and directly compared to temperature dependence of the PL peak position. The PL peak position temperature

dependencies for samples S0.5ML, S1ML, and S1.4ML are shown in Fig. 4.16.

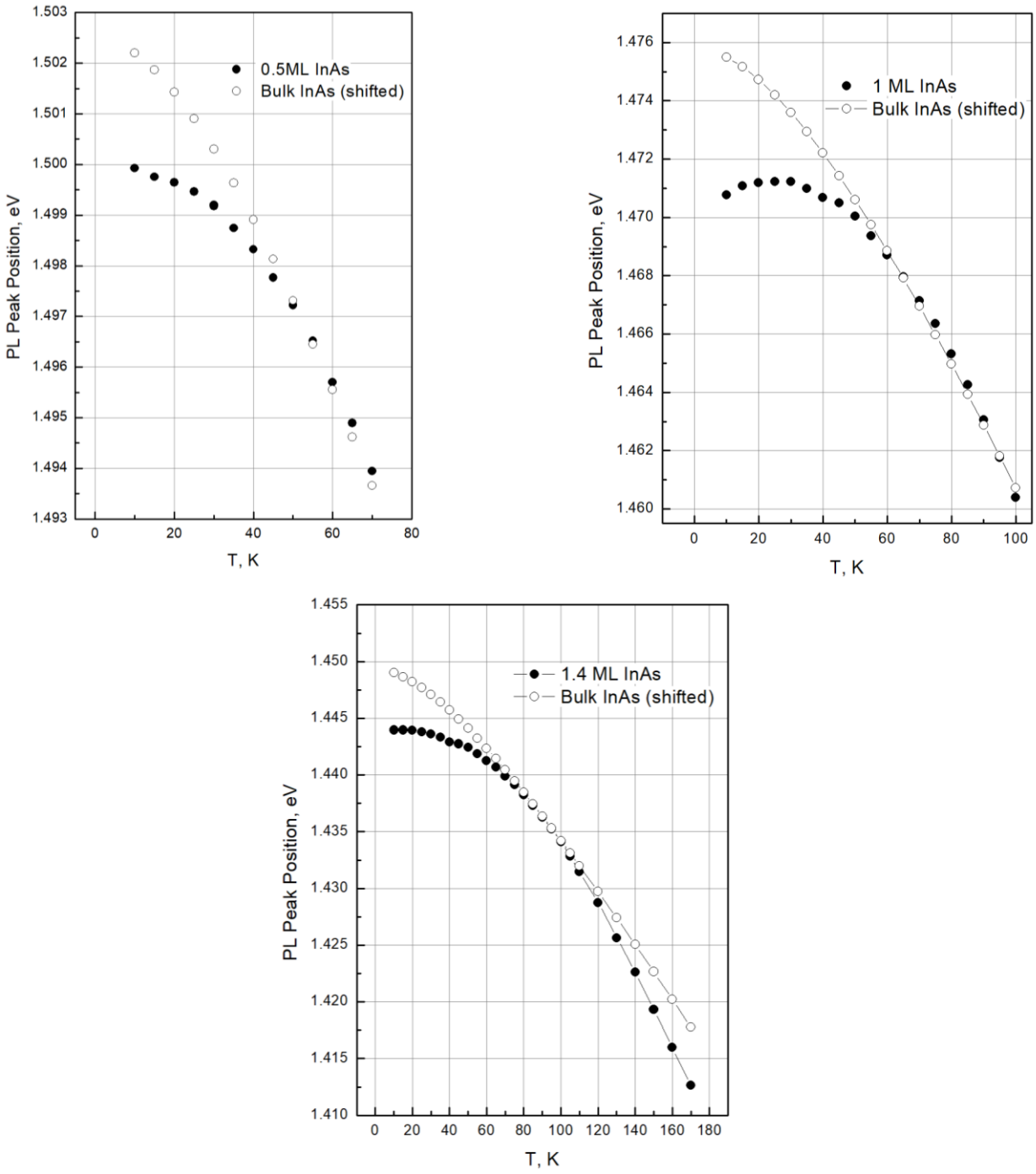

Figure 4.16. Temperature dependence of PL peak position (filled circles) evolution for samples S0.5ML, S1ML, and S1.4ML. Calculated temperature dependence of bulk InAs bandgap is shown as empty circles.

The temperature dependent PL efficiency parameter was utilized in order to calculate the thermal activation energy. The PL efficiency was calculated as an area under the PL peak curve corresponding to the temperature of the sample. The resulted integrated PL peak area as a function of 1000/T, where T is the corresponding temperature of the sample, is presented in Fig. 4.17 for samples S0.5ML, S1ML, and S1.4ML. The data have been fitted by using Arrhenius formula involving one high temperature carrier escape mechanism:

$$I(T) = \frac{I_0}{1 + C\exp(-E_A / kT)}, \qquad \text{(Equation 4.8)}$$

where T is the temperature of the sample during the measurement, $I(T)$ is the temperature dependent integrated PL emission intensity, I_0 is a variable parameter, which represents the PL intensity at relatively high temperatures, k is Boltzmann's constant, C is the ratio of nonradiative to radiative recombination probabilities, and E_A is the thermal activation energy. By plotting the data in a semi-log scale, the linear relation is more prominent at higher temperature range (lower values of $1000/T$). As a result, by neglecting the constant factor in the denominator, Equation 4.8 transforms to the following:

$$\log I = A + E_A / kT, \qquad \text{(Equation 4.9)}$$

from which the activation energies for each sample were determined from the slope of the fitted line at high temperature range as shown in Fig. 4.17 as solid black lines. Considering the GaAs emission energy at 1.517 eV, the sum of transition energy for each QW and corresponding activation energy is 7 – 9 meV higher than the GaAs band gap energy. This additional energy barrier can be corresponded to the band bending at the interfaces or the exciton binding energy.

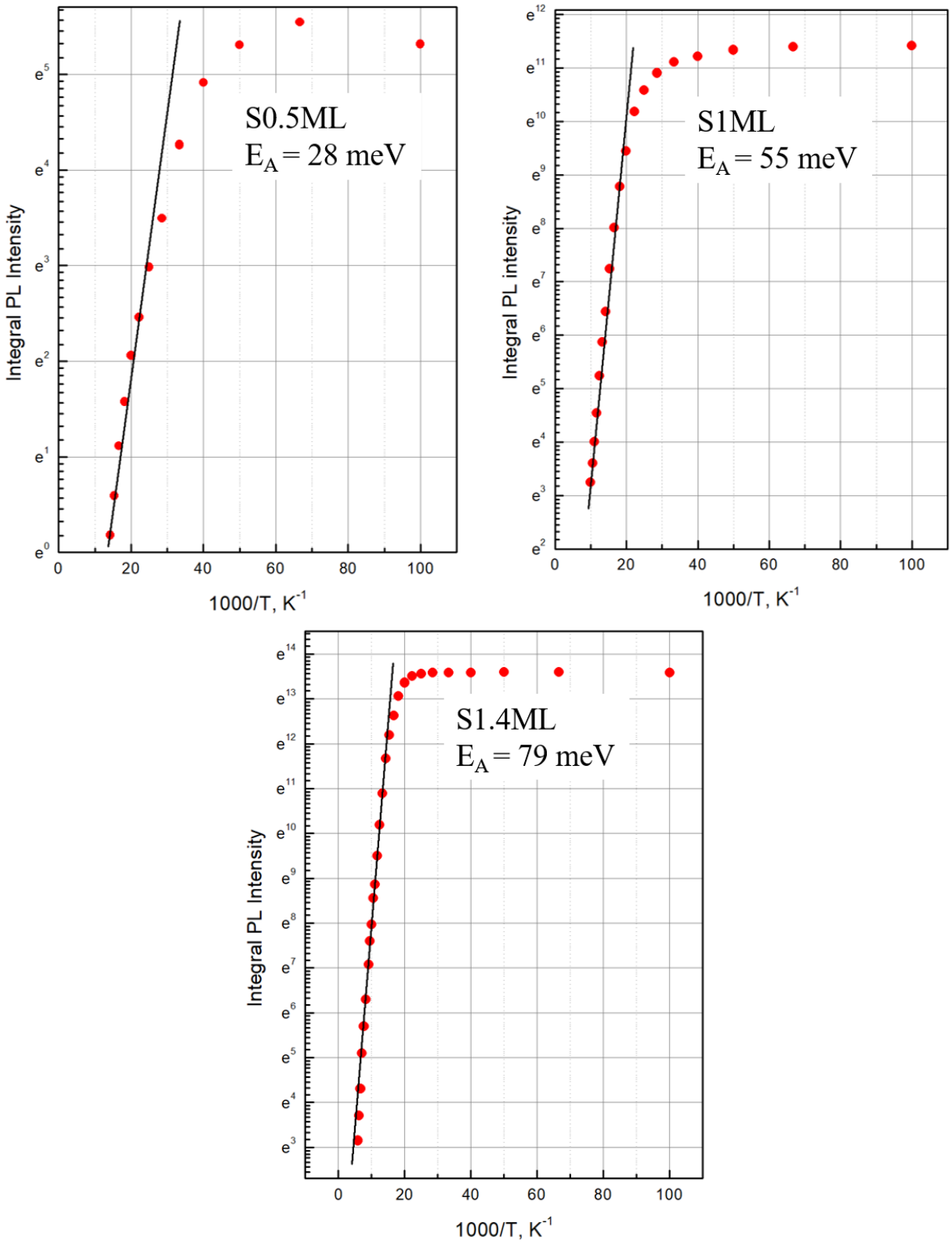

Figure 4.17. Temperature dependence of integrated PL peak area (filled red circles) evolution for samples S0.5ML, S1ML, and S1.4ML. The slope of the fitted black line was used to determine the activation energy for each sample.

4.5 Time resolved PL analysis of samples with varied InAs/GaAs QW thickness

Time-resolved PL (TRPL) measurements were performed for all five samples in order to study the decaying processes of recombination. The typical time dependence of spectrally integrated PL emission for sample S1ML is shown in Fig. 4.18. This measurement was performed under low temperature of 10 K using the medium excitation pulse intensity ensuring that the sample was not oversaturated. The time dependence of the laser pulse (shown in Fig. 4.18 as red curve) is characterized by the linewidth of 45 ps. This value is much larger than an actual pulse linewidth of 4 ps. Based on that, the system time resolution can be assumed to be

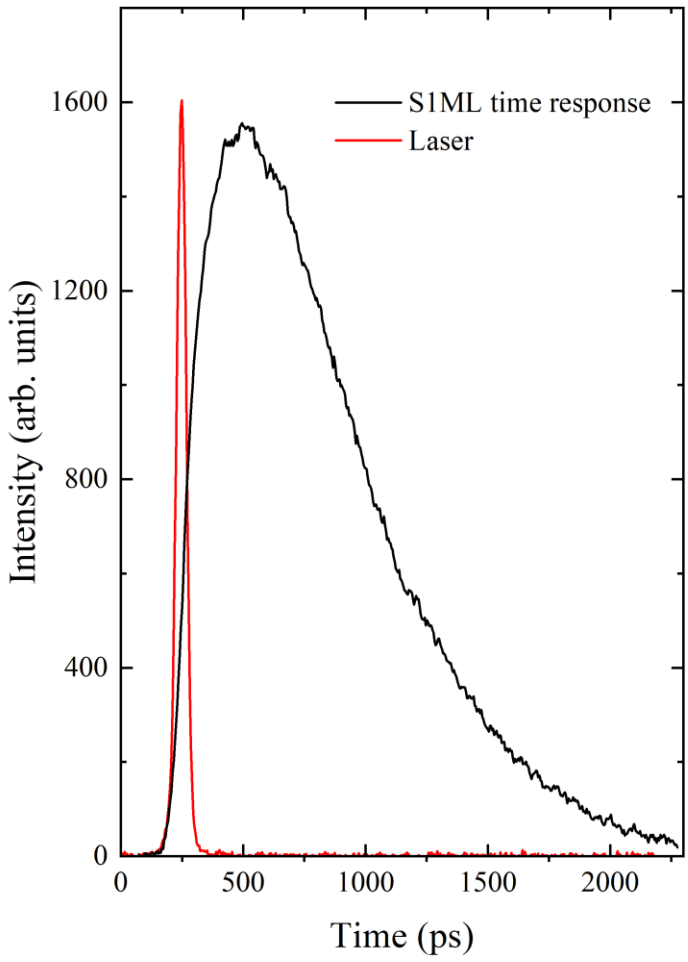

Figure 4.18. Time dependence of the spectrally averaged PL spectra (solid black curve) for sample S1ML. Time dependence of the laser pulse is shown in red solid line.

equal to 40 ps. Therefore, in order to accurately calculate the rise and decay times for each structure, the laser pulse curve must be deconvoluted from the spectrally integrated time dependent PL. The spectral integration was performed using the 2 nm spectrally wide window positioned at the wavelength which corresponds to the PL peak maximum position.

Accurate analysis of, and calculation of, the rise and decay times requires a sophisticated rate equation model, a schematic diagram of which is shown in Fig. 4.19. In this diagram, n_0 is the total number of carriers generated from the ground state $|0\rangle$ of the system (valence band of GaAs) by absorbing the laser pulse, n_2 is the generated number of carriers on the excited state $|2\rangle$. Carriers from the excited state undergo the non-radiative relaxation process characterized by the relaxation time τ_{21} to fill the energy state $|1\rangle$, which belongs to the InAs QW. Consequently, the carriers captured by QW with total number n_1 recombine with average lifetime of τ_{10}. Assuming the spectrally integrated PL intensity in Fig. 4.18 is directly proportional to the

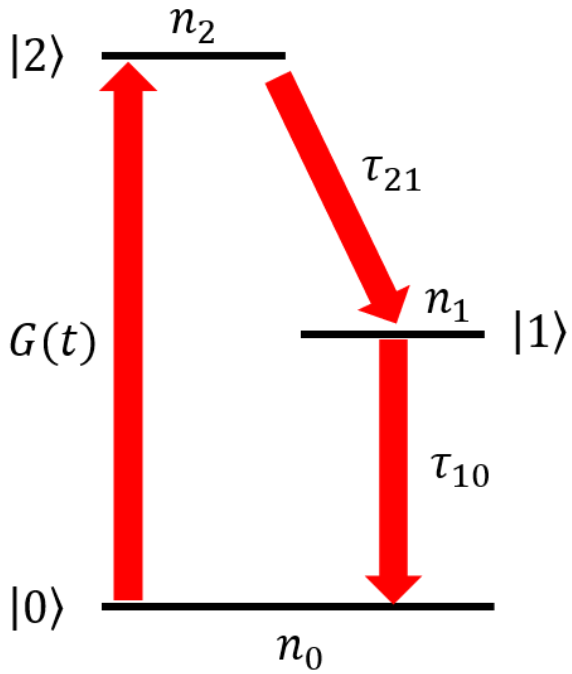

Figure 4.19. Schematic diagram of the simple three-level rate model.

number of carriers n_1, the transient curve can be used to determine supply τ_21 and decay τ_10 characterization lifetimes. Using the scheme in Fig. 4.19, the following system of rate equations can be written as:

$$\begin{cases} \dfrac{dn_2}{dt} = G(t)n_0 - \dfrac{1}{\tau_{21}}n_2 \\ \dfrac{dn_1}{dt} = \dfrac{1}{\tau_{21}}n_2 - \dfrac{1}{\tau_{10}}n_1 \\ \dfrac{dn_0}{dt} = \dfrac{1}{\tau_{10}}n_1 - G(t)n_0 \end{cases} \qquad \text{(Equation 4.10)}$$

The generation function $G(t)$ must follow the normalization property ensuring that all carriers will be generated over infinite time window, which can be written as follows:

$$\int_{-\infty}^{\infty} G(t)dt = 1 \qquad \text{(Equation 4.11)}$$

Ideally, the generation function $G(t)$ has the form of a delta function meaning all carriers were generated momentarily. In this case, the system of differential equations (Eqn. 4.10) will have the analytical solution which simplifies the analysis. However, the generation function holds the information about not only time profile of the laser pulse but also system response function which is the output of the system given the delta function-like input. The actual generation function was obtained from spectrally integrated laser pulse time profile. As can be seen from Fig. 4.18, the excitation time profile can be analytically represented by Gaussian distribution function. The resulting standard deviation parameter was found from best fit and kept constant for all calculations.

After introducing the Gaussian distribution function as the generation function $G(t)$, the system (Eqn. 4.10) can only be solved numerically. The numerical fitting process was

performed by using MATLAB software package. As a result, the rise and decay times were determined for each structure. Normally, the rise time did not exceed system resolution, which results in synchronization of the laser pulse maximum position and the transient peak position from the sample. However, as can be seen from Fig. 4.18, sample S1ML has a relatively large rise time which can be explained by the diffusion of excitons from GaAs matrix to InAs QW.

Using the described calculation method, the temperature dependent decay time analysis was performed for all five samples and shown in Fig. 4.20. The general feature for all structures is the slight decay time increase in the range of low temperatures followed by its decrease for the higher temperature.

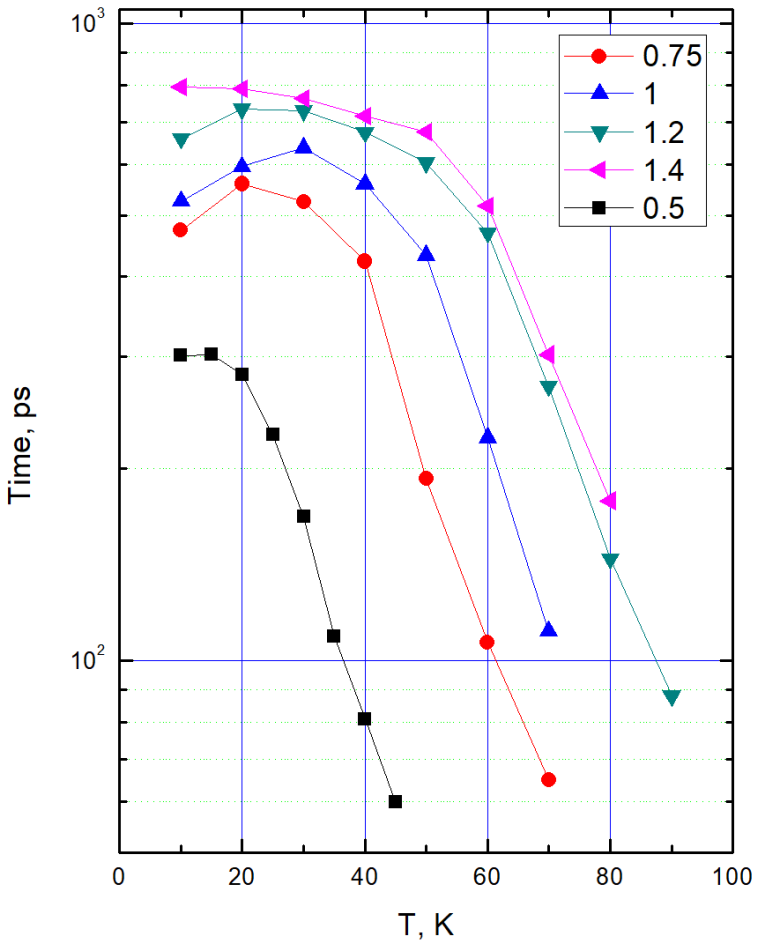

Figure 4.20. Temperature dependent PL decay time for all five structures of InAs/GaAs QW.

The general decay time trend under the fixed intensity and low temperature of 10 K is shown in Fig. 4.21. The lifetime of the carriers increased from 250 to 800 ps with the InAs QW thickness. The dependence follows a nearly linear trend with the slight deviation from non-linearity only for sample S1ML. The same explanation as for the PL linewidth can be also applied here. The interface smoothness reduces the carrier trapping probability, resulting in a shortening of the lifetime. This behavior, however, contradicts with the results published by Yuan et al.[41] who reported exactly opposite well-width dependence of the PL decay time.

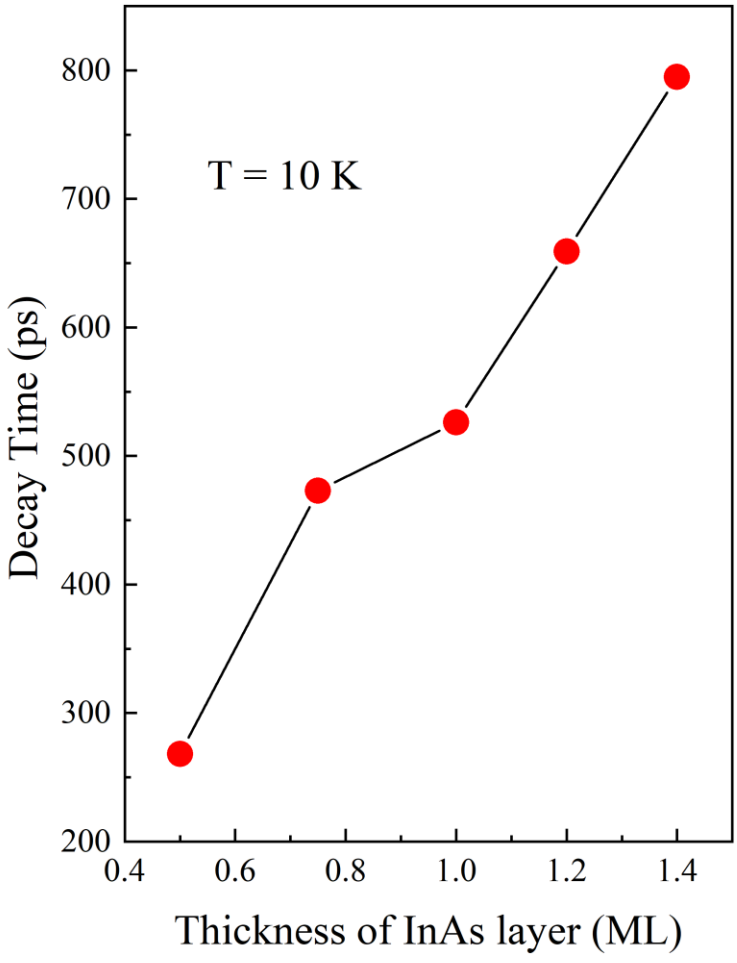

Figure 4.21. Photoluminescence decay time dependence as a function of the nominal thickness of InAs QW layer. The data were taken under the fixed conditions for each sample.

Chapter 5: Optical Properties of Ultrathin In(Ga)As/GaAs QW with Fixed Amount of Indium: The Effect of Segregation

Until this stage, the nature of InAs layer formation remains unclear. The two possible mechanisms described earlier are:

- the InAs islands formation that preserve their shape after being capped with GaAs and the indium
- the indium segregation mechanism that redistributes atoms of indium naturally creating the graded InGaAs QW layer.

All the physical properties that were discussed in Chapter 4 can be described and explained based on the mentioned In(Ga)As QW layer formation. Therefore, the main aim of this chapter is to provide physical evidence of one formation mechanism as opposed to the other. One of the reasons of high interest in this problem is the strong inconsistency in the literature. The discrepancy among scientific community relies on a fact that chemical intermixing related to the segregation is indistinguishable from the wave function intermixing for the closely arranged InAs islands.

The optimal design of the samples can potentially shine light on this problem. Admittedly, the PL experimental measurements cannot provide an irrefragable answer to this question. However, in combination with the numerical modeling of the PL response, one is able to provide quantitative analysis of differences and similarities of two possible formation models of In(Ga)As QW. This potentially opens the possibility of non-destructive structural analysis of ultrathin QWs that can outperform conventional XRD and TEM methods.

5.1 The description and justification of the growth design of the studied samples

In order to simplify further analysis, the samples for this study were designed by keeping the thickness of In(Ga)As/GaAs QW as a whole number of MLs. At the same time, the content of indium was calculated based on an idea that the total integrated indium content must be the same for all structures. The constant integrated indium content was chosen to be equal to the indium content needed to grow 1 ML of pure InAs (this exactly corresponds to the sample S1ML from the previous chapter). The four samples were grown in total with the QW layer thickness of 1, 2, 3, and 4 MLs with corresponded indium mole fraction of 1, 0.5, 0.33, and 0.25, respectively. In this chapter, for simplicity, the samples follow the naming convention based only on their nominal In(Ga)As QW thickness since the average indium content directly followed based on it. For instance, the sample S4 had the InGaAs/GaAs QW thickness of 4 MLs with the average content of indium calculated as $1.0/4 = 0.25 = 25\%$. However, it may be still unclear to the reader how this sample design can help in solving the structural characteristics of ultrathin In(Ga)As QW layer.

One of the reasons for choosing the whole number (integer) of MLs as the thickness of QW is the layer coverage. In case of sub-monolayer deposition of InAs, islands with random shape and size are formed. This randomness can be almost completely disregarded by fully covering the layer (merging all islands into one). The following capping process will either preserve the formed QW layer structure or modify it through a segregation mechanism. If the indium segregated, the effect of lateral segregation could be neglected since the whole layer coverage results in homogeneous indium content. As a result, the indium segregation, assuming it occurs, depends only on the vertical coordinate (perpendicular to the QW). Moreover, the corresponding QW band diagram can be shown and numerically analyzed in 1D.

5.2 Basic PL analysis of samples with fixed indium content

The PL spectra shown in Fig. 5.1 were measured for samples S1, S2, S3, and S4 with the constant total indium mole fraction. The offset has been applied to each of the spectra to better distinguish. The low-temperature PL spectra were recorded under the same medium excitation power intensity of 5 W/cm^2 and low temperature of 10 K. The samples S1, S2, and S4 showed strong single-peak emission at 1.471 eV, whereas the peak of the sample S3 was slightly shifted

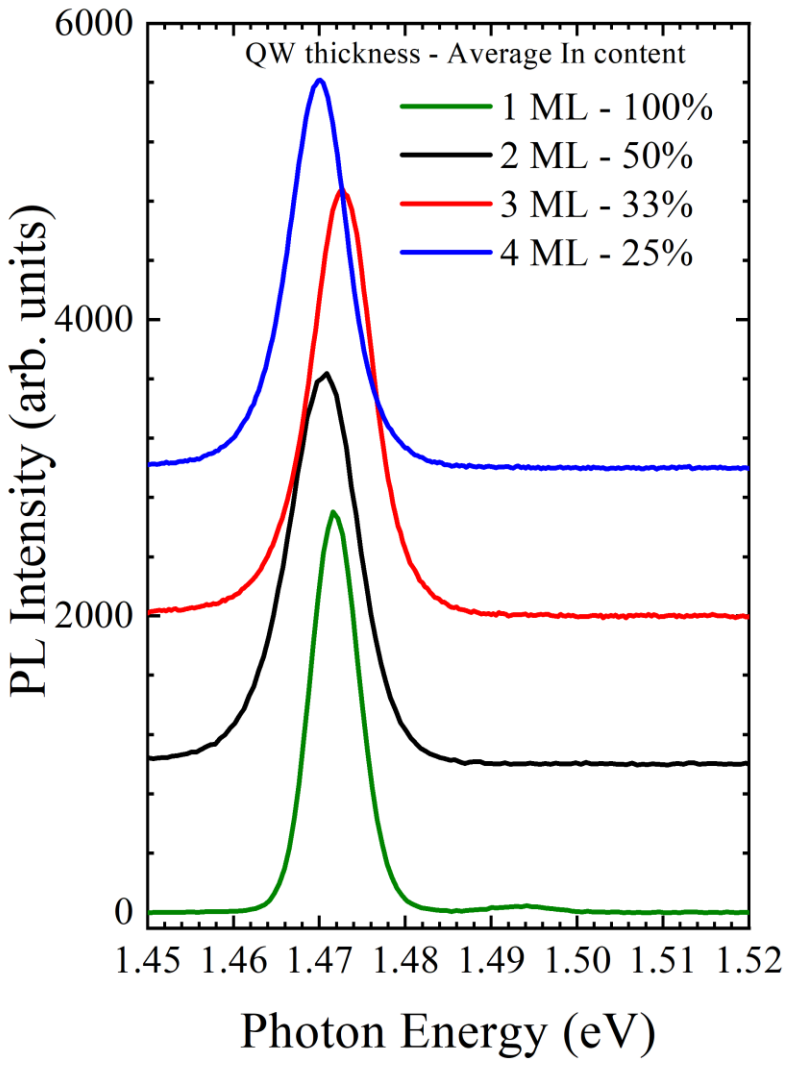

Figure 5.1. The PL spectra of four samples S1, S2, S3, and S4 plotted as a function of photon energy. The plots were stacked and separated from each other by a constant offset to better distinguish.

to 1.473 eV. These values represent inter-band ground state electron – heavy hole transition energy of the ultrathin In(Ga)As single QW. The error in the peak position is within the experimental error due to either the indium composition or the overall nominal QW thickness error during the growth. The average PL peak linewidth for all the samples was found to be 8 ± 2 meV. Such a narrow PL peak indicates constant QW thickness and lateral indium composition homogeneity within the QW.

The same PL peak position for each given sample was predicted during the structure design stage. Indeed, the reduction of the average indium content leads to increasing effective bandgap. This increase can be effectively compensated by the widening of the In(Ga)As QW so that the integrated indium content remains the same. This also can be visually shown in Fig. 5.2 as a schematic representation of the conduction band profile for five structures with fixed integrated indium content and QW thickness ranging from 1 ML to 5 MLs. The red dashed line shows the hypothetical ground state energy level for electrons. This energy level is common for each individual QW.

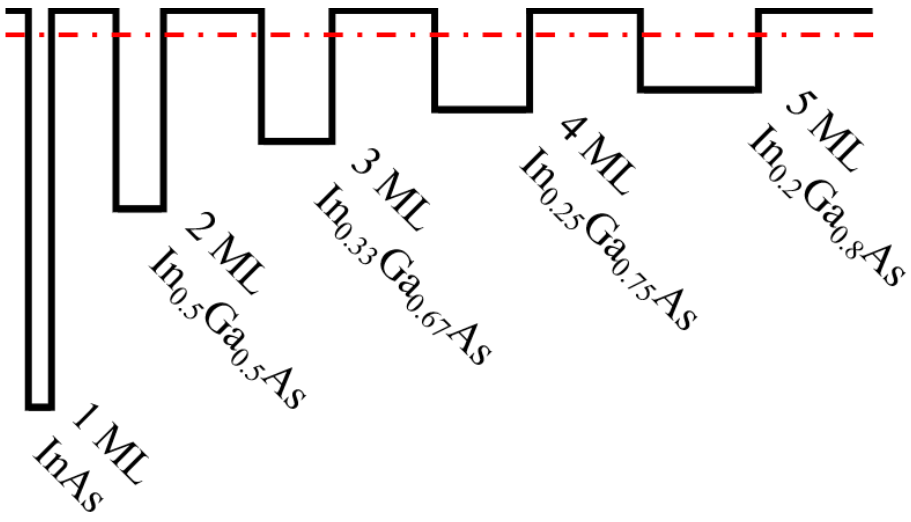

Figure 5.2. Schematic energy band diagram of independent In(Ga)As/GaAs QW. The red dashed line corresponds to the first electron energy level.

5.3 Effective energy simulation for the structure with fixed indium content without assuming the effect of the indium segregation

The common effective energy for samples S1, S2, S3, and S4 is a direct experimental result obtained from the PL analysis. It is also expected that the effective bandgap simulation for the given structures will provide the same transition energy. The reliability of the numerical approach is based on the fact that GaAs-based structures have been under active investigation for a few decades. As a result, the material parameters used in this study were taken from prior literature and calculated with a great precision. Therefore, numerical simulations based on such parameters is proved to be a reliable tool for predicting optical properties.

The actual effective bandgap simulation results are shown in Fig. 5.3. The simulation

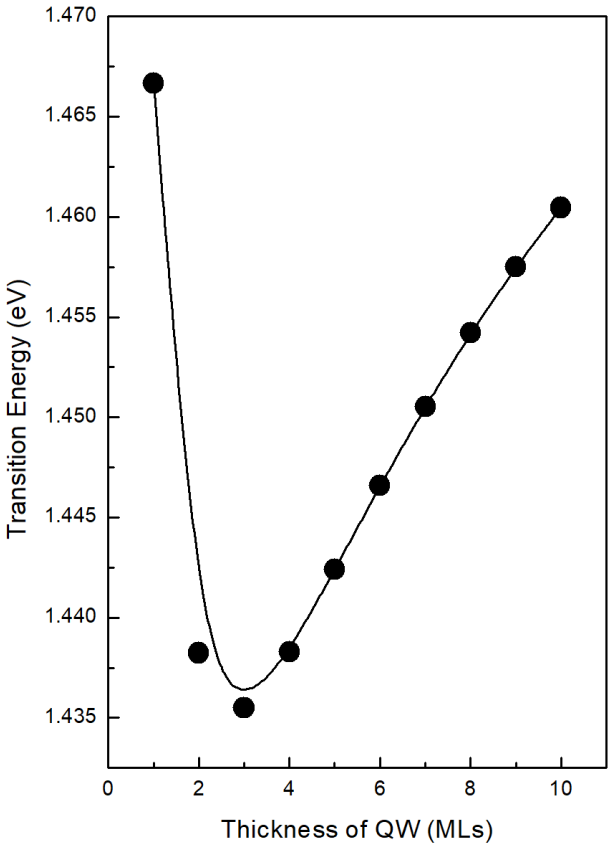

Figure 5.3. The effective bandgap simulation for the In(Ga)As/GaAs QW with constant total amount of indium as a function of QW thickness.

reveals a strong dependence between the effective bandgap and QW thickness which contradicts the experimental data. As can be observed from Fig. 5.3, the calculated transition energy (effective bandgap) for 1 ML thick QW is in a good agreement with the experimental PL data for sample S1. However, the calculated values are drastically different for S2, S3, and S4 equivalent structures. In these cases, the calculated effective bandgap is 30 meV lower that the PL peak position. From a numerical point of view, this is the result of an interplay between two effective bandgap changing processes. The first process is the effective bandgap reduction due to the increasing average indium content. The second process is the effective bandgap increase due to the QW thickness shrinking. The assumption about the common effective energy for all QW structures with constant total indium content was based on an equal effect of these processes, which effectively keeps the effective bandgap at a constant level. However, it is proved to be a false argument based on the simulation data shown in Fig. 5.3.

The effective bandgap simulation approach that does not rely on indium segregation (QW in this case has a rectangular shape) failed to explain the PL experimental data. However, this simulation provided a useful insight about the effect of indium redistribution on the effective bandgap. This opens the possibility to interpret the obtained PL results from a perspective of different shapes of QW given the constant integrated indium amount. The indium redistribution model must be the same for all structures and should be able to explain the obtained PL data as well as predict the optical properties of newly designed structures.

The uniform indium redistribution leads to the gradual effective bandgap increase as can be seen in Fig. 5.3 for the QW thickness that exceeds 4 MLs. When the total QW thickness is larger than 10 MLs (corresponding to the average indium content of less than 10%), the effective bandgap value approaches 1.47 eV (the experimental value obtained from the PL). This

indicates that the indium redistribution for more than 10 MLs is likely the cause for the constant effective bandgap. However, it is still unclear what indium chemical profile model is the most promising to simulate.

5.4 Indium segregation model

Until this point, the indium segregation was discussed in terms of indium redistribution resulting in the widening and deformation of the nominal chemical indium concentration profile. However, the qualitative analysis was provided without an actual physical model that is capable of explaining all the PL experimental data.

There are two most accepted models of indium segregation. The first theoretical model was proposed by Moison, et al.[47] in 1989. The foundation of their theory is based on the thermodynamical equilibrium. However, this model failed to explain some of the experimental results indicating that the physical processes occurring during the growth are far more complex. As a result, the more successful model was developed empirically by Muraki, et al.[48] in 1992. Their PL and the secondary ion mass spectrometry (SIMS) data show that the growth temperature is the primary component that determines the segregation level. In describing the indium content profile, the Muraki model provides better agreement with experimental data and is mostly used to provide a quantitative analysis of the segregation. The applicability of the given model was proved experimentally for the InGaAs/GaAs QWs with various growth conditions.

All consequent numerical analysis is based on the Muraki segregation model. Therefore, it is important to understand the key components of this model as well as investigate and apply it given the nominal structural parameters used in the current work. In order to simplify the

following discussion, the effect of indium desorption (reduction of the total indium content) has been neglected. This is the result of the relatively low growth temperatures of In(Ga)As QWs.

The idea behind the Muraki segregation model is quite simple. It assumes that some fraction R of indium atoms segregated to the next layer. The fraction R is called segregation coefficient. These atoms are replaced with the gallium atoms, which have the higher bonding energy. The rest of the indium atoms with fraction $1-R$ are considered to be fully incorporated to the crystal in the second surface layer. As follows from the definition, the segregation coefficient is within range from 0 to 1. When $R = 0$, there is no segregation, and the indium content profile has an initial intended shape. In contrast, $R = 1$ means that no indium incorporated in the structure. It is important to note that only the topmost layer takes part in the segregation process. All the other layers which are located underneath are finalized in terms of content distribution.

The step-by-step process of InGaAs layer formation is shown in Fig. 5.4. Although the deposition and segregation are shown as separated processes, they occur simultaneously. In order to better understand the segregation process, the deposition of a few first layers is described as follows:

- As for the first layer, $x_1 = (1-R)x_0$, where x_1 is the indium concentration in the first layer (more generally x_i is the indium concentration in the i-th layer) and x_0 is the average nominal indium concentration per layer which is assumed to be constant. The rest of indium Rx_0 is transferred to the next layer.
- The concentration of indium that has been incorporated in the second layer can be represented as $x_2 = (1-R)(x_0 + Rx_0) = (1-R^2)x_0$. The rest of indium $R(x_0 + Rx_0)$ segregated to the next layer.

- For the third layer, $x_3 = (1-R)(x_0 + R(x_0 + Rx_0)) = (1-R)(1+R+R^2)x_0 = (1-R^3)x_0$. The rest of indium $R(1+R+R^2)x_0$ is segregated.
- Generally, for the k-th layer, $x_k = (1-R^k)x_0$ content of indium incorporated to the layer, and $R(1+R+R^2+...+R^{k-1})x_0$ is transferred to the next layer. However, this calculation is applicable only for cases $k \le N$, where N is the nominal thickness of In(Ga)As layer in MLs.
- The indium concentration for the last layer before the growth of pure GaAs is evaluated as $x_N = (1-R^N)x_0$.
- The situation changes after reaching $N+1$ layer. This, and all consequent layers, have no additional supply of indium. All indium that eventually incorporated in these layers is coming solely from previous layer due to the segregation. For instance, the indium content for the $N+1$ layer can be written as $x_{N+1} = R(1-R^N)x_0$.

All in all, the general form to calculate the indium content in the n-th layer is represented as follows:

$$x_n = \begin{cases} x_0(1-R^n) & n \le N \\ x_0(1-R^N)R^{n-N} & n > N \end{cases}. \qquad \text{(Equation 5.1)}$$

This equation has only one parameter to vary – segregation coefficient R. The rest of the variables (x_0 and N) are the predefined parameters that are established before sample growth. In terms of samples S1, S2, S3, and S4, the average indium content evaluated as $x_0 = 1, 0.5, 0.33, 0.25$ and the In(Ga)As nominal layer thicknesses in MLs are $N = 1, 2, 3, 4$, respectively. In addition, the growth defined variables x_0 and N lock the amount of total indium in the system, so that the integrated indium content value is always equal to $x_0 \times N$. This value

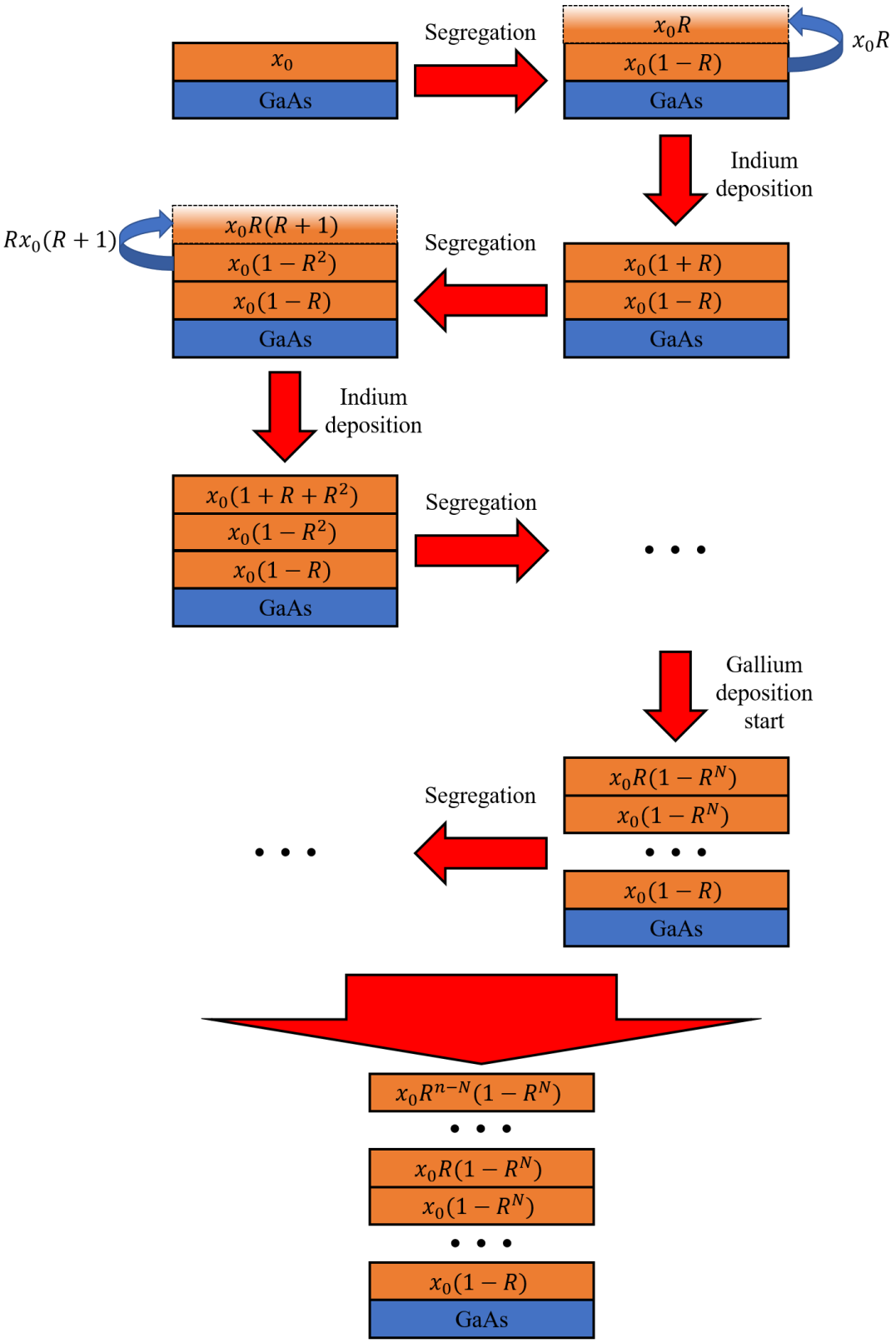

Figure 5.4. The schematic diagram of the In(Ga)As layers formation assuming the segregation model developed by Muraki et al.[48]

will not be affected by the segregation coefficient and can be treated as an invariant of a structure.

The effect of segregation coefficient R on the indium profile shape is demonstrated in Fig. 5.5. The structure identical to S1 was chosen in order to explore the difference in the indium redistribution. The natural composition profile has a step-like shape due to the fixed amount of indium within the single layer. However, for the purpose of clarity, all profiles have been plotted as smooth curves. The profiles for different values of R and fixed parameters x_0

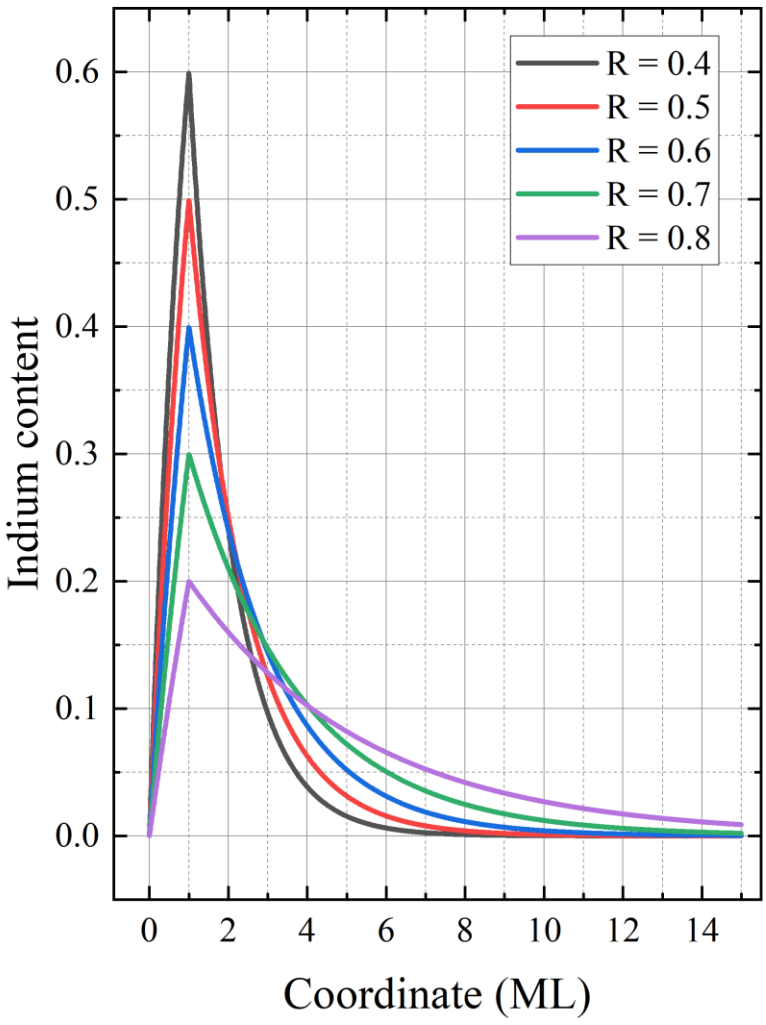

Figure 5.5. The indium profile evolution plotted for different segregation coefficients ranging from 0.4 to 0.8.

and N share the same vertical coordinate of the indium content maximum. In case of structure S1, the indium content maximum equal to $(1-R)$. The profiles for higher values of R are characterized by increased asymmetry.

In general, it is reasonable to assume that the segregation coefficient R is a function of numerous growth parameters including: the growth temperature, flux of indium (gallium) and arsenide, and the content of indium in the previous layer. For simplicity, the effect of the latter is neglected so that $R \neq R(x_n)$. More generally, the discussed segregation model assumes that the segregation coefficient does not depend on the nominal average indium content x_0 and is strictly determined by the growth temperature. Given this model, the indium content profile for samples S1, S2, S3, and S4 must be calculated using the same values of R. As an example, the predicted profiles for the mentioned structures is plotted in Fig. 5.6. These profiles were calculated by using the constant segregation level $R = 0.8$, which is the generally accepted value given the growth temperature of 460 °C.

The changes in indium profiles are quite dramatic compared to the nominal rectangular shapes. For studied samples, the difference in indium content within the fifth layer counting from the first layer of In(Ga)As is within 5%. This difference is getting smaller for subsequent layers. This indicates that these layers are almost indistinguishable from sample to sample in terms of structural characteristics. The major difference comes from the shifted maximum of indium content. As follows from Fig. 5.6, the maximum shifts from first to fourth coordinate position (same as growth parameter N) for samples S1 and S4, respectively.

As a result, the obtained profiles can be used as an input for the numerical calculation of the effective bandgap. At first, the conduction and valence band edges were calculated utilizing the indium content profile as a function of x_0, N, and R. As an example, the energy band

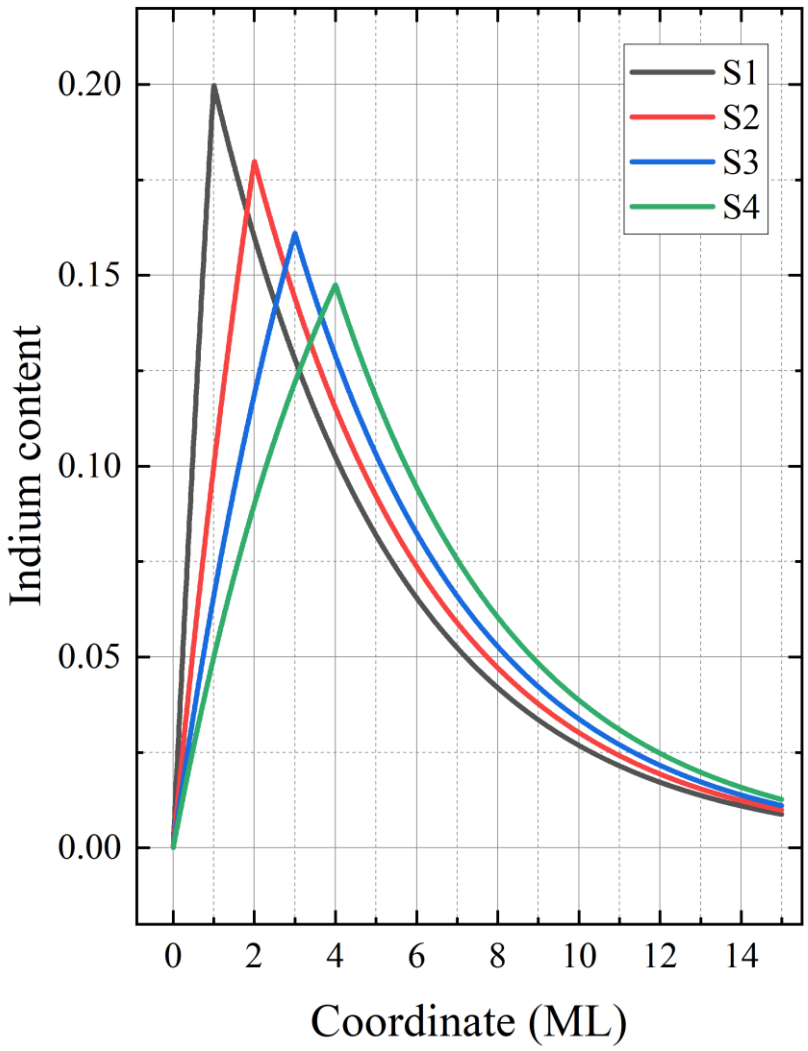

Figure 5.6. The indium profiles evolution plotted for structures equivalent to S1, S2, S3, and S4. The segregation coefficient is equal to 0.8.

diagram for the structure S1 $(x_0 = 1, N = 1)$, assuming the segregation level of 0.8, is presented in Fig. 5.7. In addition, the ground state energy levels with the corresponding wave functions are shown. Using these parameter configurations, the transition energy value (effective bandgap) obtained from the modeling is nearly equal to 1.47 eV. This value perfectly coincides with the experimental PL data. It is also the case for the non-segregation approach (rectangular QW). However, as was mentioned earlier, non-segregation numerical analysis only provided

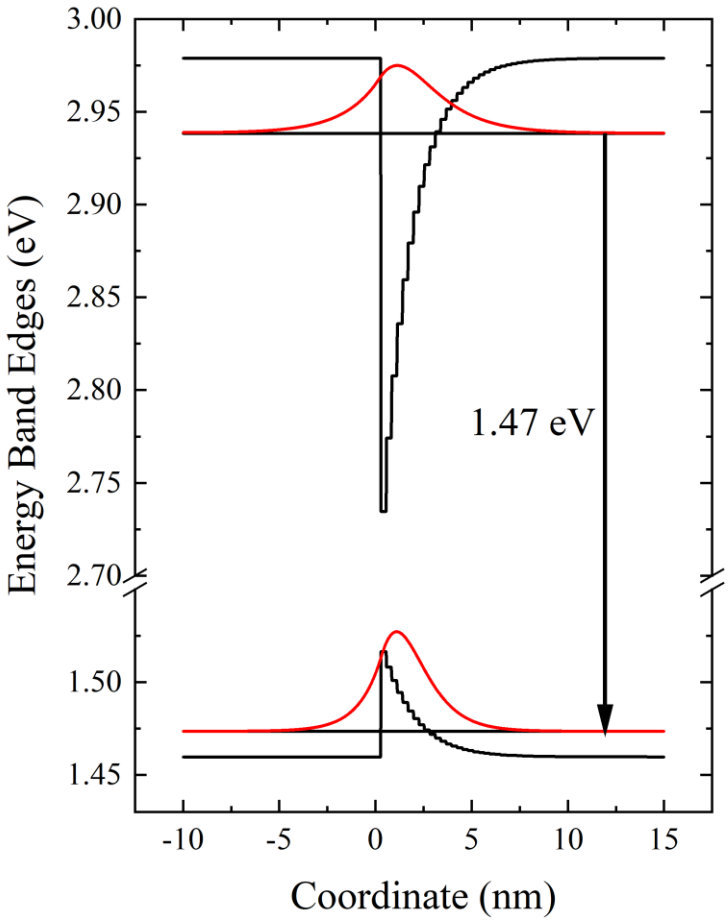

Figure 5.7. The energy band diagram with calculated energy levels and wave functions for the structure equivalent to S1. The segregation coefficient is equal to 0.8.

reasonable agreement for the sample S1. The rest of three samples have a noticeable calculated effective deviation from the experimental results. Therefore, it is important to explore the role of segregation coefficient on the calculated effective bandgap.

As was mentioned earlier, the parameters x_0 and N are predefined and based on the nominal structural characteristics during the growth process. Therefore, the only unknown parameter is the segregation coefficient R. Given the resulting energy band diagram, the effective bandgap can be obtained as a function of continuous variable R, so that

$E_{eff} = E_{eff}(x_0, N, R)$.

Figure 5.8 shows the simulation of the effective bandgap for the sample structures S1, S2, S3, and S4 as a function of the segregation coefficient. For each structure, the energy band diagrams (like the one shown in Fig. 5.7) were calculated for continuous value of R in the range of 0 and 0.9 using the indium content profile described by Eqn. 5.1. The simulated effective bandgap was obtained as the inter-band $e_1 - hh_1$ transition energy for the corresponding structure and the value of R. Without the segregation process $R = 0$, the simulated effective bandgap for

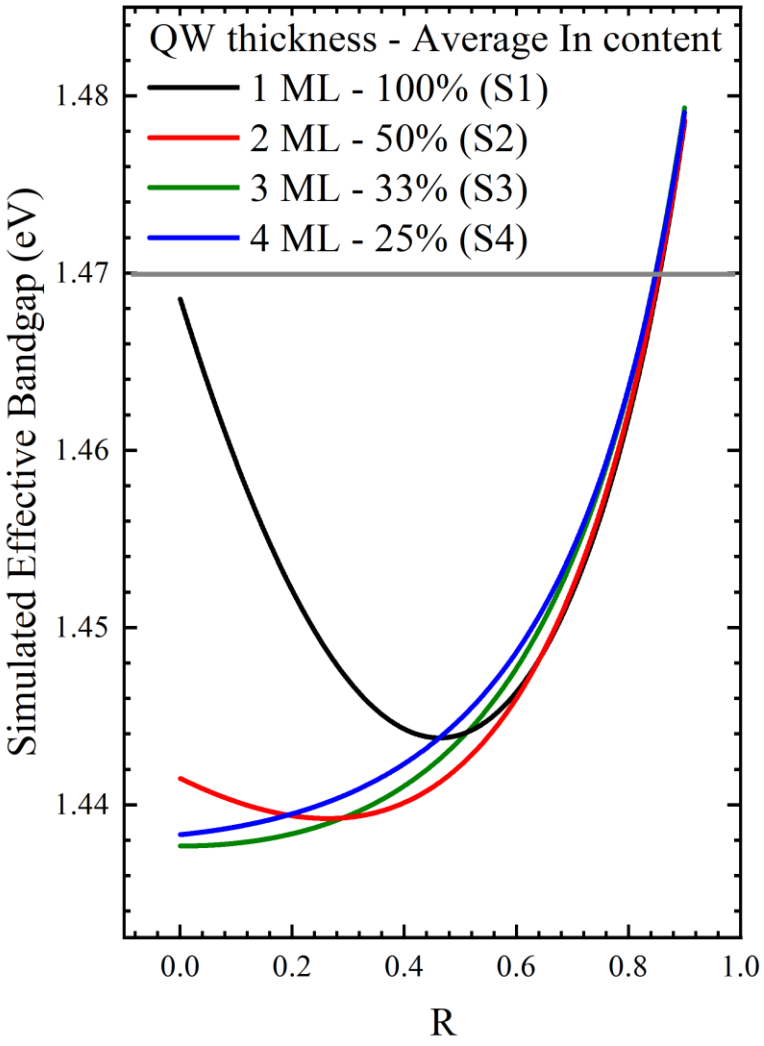

Figure 5.8. The simulated effective bandgap of four structures equivalent to S1, S2, S3, and S4 plotted as a function of segregation coefficient. The horizontal solid grey line shows experimental PL peak position for these samples.

the given structures varies from 1.438 to 1.468 eV as was shown earlier in Fig. 5.3. On the other hand, effective bandgap for all four structures is approximately equal for $R > 0.5$. The horizontal solid grey line represents the experimental value of effective bandgap extracted from the PL. Combining the experimental and simulated results, the segregation coefficient for all structures S1, S2, S3, and S4 with the same total indium composition is found to be equal to 0.83.

For clarity, the energy band diagrams at three different segregation levels with corresponding transition energies are shown in Fig. 5.9.

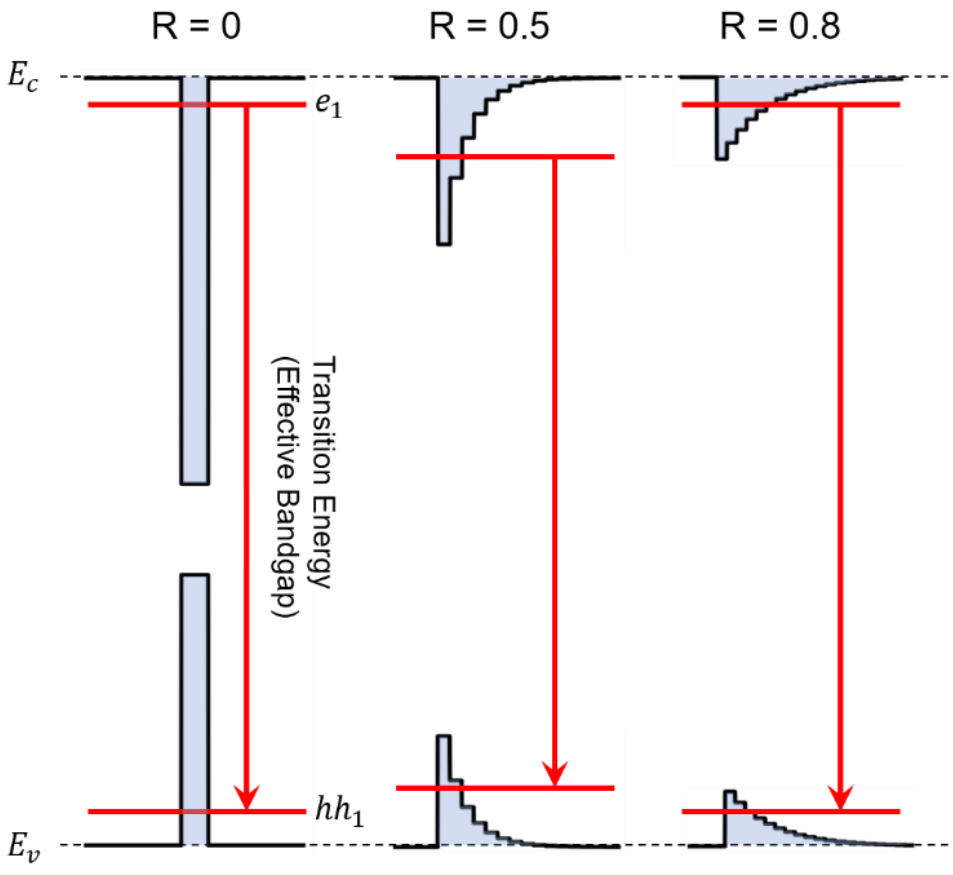

Figure 5.9. The energy band diagrams for structure equivalent to S1 calculated for different segregation coefficients.

It is important to note that having the simulated data for structure S1 only would be impossible to conclude whether or not indium segregation is taking place. The reason for that is the same simulated effective energy value in two regions: without segregation $(R = 0)$ and at high segregation level $(R = 0.83)$. Therefore, it was vital to have additional structures (S2, S3, and S4) to confirm the occurrence of the indium segregation mechanism.

The combination of the experimental PL data and the effective bandgap simulation proved to be a useful tool to not only confirm the segregation occurrence but also accurately determine quantitative parameters of segregation.

5.5 STEM analysis for probing the content depth profile of indium

Figure 5.10 shows the STEM intensity profiles as a function of the growth direction coordinate for two samples (a) S1 and (b) S2. The actual STEM images are shown as insets for the corresponding sample. The InGaAs QW is shown as a brighter region in the image due to the indium incorporation in that area. The data (open red circles) represent the intensity extracted from STEM image averaged over the area shown in the insets. The zero-coordinate position is set to coincide with the first interface of the InGaAs QW. The experimental data were fitted according to the segregation model described by Muraki et al.[48] and given by Eqn. 5.1. Since x_0 and N parameters are predefined during the structure design, the segregation coefficient R was used as the fitting parameter. The segregation coefficients that were extracted from the best fit following the least squares approach are 0.85 and 0.81 for samples S1 and S2, respectively. The found values are in a good agreement with the segregation coefficient extracted from the PL analysis technique. The latter, however, has an obvious advantage since it is fast and non-destructive approach that does not require the tedious sample preparation process.

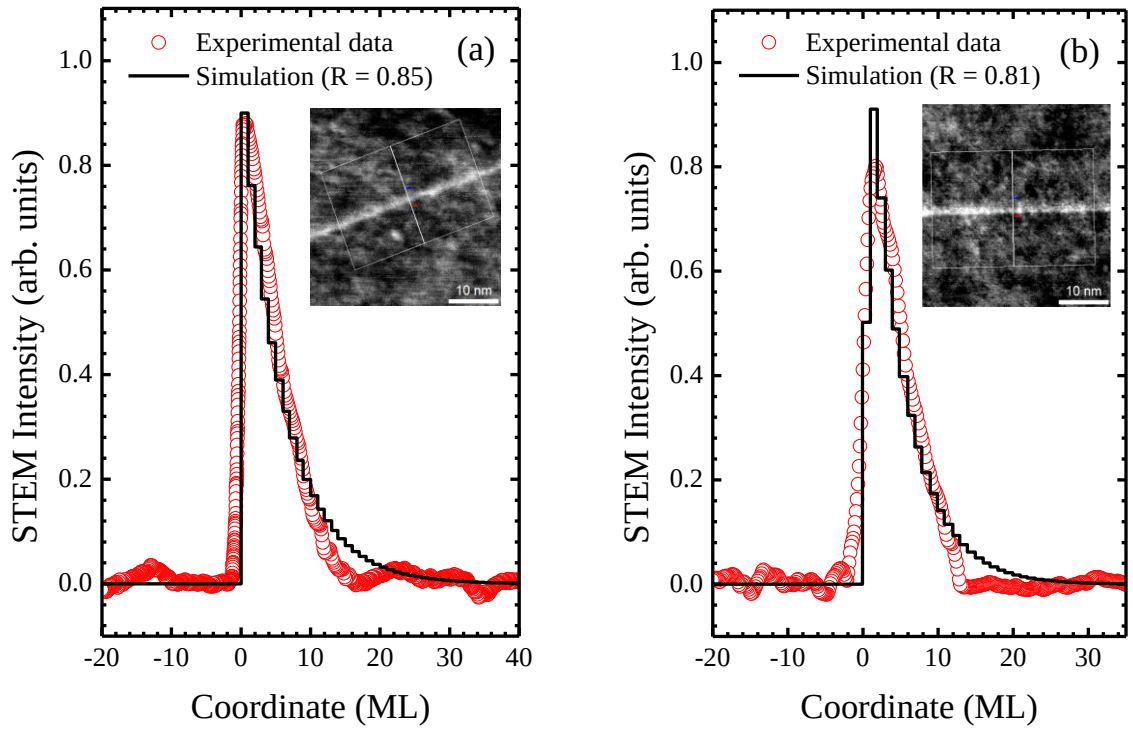

Figure 5.10. The STEM intensity profiles of samples (a) S1 and (b) S2 plotted along the growth axis. The insets show actual STEM images of In(Ga)As QW region.

5.6 Indium segregation for structures grown at different temperatures: The effect of GaAs capping design

At this point, the useful non-destructive technique to accurately calculate segregation coefficient has been established for ultrathin InGaAs/GaAs QW structures. In order to check the goodness of the proposed approach, it can be applied to the structures with the different segregation levels. As was mentioned earlier, the best way to achieve noticeable changes in the segregation coefficient is to change the temperature during the QW growth. The first three samples S1, S5, and S6 were grown at different QW temperatures. The specific information about the growth as well as some important growth parameters can be found in Table 2.1 in Chapter 2. It is important to mention the designed thickness of low-temperature (the same

temperature as for the QW) GaAs cap layer which was kept constant for these samples and resulted in 35 MLs. Since the growth temperature for this layer remained unchanged, it is safe to assume that the segregation coefficient remained constant as well. Due to the nature of segregation, the indium content after the 35th layer was close to zero. As a result, all remaining indium after the low-temperature GaAs cap layer practically does not affect the effective bandgap. The subsequent increase of the growth temperature to grow the remaining GaAs layer would not affect the shape of the buried indium profile and corresponding effective bandgap.

The PL spectra were recorded for these three samples. The resulting normalized PL peaks are plotted in Fig. 5.11. The growth temperature decrease leads to the PL peak red shift.

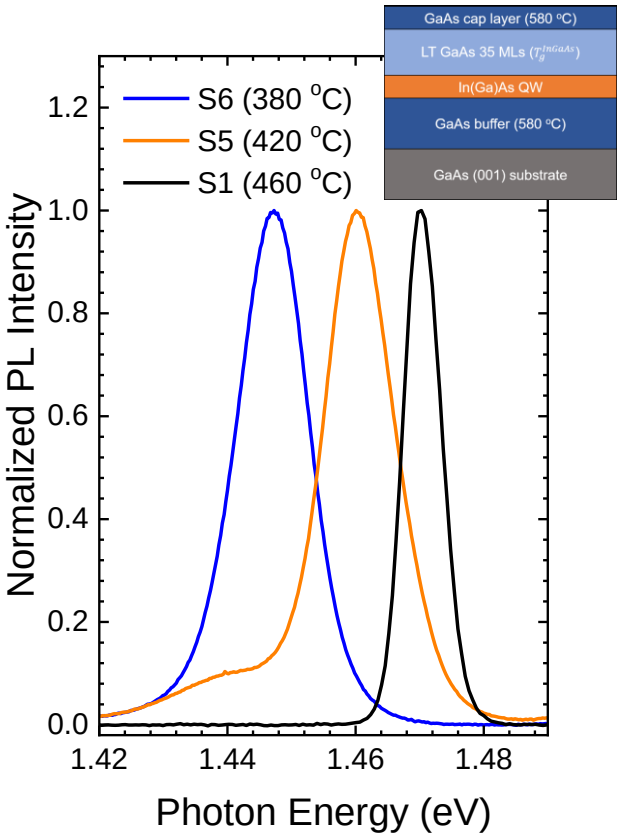

Figure 5.11. Normalized low temperature experimental (10 K) PL spectrum measured for InAs/GaAs QWs with 35 MLs LT GaAs cap layer grown at 380 °C (S5), 420 °C (S6), and 460 °C (S1).

The reason for such shift is the difference in segregation coefficient. Based on the Muraki segregation model, all three samples had the same structural parameters ($N = 1, x_0 = 1$). Therefore, the dependence in Fig. 5.8 that corresponds to the curve S1 can be reused to determine the segregation coefficients for all samples independently. The resulting segregation coefficients were found to be equal to 0.6, 0.79, and 0.83 for the growth temperatures 380 °C, 420 °C, and 460 °C, respectively. The found coefficients are in a good agreement with the temperature dependence of indium redistribution published by other research groups. This PL data experimentally proves the strong effect of the indium redistribution on the optical properties of the structure, as well as opens interesting possibilities to bandgap engineering.

One of the possible ways to control the effective bandgap relies on the thickness variation of the LT GaAs cap layer. The next set of samples were designed to test the effect of LT GaAs cap layer thickness, as well as provide full optical analysis of these structures based on the established segregation model.

For the next set of three samples, the LT GaAs cap layer was set to be four MLs. The samples were named as S8, S9, and S7 and had the rest of the growth parameters exactly the same as for S5, S6, and S1, respectively. The remaining GaAs was grown at the higher temperature of 580 °C. Practically, it means that any indium atoms could not be incorporated to the structure due to the high temperature. The normalized PL spectra for structures S8, S9, and S7 is shown in Fig. 5.12. As expected, the PL peak positions for all three samples were blue shifted with respect to their corresponding structure with sufficiently thicker LT GaAs cap layer. The reason of such shift could be attributed to the indium profile cut-off which efficiently reduced the content of indium after 4th ML of GaAs to zero. As a result, the effective bandgap simulation could be performed with a modified content profile.

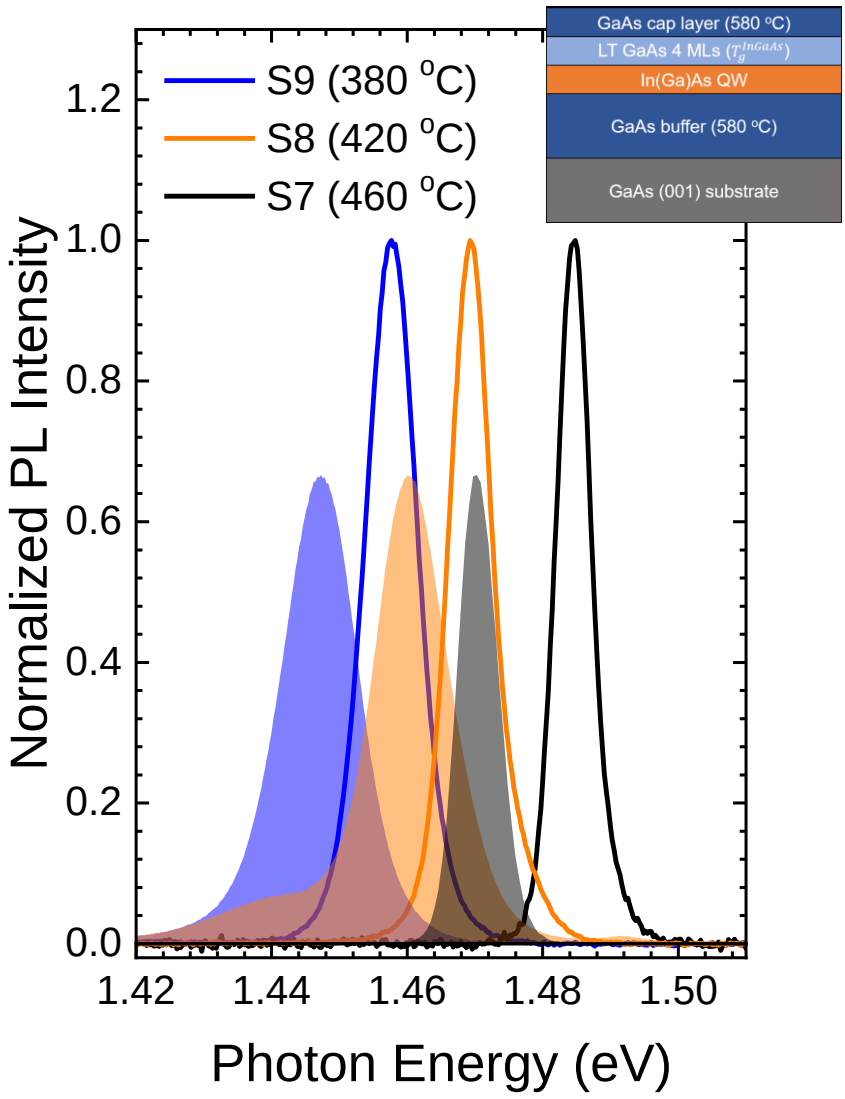

Figure 5.12. Normalized low temperature experimental (10 K) PL spectrum measured for InAs/GaAs QWs with 4 MLs LT GaAs cap layer grown at 380 °C (S8), 420 °C (S9), and 460 °C (S7).

The effective bandgap simulation was performed for structures S7, S8, and S9. Since the growth temperature remained the same as for the corresponding samples, it is reasonable to assume that the segregation coefficient was also the same for every pair of corresponding samples. The indium profiles, however, had to be modified to reflect the LT GaAs thickness effect. The resulting profiles for all six structures are plotted in Fig. 5.13.

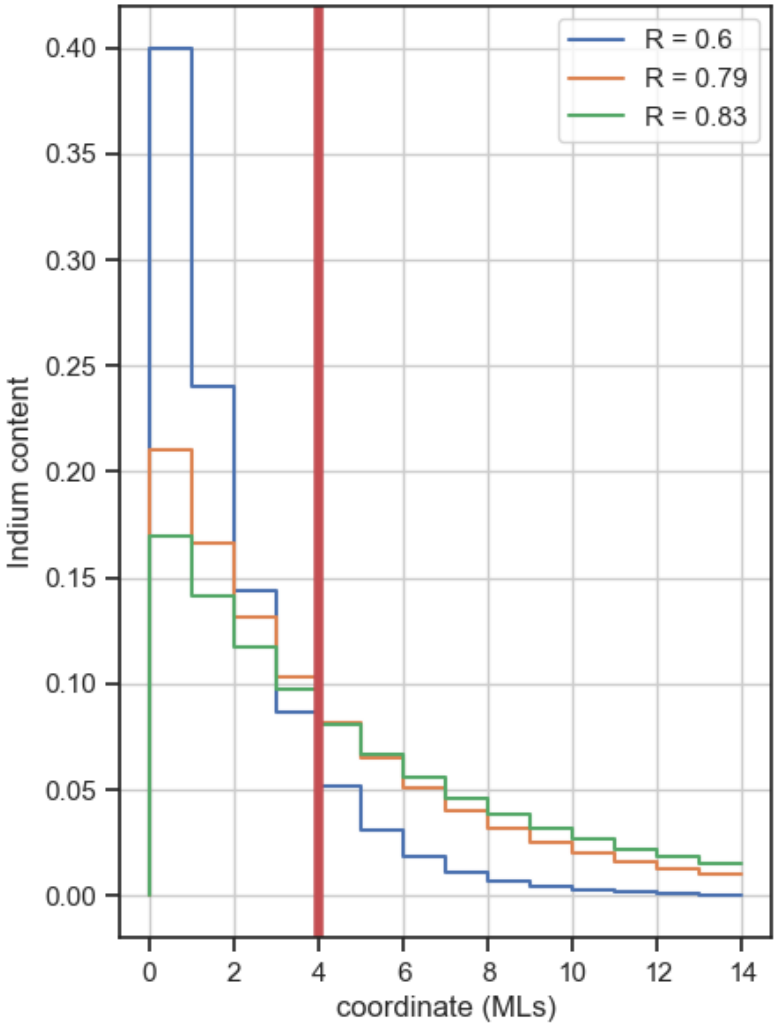

Figure 5.13. The indium content profiles used to simulate the effective bandgap for samples S1, S5, and S6. The red vertical line shows the layer after which indium cannot be incorporated.

In terms of simulation, the difference between the two sets of samples grown at different temperatures is reflected in indium profile modification after the vertical red line in Fig. 5.13. By setting the indium content after this line to zero, the resulting profiles have been used to generate the energy band diagram for each sample. The obtained simulated effective energy and the actual experimental data gathered from PL are summarized in Table 5.1. for different growth temperature samples with four MLs LT GaAs cap layer.

Table 5.1. The calculated and experimental transition energies for samples grown at different temperatures.

Growth temperature (°C)	R	Calculated Transition energy (eV)	PL peak position(eV)
380	0.62	1.457	1.456
420	0.78	1.469	1.467
460	0.83	1.485	1.483

The calculated transition energy values are in a perfect agreement with the experimental PL peak positions. This indicates that the proposed PL technique is a reliable tool for determining the indium depth profile with a high accuracy.

5.7 Summary

In summary, the indium segregation effect on PL properties was investigated for ultra-thin InGaAs/GaAs QWs grown by MBE. It was shown that the PL peak positions were identical for the structures with the same nominal amount of indium. The effective bandgap simulation performed for the latter structures was in a good agreement with the PL data for a fixed segregation coefficient. The described method is the unique approach to probe the indium depth profile. This technique can be successfully applied to the ultrathin QWs based on a variety of different materials. The indium content profiles extracted from STEM data were utilized to determine the segregation coefficient experimentally. The obtained values of the segregation coefficient were consistent with the effective bandgap simulation combined with the PL data. The PL for the samples grown at different temperatures was utilized to obtain segregation coefficients from the simulation. It was shown that the indium content profile could be

effectively modified by controlling the thickness of the LT GaAs cap layer.

Chapter 6: Optical Properties of Ultrathin In(Ga)N/GaN Multi QW: The Effect of the Growth Temperature

GaN, a direct energy band gap semiconductor, allows the formation of the ternary and heterostructures when paired with InN and AlN. Thus, it can be applied to optoelectronic as well as high frequency, high power electronic devices. In addition, the III-nitride materials provide broad spectral coverage, from the visible light into near ultraviolet. The refinement of these materials offers the potential for novel blue and ultraviolet detectors and emitters. Therefore, GaN is an excellent choice for most wide band gap semiconductor device applications in both optoelectronics and high-frequency power electronics.

Due to the emerging importance of gallium nitride (GaN) in both optoelectronic and high-frequency electronic device applications, numerous studies have recently been done to explore the properties and to refine the technology of GaN. However, the realization of the full potential of GaN and its related compounds is still in its infancy. Therefore, contemporary academic society is very interested in finding any new approach to predict physical properties of new systems based on GaN or to improve characteristics of existing ones.

There is a strong need for photonic emitters in the blue and ultraviolet portions of the spectrum. GaN-based structures, particularly InGaN quantum wells in a GaN matrix, are found to be extremely useful to develop a coherent blue light source for laser printers, and of a read-write laser source for high-density optical mass storage systems. Shorter wavelength emitters extend the diffraction limit for optical systems thus enabling more compact storage of information. The importance of developing blue and ultraviolet photon detectors is growing as well. Moreover, the wide band gap semiconductors, principally GaN and AlGaN, offer attractive alternatives for solar-blind ultraviolet detection.

6.1 General optical properties of ultra-thin In(Ga)N/GaN MQW structures

The ultra-thin In(Ga)N/GaN MQW structures are recently under active research. Although the InGaN quantum well structures have attracted much attention due to their unique optical and electrical properties, the fabrication process is still extremely challenging. Such difficulties are due to the strict requirements of the interface quality, constant alloy composition, and uniform quantum well thickness. The fundamental theoretical analysis shows that the emission from pure ultra-thin InN quantum wells embedded in GaN matrix can cover the whole visible spectrum range (400-750 nm). This is possible due to the significant difference in band gap energies for InN (0.65 eV) and GaN (3.4 eV) at room temperature. The lattice mismatch, however, is quite significant and equals to 12%, which is much larger that the InAs/GaAs mismatch of 7%. The band gap energy and the corresponding lattice parameter is shown in Fig. 6.1. Theoretically, the whole visible spectrum coverage can be achieved by designing the InGaN/GaN quantum systems with different indium content. However, in practice, the grown structures do not show the desired efficiency due to the high dislocation density.

The ongoing research in this area might shed light on the so-called "green gap problem," which relates to the large LED efficiency drop within the range of 500-600 nm as shown in Fig. 6.2. Nowadays, the majority of the commercial screen panels use the RGB matrix, each pixel of which consists of three sub-pixels with different colors (R - red, G - green, B - blue). Therefore, by increasing efficiency of the green sub-pixels to the level of around 80% as for blue or red LEDs, the power consumption of the panel will decrease by approximately 20% in average. In order to solve the green gap problem, the studies in this direction focus on complex structural analysis based on TEM and XRD analysis, optical characterization (PL and cathodoluminescence), and first principle simulation. The experimental results from a few research groups show that indium content is limited to about 35%. The exact process of such

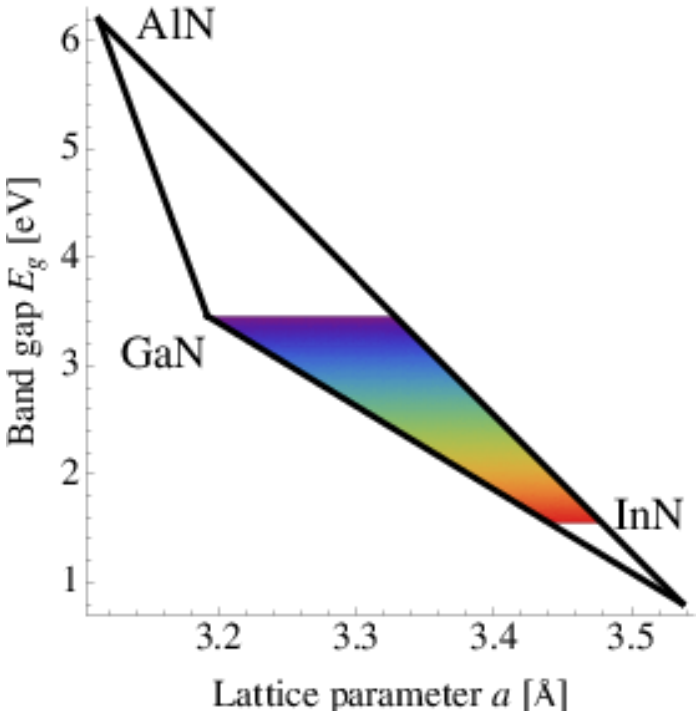

Figure 6.1. The bandgap and the corresponding lattice parameter for the III nitride-based compounds and their alloys (AlN, GaN, and InN).

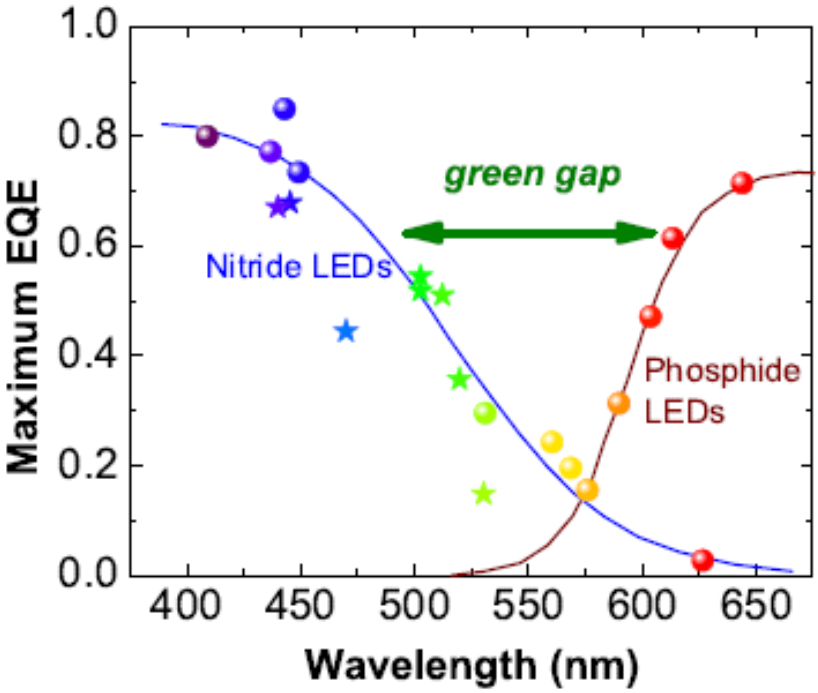

Figure 6.2. Maximum external quantum efficiency for the most used commercial LEDs.

limitation can include indium desorption, segregation, and indium-gallium inter-diffusion. It is still an open question what causes the self-limiting mechanism of In(Ga)N layer formation.

The fundamental theoretical analysis by using the solution of the Schrodinger equation shows that the emission from ultrathin In(Ga)N quantum wells embedded in GaN matrix can cover whole visible spectrum range (400 – 750 nm) as shown in Fig. 6.1. This is possible due to the huge difference in band gap energies for InN (0.65 eV) and GaN (3.4 eV) at the room temperature. By changing only one parameter, one can tune the effective band gap. For example, the change of In(Ga)N quantum well thickness can alter electron and hole energy levels and, consequently, transition energy as can be seen in Fig 6.3. It is worth mentioning the huge impact of strain on the effective bandgap value. The two effective bandgap dependencies were plotted assuming absence of strain and fully strained InN QW layers. However, this is not feasible due to the natural growth limitations such as critical thickness.

6.2 Optical properties of the bulk GaN

Before the discussion about optical properties of the ultrathin InN/GaN QWs, it is important to establish the full optical analysis of the bulk GaN. Due to the high dislocation density of the nitride-based materials, their PL emission is characterized by a few additional peaks that correspond to the emission due to the dislocation centers. Unlike the emission from bulk GaAs, the PL emission from the bulk GaN has additional peaks with lower emission energy compared to the main bandgap emission of 3.47 eV at low temperature.

The PL spectra of the undoped bulk GaN is shown in Fig. 6.4. The data was extracted from Reshchikov et al.[71] The near-band-edge (NBE) emission is at 3.47 eV. The defect-related PL peaks are located within the range of 1.5 to 3.3 eV. The emission intensity of these

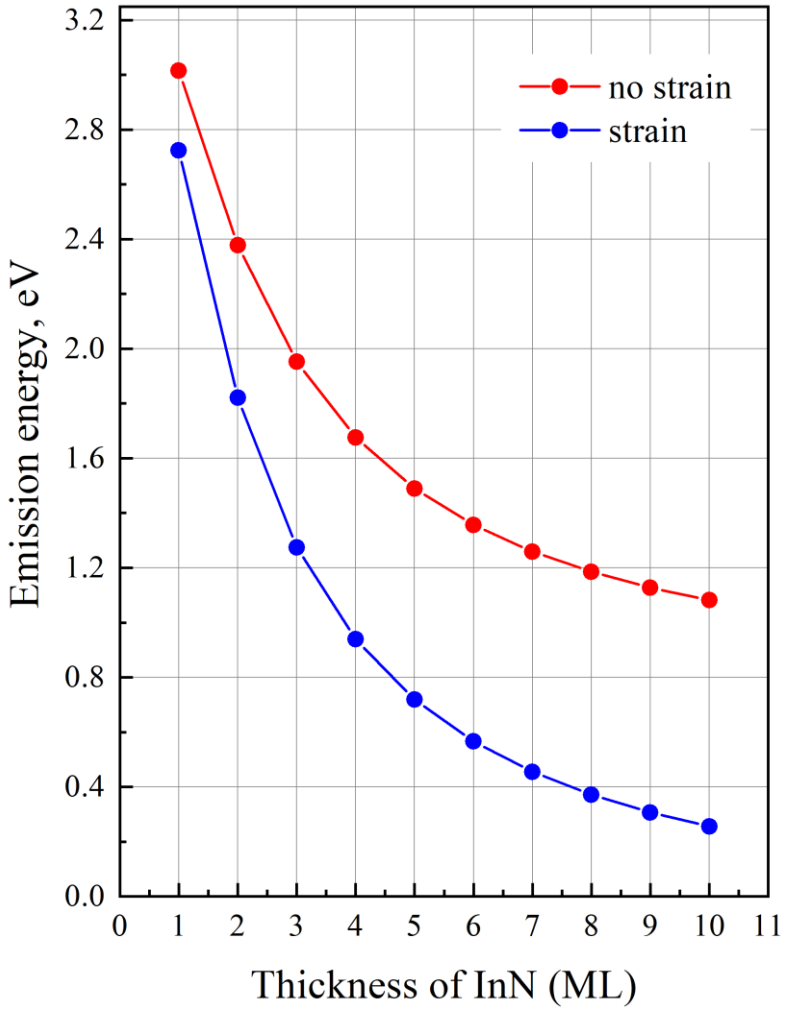

Figure 6.3. The calculated emission energy (effective bandgap) of the InN/GaN QW with varying thickness. Two effective bandgap curves were plotted assuming fully strained layer (blue curve) and fully relaxed layer (red curve).

peaks depends on the crystalline quality of the bulk GaN. The ultraviolet luminescence (UVL) band can be observed near to the NBE peak. The typical UVL emission can be observed in the range from 3.1 to 3.3 eV. Additionally, the ULV band is the set of a few peaks: the most intensive peak observed at 3.3 eV and LO phonon replicas with lower intensity are equidistantly red-shifted from it. The dislocation related blue luminescence (BL) and green luminescence (GL) bands are both quite broad and can be observed at 2.9 and 2.4 eV, respectively.

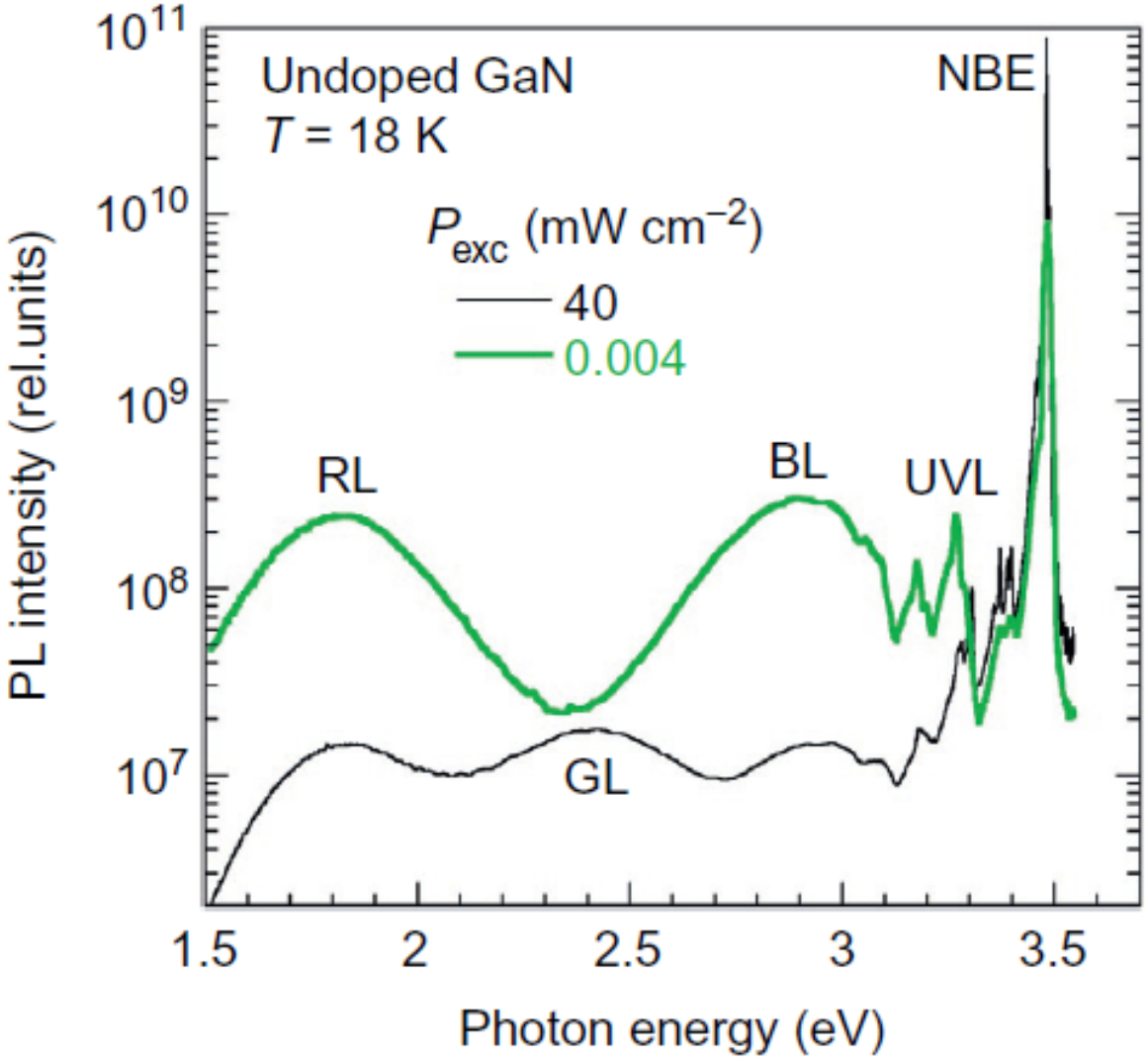

Figure 6.4. The low temperature PL spectra recorded for undoped GaN.[71]

The intensity ratio as well as the energy position of each band can be slightly different for the different growths. Therefore, it is essential to provide the PL data for samples grown in the same MBE system. For this purpose, the buffer layer of GaN was grown on a GaN/Sapphire substrate. The actual intensity dependent PL spectra for the reference GaN sample were measured on PLS2 system. The resulting PL data for the buffer layer of GaN with thickness of 200 nm grown on the unintentionally doped GaN/Sapphire substrate is shown in Fig. 6.5.

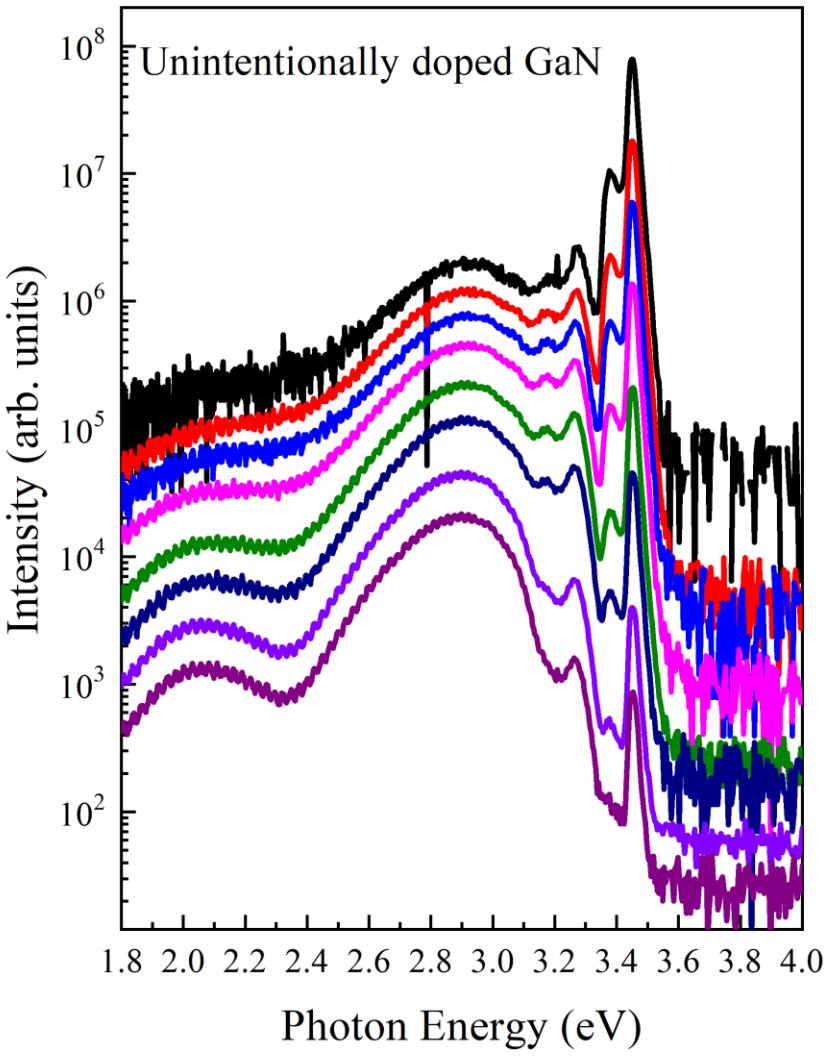

Figure 6.5. The intensity dependent PL spectra for 200 nm thick GaN buffer layer grown on an unintentionally doped GaN/Sapphire substrate.

6.3 Optical properties of InN/GaN QWs grown at different temperatures

The first part of the study relates to understanding the optical properties of the set of In(Ga)N/GaN QWs grown at different temperatures. In order to achieve this goal, the set of samples were investigated. The common elements of the structure of every sample can be found in Chapter 3. The only parameter that changed during the growth was the temperature of the substrate. The samples and their substrate temperatures are shown in Table 6.1. The reference

samples (name contains REF) were chosen to be the reference of GaN layer. Instead of In(Ga)N quantum well, the growth interruption was introduced.

Table 6.1. The key growth parameters for the InN/GaN MQW samples used for the optical measurements.

Sample #	Quantum well thickness	Substrate temperature, °C
N1	1ML	500
N2	1ML	530
N3	1ML	550
N4	1ML	575
REF500	0ML	500
REF530	0ML	530
REF550	0ML	550
REF575	0ML	575

The intensity dependent PL data were taken for each of the samples. The resulting normalized PL spectra can be observed in Fig. 6.5. For comparison, the PL emission from sample REF550 is also included in the figure in order to show GaN bandgap related emission at 3.47 eV as well as corresponding defect bands emission at 2.6 and 3.2 eV. In addition, the position of the PL peak depending on substrate temperature is plotted in Fig. 6.6. The horizontal red dashed line underlines the energy position of pure GaN bandgap emission. The significant red shift around 700 meV was observed by decreasing the substrate temperature from 575 °C to 500 °C during growth. It is reasonable to assume that the red shift could be caused by changing the indium content in the In(Ga)N quantum well.

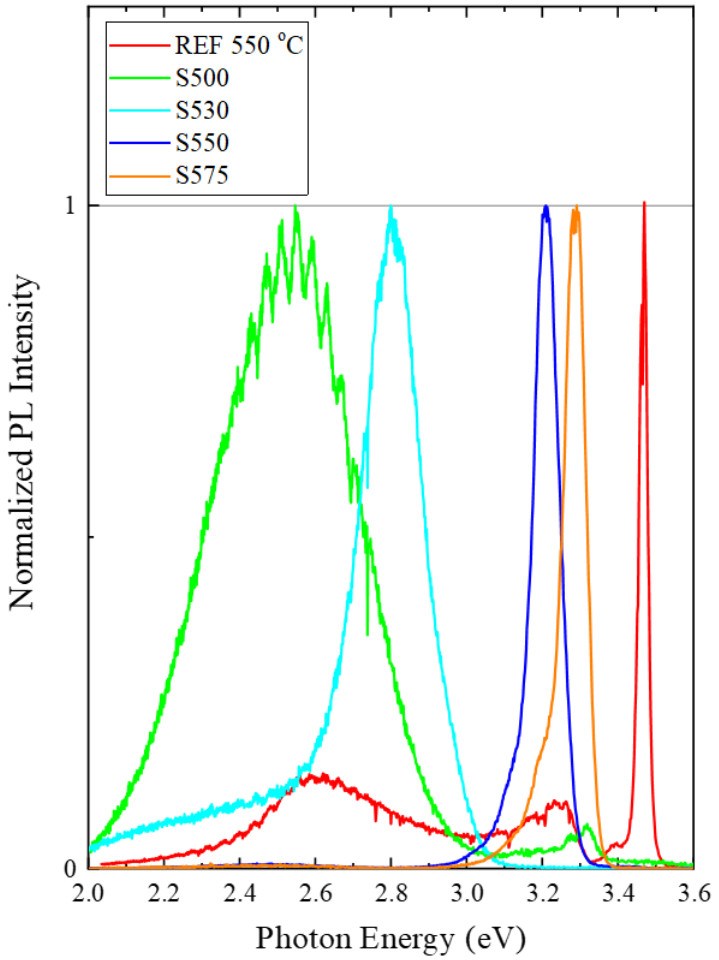

Figure 6.5. Normalized low temperature experimental (10 K) PL results measured for InN/GaN MQWs structures with varied growth temperature.

The conclusion about the indium content changing is based on TEM imaging, which clearly indicates that only one monolayer of In(Ga)N was deposited. For instance, the TEM image for the sample N3 is shown in Fig. 6.7. The image was taken in under-focused mode to underline the single InN/GaN QW. However, the same discussion as for the InAs/GaAs QW TEM imaging can be applied in this case. The presented TEM image basically shows that the vertical lattice parameter is slightly different in the 1 ML thick region, which is presumed to coincide with the InN/GaN QW. The information about the indium redistribution, however,

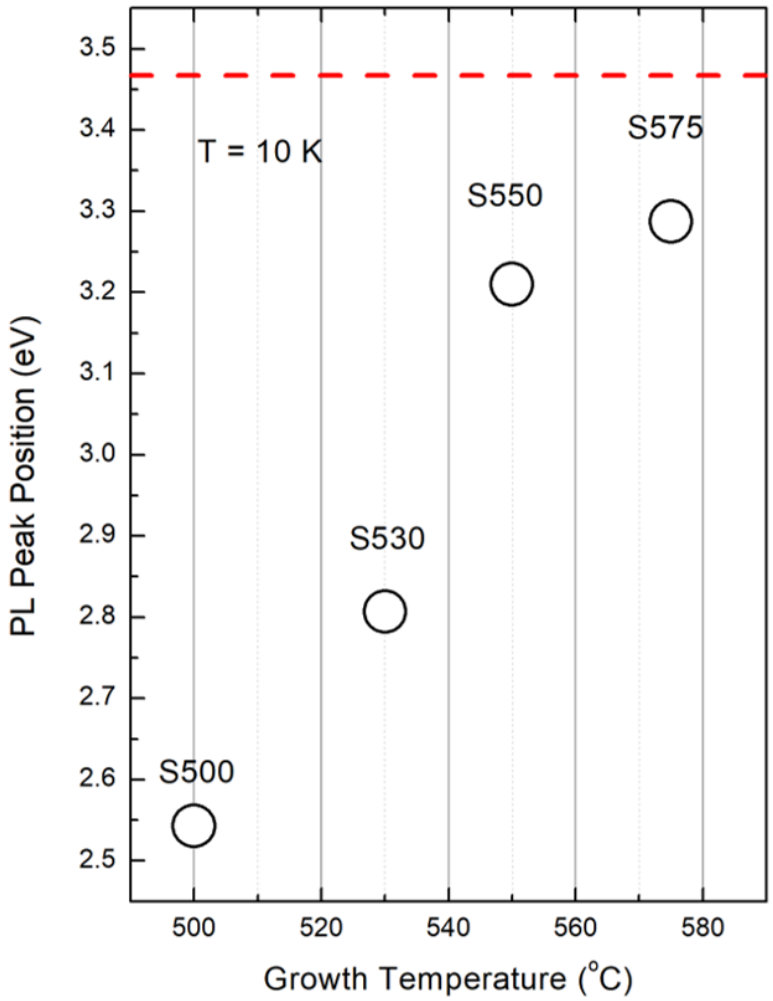

Figure 6.6. PL peak emission energy as a function of InN/GaN MQW growth temperature.

cannot be directly determined given only TEM data. The STEM analysis which is sensitive to the atomic weight would be sufficient to determine the exact composition of the QW. Unlike the InAs/GaAs QW samples, good quality STEM images taken for ultrathin InN/GaN QW requires professional sample preparation techniques.

The high-resolution XRD analysis was utilized to estimate the total indium content with sufficient accuracy. The estimated indium content as a function of the growth temperature is shown in Fig. 6.8. This dependence can be associated with the thermally activated exchange

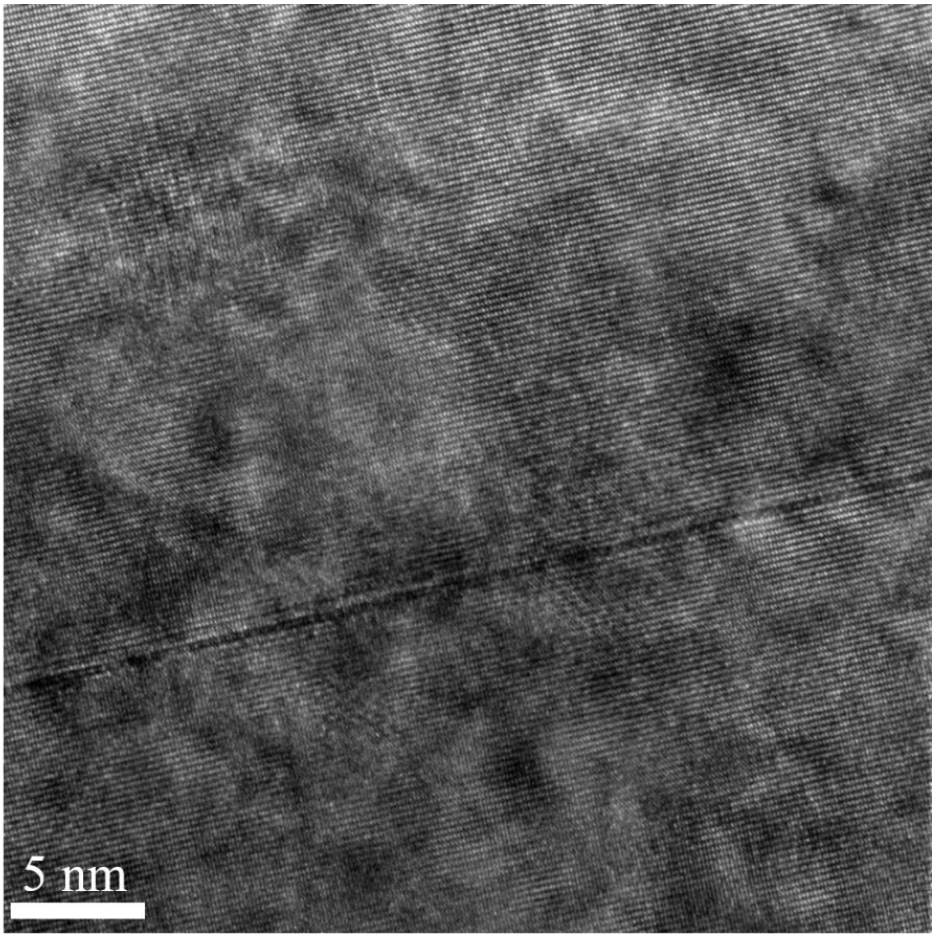

Figure 6.7. Cross-sectional TEM image of nominal 1 ML of InN QW embedded into the GaN buffer.

mechanism during the growth of the quantum well. With such exchange mechanism, the number of indium atoms that are being replaced by gallium atoms will grow with increasing temperature. The same dependence can be plotted for $1/kT$ in semi-log scale. This type of plotting reveals a linear dependence suggesting that the indium content follows the Arrhenius equation of the form:

$$x_{In} = x_0 \exp(\frac{E_a}{kT}), \qquad \text{(Equation 6.1)}$$

from which the activation energy is calculated to be equal to 0.7 eV. As was shown for the InAs/GaAs QW samples, the total indium content parameter is not sufficient to determine the

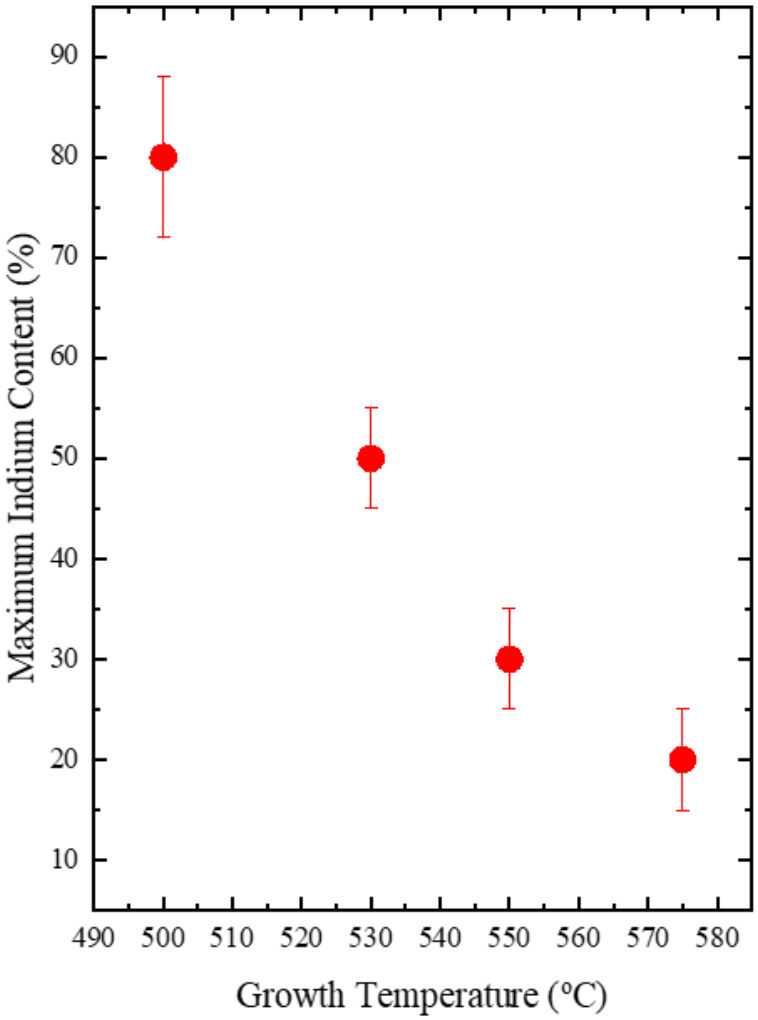

Figure 6.8. The total content of indium within the InN/GaN QW extracted from the XRD analysis.

effective band gap of the structure. Another important factor is the content profile shape. The segregation model proposed earlier has not found strong support among the research community.

Therefore, the general indium content profile is the open question. A few research groups claimed that all indium is located within the nominal QW thickness (no segregation through InN/GaN interface).[34], [56] The other groups, based on the careful STEM analysis, show that the indium content profile of the 1 ML InN/GaN has a triangular shape.[66], [67] It

was shown that the indium evenly distributed in both directions up to two MLs. The resulting indium profile consisting of a total five MLs is plotted in Fig. 6.9.

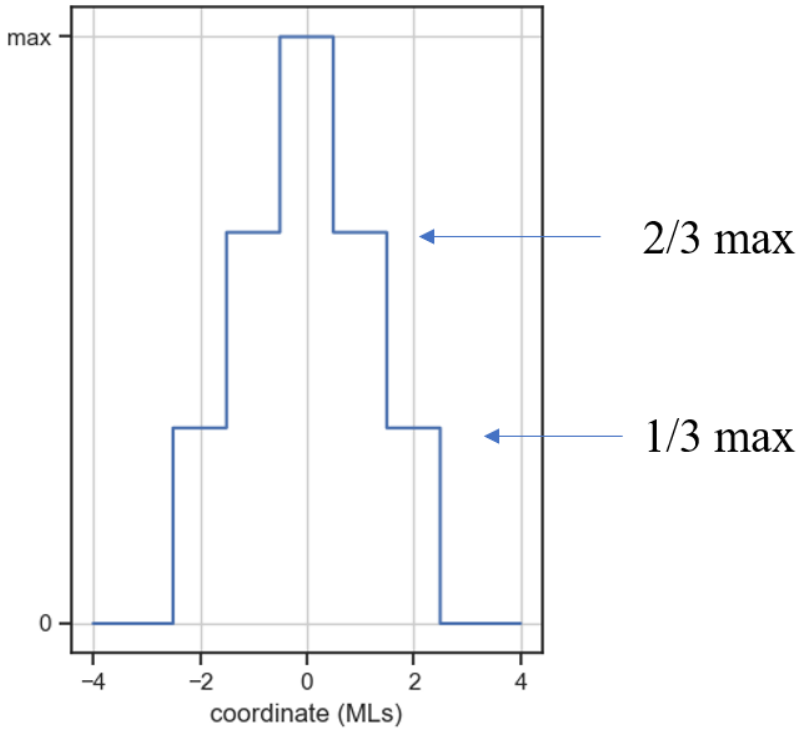

Figure 6.9. The assumed indium content profile used for the simulation purposes.

As a result, the only parameter that can be manipulated is the indium content at the maximum. The resulting profile was used in the effective bandgap simulations in order to achieve the best fit with the experimental PL peak position data shown earlier. The calculations were performed on the continuous set of indium profiles resulting in the effective bandgap dependence shown in Fig. 6.10. The inset represents the energy band diagram of the triangular shaped indium content in the case of 30% indium in the center layer. The Schrodinger equation was solved for each of the diagrams. For instance, the ground state levels for the conduction and valence bands for the 30% of indium within the central layer are marked as red lines in the inset.

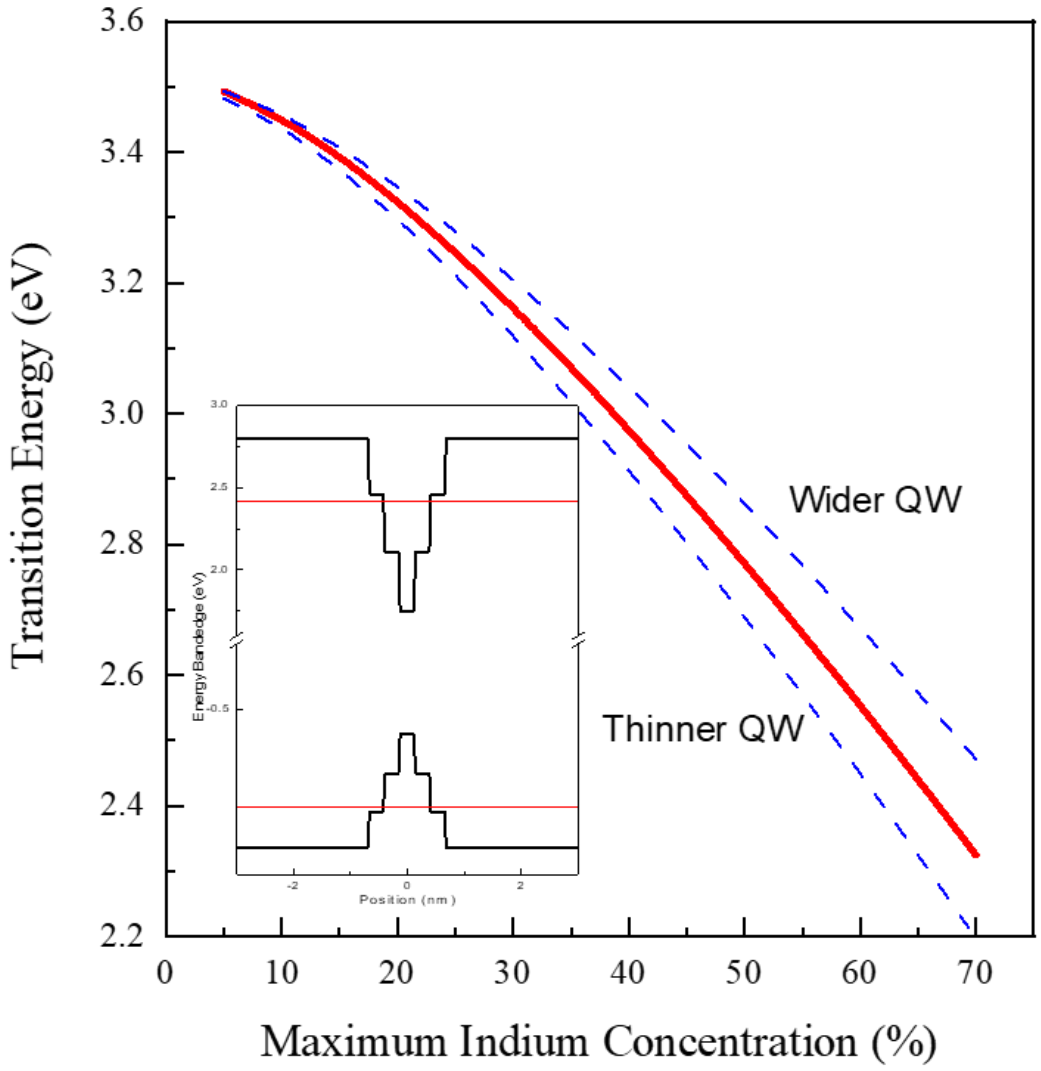

Figure 6.10. The effective bandgap simulation of the triangular InN/GaN QW as a function of the content of indium at the maximum.

The energy difference between those lines exactly represents the calculated effective bandgap, which can be directly compared with the experimental PL peak positions.

Overall, by comparing the indium content dependence obtained from XRD analysis and numerical effective bandgap calculation, good agreement between experimental data and simulation was found. However, it was assumed that the lattice parameter changing due to the lattice mismatch between InGaN and GaN only affected the center layer with the highest indium

content. Additionally, the dashed blue curves show the effect of changing the full width of the QW while keeping the total amount of indium the same within the vertical axis.

While designing the LED structures, one of the most important characteristics was the PL efficiency. Experimentally, the PL efficiency is proportional to the area under the corresponding PL curve. The resulting PL efficiency as a function of the growth temperature at a fixed excitation intensity for all four InN/GaN MQW samples is shown in Fig. 6.11. As can be determined from the figure, the optimal growth temperature in terms of PL efficiency was within the range from 550 to 575 °C.

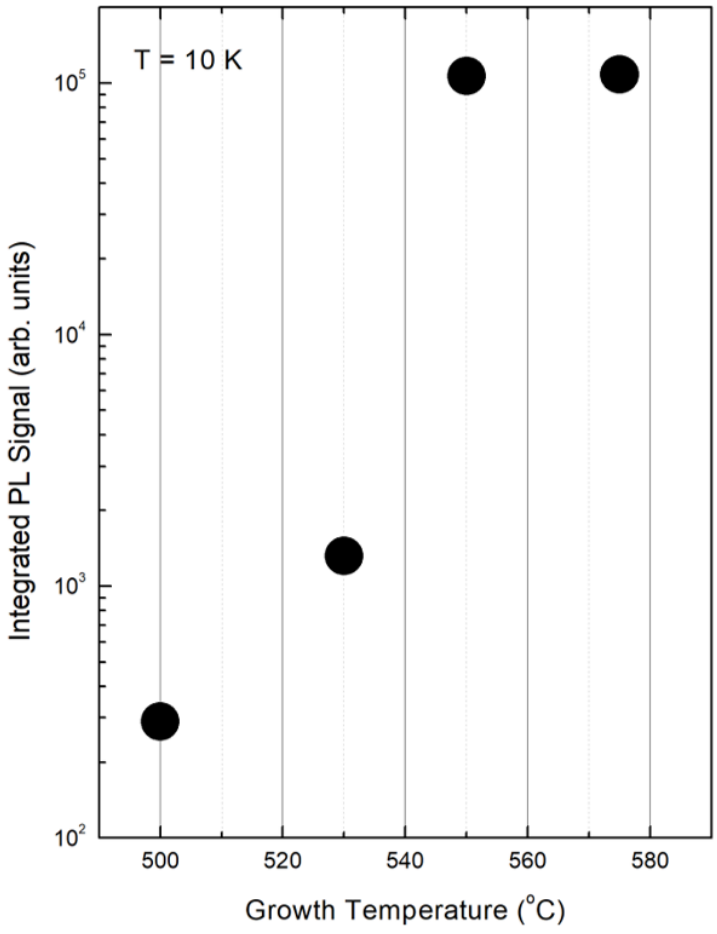

Figure 6.11. The PL efficiency (integrated PL) for InN/GaN MQW structures plotted as a function of the growth temperature.

The efficiency increase was connected with the crystalline quality improvement of the GaN barrier. Even though the lower growth temperatures were preferable to obtain good quality InN, the barriers still play a major role in the optical efficiency due to the low quality of the GaN grown at these temperatures. The huge impact of the barrier on the optical efficiency can be explained by the wave functions of the electrons and holes that are mainly localized in the barrier due to the extremely narrow QW. As a result, the generated electron-hole pairs will have a low probability of being captured by the QW. Instead, a majority of carriers will be trapped by the dislocation formed energy levels within the low temperature grown GaN. The trapped carriers will recombine through non-radiative channels. At higher growth temperatures, the density of defect related energy traps decreases followed by an increase of overall GaN quality. Effectively, this leads to the optical efficiency behavior for the growth temperatures from 500 to 575 °C.

6.4 Summary

The set of samples with varying parameters were grown using plasma-assisted molecular beam epitaxy (PAMBE) system on semi-insulating GaN (0001) substrates. The nominal In(Ga)N QW thickness was chosen to be one ML for four samples grown at different temperatures. The intensity dependent PL data were taken for each of the sample. A significant red shift of 700 meV by changing substrate temperature from 575 °C to 500 °C was observed. By performing the effective bandgap simulation, it was concluded that this transition energy shift was caused by the total amount of indium change within the In(Ga)N quantum wells. An indium content depth profile shape analysis was performed to demonstrate its weak effect of the transition energy. Furthermore, the structural properties were studied by the XRD technique and

TEM analysis where the total indium content change was confirmed. Finally, the correlation between optical and structural properties and the actual indium content profile were discussed.

Chapter 7: Conclusion and Outlook

In this dissertation, structural parameters of ultrathin QWs and their effect on emission properties were investigated by conducting a systematic analysis of the optical properties of In(Ga)As/GaAs and In(Ga)N/GaN ultrathin QWs. Specifically, the analysis involved photoluminescence measurements combined with effective bandgap simulation, x-ray diffraction, and transmission electron microscopy characterization. It was discovered that the indium content depth profile modifications due to the In/Ga intermixing could be achieved by controlling the growth temperature for the In(Ga)As/GaAs QWs. This led to substantial changes in the emission properties. The analysis was supported by the effective bandgap simulation, which allowed not only to probe the exact shape of the indium depth profile but also to predict and design structures with the desired optical characteristics. In the case of In(Ga)N/GaN ultrathin QWs, the growth temperature change affected the total indium incorporation within the QW, which was supported by the optical analysis and XRD characterization. The effective bandgap analysis revealed that the total amount of indium was the dominant factor when dealing with optical emission from ultrathin QWs. This was proven by simulating the transition energy of ultrathin In(Ga)N/GaN QWs with varied total amount of indium as well as the indium content profile shape variation.

References

[1] S. F. Tang, S. Y. Lin, and S. C. Lee, “Near-room-temperature operation of an InAs/GaAs quantum-dot infrared photodetector,” *Appl. Phys. Lett.*, vol. 78, no. 17, pp. 2428–2430, 2001.

[2] X. Dai, S. Zhang, Z. Wang, G. Adamo, H. Liu, Y. Huang, C. Couteau, and C. Soci, “GaAs/AlGaAs nanowire photodetector,” *Nano Lett.*, vol. 14, no. 5, pp. 2688–2693, 2014.

[3] T. Nishida, H. Saito, and N. Kobayashi, “Efficient and high-power AlGaN-based ultraviolet light-emitting diode grown on bulk GaN,” *Appl. Phys. Lett.*, vol. 79, no. 6, pp. 711–712, 2001.

[4] H. W. Lin, Y. J. Lu, H. Y. Chen, H. M. Lee, and S. Gwo, “InGaN/GaN nanorod array white light-emitting diode,” *Appl. Phys. Lett.*, vol. 97, no. 7, p. 073101, 2010.

[5] C. Huh, K. S. Lee, E. J. Kang, and S. J. Park, “Improved light-output and electrical performance of InGaN-based light-emitting diode by microroughening of the p-GaN surface,” *J. Appl. Phys.*, vol. 93, no. 11, pp. 9383–9385, 2003.

[6] P. Harrison, D. Indjin, V. D. Jovanović, A. Mirčetić, Z. Ikonić, R. W. Kelsall, J. McTavish, I. Savić, N. Vukmirović, and V. Milanović, “A physical model of quantum cascade lasers: Application to GaAs, GaN and SiGe devices,” *Phys. Status Solidi Appl. Mater. Sci.*, vol. 202, no. 6, pp. 980–986, 2005.

[7] J. Cheng, P. Quach, D. Wang, F. Liu, S. Liu, L. Yang, H. Liu, B. Shen, Y. Tong, and X. Wang, “Dominant Influence of Interface Roughness Scattering on the Performance of GaN Terahertz Quantum Cascade Lasers,” *Nanoscale Res. Lett.*, vol. 14, p. 206, 2019.

[8] A. T. Meney and E. P. O’Reilly, “Theory of optical gain in ideal GaN heterostructure lasers,” *Appl. Phys. Lett.*, vol. 67, p. 3013, 1995.

[9] A. T. Meney, E. P. O’Reilly, and A. R. Adams, “Optical gain in wide bandgap GaN quantum well lasers,” *Semicond. Sci. Technol.*, vol. 11, no. 6, pp. 897–903, 1996.

[10] W. Muranaga, T. Akagi, R. Fuwa, S. Yoshida, J. Ogimoto, Y. Akatsuka, S. Iwayama, T. Takeuchi, S. Kamiyama, M. Iwaya, and I. Akasaki, “GaN-based vertical-cavity surface-emitting lasers using n-type conductive AlInN/GaN bottom distributed Bragg reflectors with graded interfaces,” *Jpn. J. Appl. Phys.*, vol. 58, p. SCCC01, 2019.

[11] S. Jin, L. Xu, and Y. Li, “Inside a Mixed QW Modulator,” vol. 28, no. 16, pp. 1759–1762, 2016.

[12] H. F. Zhu, L. H. Du, J. Li, Q. W. Shi, B. Peng, Z. R. Li, W. X. Huang, and L. G. Zhu, “Near-perfect terahertz wave amplitude modulation enabled by impedance matching in VO2 thin films,” *Appl. Phys. Lett.*, vol. 112, no. 8, p. 081103, 2018.

[13] D. Zhang, W. Lou, M. Miao, S. C. Zhang, and K. Chang, “Interface-induced topological

insulator transition in GaAs/Ge/GaAs quantum wells," *Phys. Rev. Lett.*, vol. 111, no. 15, p. 156402, 2013.

[14] G. Hu, Y. Zhang, L. Li, and Z. L. Wang, "Piezotronic Transistor Based on Topological Insulators," *ACS Nano*, vol. 12, no. 1, pp. 779–785, 2018.

[15] P. Y. Shapochkin, M. S. Lozhkin, I. A. Solovev, O. A. Lozhkina, Y. P. Efimov, S. A. Eliseev, V. A. Lovcjus, G. G. Kozlov, A. A. Pervishko, D. N. Krizhanovskii, P. M. Walker, I. A. Shelykh, M. S. Skolnick, and Y. V. Kapitonov, "Polarization-resolved strong light – matter coupling in planar GaAs / AlGaAs waveguides," *Opt. Lett.*, vol. 43, no. 18, pp. 4526–4529, 2018.

[16] H. T. Grahn, C. Chèze, R. Calarco, T. Flissikowski, F. Feix, and O. Brandt, "Individual electron and hole localization in submonolayer InN quantum sheets embedded in GaN," *Appl. Phys. Lett.*, vol. 109, no. 4, p. 042104, 2016.

[17] A. Aiello, Y. Wu, Z. Mi, and P. Bhattacharya, "Deep ultraviolet monolayer GaN/AlN disk-in-nanowire array photodiode on silicon," *Appl. Phys. Lett.*, vol. 116, no. 6, p. 061104, 2020.

[18] V. N. Jmerik, D. V. Nechaev, A. A. Toropov, E. A. Evropeitsev, V. I. Kozlovsky, V. P. Martovitsky, S. Rouvimov, and S. V. Ivanov, "High-efficiency electron-beam-pumped sub-240-nm ultraviolet emitters based on ultra-thin GaN/AlN multiple quantum wells grown by plasma-assisted molecular-beam epitaxy on c-Al2O3," *Appl. Phys. Express*, vol. 11, no. 9, p. 091003, 2018.

[19] W. Sun, C. K. Tan, and N. Tansu, "III-Nitride Digital Alloy: Electronics and Optoelectronics Properties of the InN/GaN Ultra-Short Period Superlattice Nanostructures," *Sci. Rep.*, vol. 7, no. 1, p. 6671, 2017.

[20] R. S. R. Gajjela, A. L. Hendriks, A. Alzeidan, T. F. Cantalice, A. A. Quivy, and P. M. Koenraad, "Cross-sectional scanning tunneling microscopy of InAs / GaAs (001) submonolayer quantum dots," *Phys. Rev. Mater.*, vol. 4, no. 11, p. 114601, 2020.

[21] X. Sun, P. Wang, T. Wang, L. Chen, Z. Chen, K. Gao, T. Aoki, M. Li, J. Zhang, T. Schulz, M. Albrecht, W. Ge, Y. Arakawa, B. Shen, M. Holmes, and X. Wang, "Single-photon emission from isolated monolayer islands of InGaN," *Light Sci. Appl.*, vol. 9, no. 1, p. 159, 2020.

[22] L. Lymperakis, T. Schulz, C. Freysoldt, M. Anikeeva, Z. Chen, X. Zheng, B. Shen, C. Chèze, M. Siekacz, X. Q. Wang, M. Albrecht, and J. Neugebauer, "Elastically frustrated rehybridization: Origin of chemical order and compositional limits in InGaN quantum wells," *Phys. Rev. Mater.*, vol. 2, no. 1, p. 011601(R), 2018.

[23] M. Anikeeva, M. Albrecht, F. Mahler, J. W. Tomm, L. Lymperakis, C. Chèze, R. Calarco, J. Neugebauer, and T. Schulz, "Role of hole confinement in the recombination properties of InGaN quantum structures," *Sci. Rep.*, vol. 9, no. 1, p. 9047, 2019.

[24] F. Hopfer, A. Mutig, M. Kuntz, G. Fiol, D. Bimberg, N. N. Ledentsov, V. A. Shchukin, S. S. Mikhrin, D. L. Livshits, I. L. Krestnikov, A. R. Kovsh, N. D. Zakharov, and P. Werner, "Single-mode submonolayer quantum-dot vertical-cavity surface-emitting lasers with high modulation bandwidth," *Appl. Phys. Lett.*, vol. 89, no. 14, p. 141106, 2006.

[25] P. Lam, J. Wu, M. Tang, Q. Jiang, S. Hatch, R. Beanland, J. Wilson, R. Allison, and H. Liu, "Submonolayer InGaAs/GaAs quantum dot solar cells," *Sol. Energy Mater. Sol. Cells*, vol. 126, pp. 83–87, 2014.

[26] D. Z. Y. Ting, S. V. Bandara, S. D. Gunapala, J. M. Mumolo, S. A. Keo, C. J. Hill, J. K. Liu, E. R. Blazejewski, S. B. Rafol, and Y. C. Chang, "Submonolayer quantum dot infrared photodetector," *Appl. Phys. Lett.*, vol. 94, no. 11, p. 111107, 2009.

[27] J. Huang, D. Guo, W. Chen, Z. Deng, Y. Bai, T. Wu, Y. Chen, H. Liu, J. Wu, and B. Chen, "Sub-monolayer quantum dot quantum cascade mid-infrared photodetector," *Appl. Phys. Lett.*, vol. 111, no. 251104, p. 251104, 2017.

[28] S. Harrison, M. P. Young, P. D. Hodgson, R. J. Young, M. Hayne, L. Danos, A. Schliwa, A. Strittmatter, A. Lenz, H. Eisele, U. W. Pohl, and D. Bimberg, "Heterodimensional charge-carrier confinement in stacked submonolayer InAs in GaAs," *Phys. Rev. B*, vol. 93, no. 8, pp. 1–9, 2016.

[29] C. Chèze, F. Feix, M. Anikeeva, T. Schulz, M. Albrecht, H. Riechert, O. Brandt, and R. Calarco, "In/GaN(0001)- (3×3)R30° adsorbate structure as a template for embedded (In, Ga)N/GaN monolayers and short-period superlattices," *Appl. Phys. Lett.*, vol. 110, no. 7, p. 072104, 2017.

[30] C. Chèze, M. Siekacz, F. Isa, B. Jenichen, F. Feix, J. Buller, T. Schulz, M. Albrecht, C. Skierbiszewski, R. Calarco, and H. Riechert, "Investigation of interface abruptness and in content in (In,Ga)N/GaN superlattices," *J. Appl. Phys.*, vol. 120, no. 12, p. 125307, 2016.

[31] R. Kumar, Y. Maidaniuk, A. Kuchuk, S. K. Saha, P. K. Ghosh, Y. I. Mazur, M. E. Ware, and G. J. Salamo, "Excitation intensity and thickness dependent emission mechanism from an ultrathin InAs layer in GaAs matrix," *J. Appl. Phys.*, vol. 124, no. 23, p. 235303, 2018.

[32] C. Li, Y. Maidaniuk, A. V. Kuchuk, Y. I. Mazur, M. Benamara, M. E. Ware, and G. J. Salamo, "Effect of indium accumulation on the growth and properties of ultrathin In(Ga)N/GaN quantum wells," *Mater. Des.*, vol. 190, p. 108565, 2020.

[33] C. Li, Y. Maidaniuk, A. V. Kuchuk, S. Shetty, P. Ghosh, T. P. White, T. Al Morgan, X. Hu, Y. Wu, M. E. Ware, Y. I. Mazur, and G. J. Salamo, "Kinetically controlled indium surface coverage effects on PAMBE-growth of InN/GaN(0001) quantum well structures," *J. Appl. Phys.*, vol. 123, no. 19, p. 195302, 2018.

[34] T. Schulz, L. Lymperakis, M. Anikeeva, M. Siekacz, P. Wolny, T. Markurt, and M. Albrecht, "Influence of strain on the indium incorporation in (0001) GaN," *Phys. Rev. Mater.*, vol. 4, no. 7, p. 073404, 2020.

[35] D. Bimberg, N. Kirstaedter, N. N. Ledentsov, Z. I. Alferov, P. S. Kop, and V. M. Ustinov, "InGaAs – GaAs Quantum-Dot Lasers," *IEEE J. Sel. Top. Quantum Electron*, vol. 3, no. 2, pp. 196–205, 1997.

[36] T. Sugaya, O. Numakami, R. Oshima, S. Furue, H. Komaki, T. Amano, K. Matsubara, Y. Okano, and S. Niki, "Ultra-high stacks of InGaAs/GaAs quantum dots for high efficiency solar cells," *Energy Environ. Sci.*, vol. 5, no. 3, pp. 6233–6237, 2012.

[37] J. Ajayan and D. Nirmal, "20-nm enhancement-mode metamorphic GaAs HEMT with highly doped InGaAs source/drain regions for high-frequency applications," *Int. J. Electron.*, vol. 104, no. 3, pp. 504–512, 2017.

[38] A. Lenz, H. Eisele, J. Becker, J.-H. Schulze, T. D. Germann, F. Luckert, K. Pötschke, E. Lenz, L. Ivanova, A. Strittmatter, D. Bimberg, U. W. Pohl, and M. Dähne, "Atomic structure and optical properties of InAs submonolayer depositions in GaAs," *J. Vac. Sci. Technol. B, Nanotechnol. Microelectron. Mater. Process. Meas. Phenom.*, vol. 29, no. 4, p. 04D104, 2011.

[39] M. I. Alonso, M. Ilg, and K. H. Ploog, "Optical investigation of the electronic structure of single ultrathin InAs layers grown pseudomorphically on (100) and (311)A GaAs substrates," *Phys. Rev. B*, vol. 50, no. 3, pp. 1628–1635, 1994.

[40] M. I. Alonso, M. Ilg, K. Ploog, and A. Trampert, "Excitonic properties of isolated nanometer-sized InAs islands in a GaAs matrix," *J. Appl. Phys.*, vol. 78, no. 3, pp. 1980–1983, 1995.

[41] Z. L. Yuan, Z. Y. Xu, B. Z. Zheng, J. Z. Xu, S. S. Li, W. Ge, Y. Wang, J. Wang, L. L. Chang, P. D. Wang, C. M. Sotomayor Torres, and N. N. Ledentsov, "Two-dimensional excitonic emission in InAs submonolayers," *Phys. Rev. B*, vol. 54, no. 23, pp. 16919–16924, 1996.

[42] D. González, V. Braza, A. D. Utrilla, A. Gonzalo, D. F. Reyes, T. Ben, A. Guzman, A. Hierro, and J. M. Ulloa, "Quantitative analysis of the interplay between InAs quantum dots and wetting layer during the GaAs capping process," *Nanotechnology*, vol. 28, no. 42, 2017.

[43] P. D. Robb, M. Finnie, and A. J. Craven, "Characterisation of InAs/GaAs short period superlattices using column ratio mapping in aberration-corrected scanning transmission electron microscopy," *Micron*, vol. 43, no. 10, pp. 1068–1072, 2012.

[44] S. Y. Karpov and Y. N. Makarov, "Indium segregation kinetics in InGaAs ternary compounds," *Thin Solid Films*, vol. 380, no. 1–2, pp. 71–74, 2000.

[45] K. Yamaguchi, T. Okada, and F. Hiwatashi, "Analysis of indium surface segregation in molecular beam epitaxy of InGaAs/GaAs quantum wells," *Appl. Surf. Sci.*, vol. 117/118, pp. 700–704, 1997.

[46] O. Dehaese, X. Wallart, and F. Mollot, "Kinetic model of element III segregation during

molecular beam epitaxy of III-III′-V semiconductor compounds," *Appl. Phys. Lett.*, vol. 66, p. 52, 1995.

[47] J. M. Moison, C. Guille, F. Houzay, F. Barthe, and M. Van Rompay, "Surface segregation of third-column atoms in group III-V arsenide compounds: Ternary alloys and heterostructures," *Phys. Rev. B*, vol. 40, no. 9, pp. 6149–6162, 1989.

[48] K. Muraki, S. Fukatsu, Y. Shiraki, and R. Ito, "Surface segregation of in atoms during molecular beam epitaxy and its influence on the energy levels in InGaAs/GaAs quantum wells," *Appl. Phys. Lett.*, vol. 61, no. 5, pp. 557–559, 1992.

[49] M. Ilg, M. I. Alonso, A. Lehmann, K. H. Ploog, and M. Hohenstein, "Investigation of InAs submonolayer and monolayer structures on GaAs(100) and (311) substrates," *J. Appl. Phys.*, vol. 74, no. 12, pp. 7188–7197, 1993.

[50] R. R. Pelá, L. K. Teles, M. Marques, and S. Martini, "Theoretical study of the indium incorporation into III-V compounds revisited: The role of indium segregation and desorption," *J. Appl. Phys.*, vol. 113, no. 3, p. 033515, 2013.

[51] S. Martini, J. E. Manzoli, and A. A. Quivy, "Study of the influence of indium segregation on the optical properties of InGaAs/GaAs quantum wells via split-operator method," *J. Vac. Sci. Technol. B*, vol. 28, no. 2, pp. 277–283, 2010.

[52] N. Tit, "Two types of quantum-confinement characters for the bound states in the InGaN/GaN quantum wells," *Phys. E*, vol. 44, pp. 298–306, 2011.

[53] M. Auf Der Maur, A. Pecchia, G. Penazzi, W. Rodrigues, and A. Di Carlo, "Efficiency Drop in Green InGaN/GaN Light Emitting Diodes: The Role of Random Alloy Fluctuations," *Phys. Rev. Lett.*, vol. 116, no. 2, p. 027401, 2016.

[54] S. Che, A. Yuki, H. Watanabe, Y. Ishitani, and A. Yoshikawa, "Fabrication of asymmetric GaN/InN/InGaN/GaN quantum-well light emitting diodes for reducing the quantum-confined stark effect in the blue-green region," *Appl. Phys. Express*, vol. 2, no. 2, 2009.

[55] S. M. Islam, K. Lee, J. Verma, V. Protasenko, S. Rouvimov, S. Bharadwaj, H. Xing, and D. Jena, "MBE-grown 232-270 nm deep-UV LEDs using monolayer thin binary GaN/AlN quantum heterostructures," *Appl. Phys. Lett.*, vol. 110, no. 4, 2017.

[56] A. Yoshikawa, S. B. Che, W. Yamaguchi, H. Saito, X. Q. Wang, Y. Ishitani, and E. S. Hwang, "Proposal and achievement of novel structure InNGaN multiple quantum wells consisting of 1 ML and fractional monolayer InN wells inserted in GaN matrix," *Appl. Phys. Lett.*, vol. 90, no. 7, p. 073101, 2007.

[57] A. Yoshikawa, S. B. Che, N. Hashimoto, H. Saito, Y. Ishitani, and X. Q. Wang, "Fabrication and characterization of novel monolayer InN quantum wells in a GaN matrix," *J. Vac. Sci. Technol. B*, vol. 26, no. 4, pp. 1551–1559, 2008.

[58] A. Yoshikawa, S. Che, Y. Ishitani, and X. Wang, "Advances in InN epitaxy and its

material control by MBE towards novel InN-based QWs," *J. Cryst. Growth*, vol. 311, no. 7, pp. 2073–2079, 2009.

[59] A. Yoshikawa, K. Kusakabe, N. Hashimoto, D. Imai, and E. S. Hwang, "Systematic study on dynamic atomic layer epitaxy of InN on/in +c-GaN matrix and fabrication of fine-structure InN/GaN quantum wells: Impact of excess In-atoms at high growth temperature," *J. Appl. Phys.*, vol. 120, no. 23, 2016.

[60] S. M. Ko, H. S. Kwack, C. Park, Y. S. Yoo, S. Y. Kwon, H. Jin Kim, E. Yoon, L. Si Dang, and Y. H. Cho, "Strong carrier localization and diminished quantum-confined Stark effect in ultra-thin high-indium-content InGaN quantum wells with violet light emission," *Appl. Phys. Lett.*, vol. 103, no. 22, 2013.

[61] K. Tateishi, M. Funato, Y. Kawakami, K. Okamoto, and K. Tamada, "Highly enhanced green emission from InGaN quantum wells due to surface plasmon resonance on aluminum films," *Appl. Phys. Lett.*, vol. 106, no. 12, pp. 1–6, 2015.

[62] H. V. Stanchu, A. V. Kuchuk, M. Barchuk, Y. I. Mazur, V. P. Kladko, Z. M. Wang, D. Rafaja, and G. J. Salamo, "Asymmetrical reciprocal space mapping using X-ray diffraction: A technique for structural characterization of GaN/AlN superlattices," *CrystEngComm*, vol. 19, no. 22, pp. 2977–2982, 2017.

[63] H. V. Stanchu, A. V. Kuchuk, P. M. Lytvyn, Y. I. Mazur, Y. Maidaniuk, M. Benamara, S. Li, S. Kryvyi, V. P. Kladko, A. E. Belyaev, Z. M. Wang, and G. J. Salamo, "Strain relaxation in GaN/AlN superlattices on GaN(0001) substrate: Combined superlattice-to-substrate lattice misfit and thickness-dependent effects," *Mater. Des.*, vol. 157, no. 0001, pp. 141–150, 2018.

[64] W. Pan, E. Dimakis, G. T. Wang, T. D. Moustakas, and D. C. Tsui, "Two-dimensional electron gas in monolayer InN quantum wells," *Appl. Phys. Lett.*, vol. 105, no. 21, 2014.

[65] D. Ma, X. Rong, X. Zheng, W. Wang, P. Wang, T. Schulz, M. Albrecht, S. Metzner, M. Müller, O. August, F. Bertram, J. Christen, P. Jin, M. Li, J. Zhang, X. Yang, F. Xu, Z. Qin, W. Ge, B. Shen, and X. Wang, "Exciton emission of quasi-2D InGaN in GaN matrix grown by molecular beam epitaxy," *Sci. Rep.*, vol. 7, no. 46420, pp. 1–6, 2017.

[66] G. Staszczak, I. Gorczyca, E. Grzanka, J. Smalc-Koziorowska, G. Targowski, R. Czernecki, M. Siekacz, S. Grzanka, C. Skierbiszewski, T. Schulz, N. E. Christensen, and T. Suski, "Bandgap behavior of InGaN/GaN short period superlattices grown by metal-organic vapor phase epitaxy," *Phys. Status Solidi Basic Res.*, vol. 254, no. 8, 2017.

[67] G. P. Dimitrakopulos, I. G. Vasileiadis, C. Bazioti, J. Smalc-Koziorowska, S. Kret, E. Dimakis, N. Florini, T. Kehagias, T. Suski, T. Karakostas, T. D. Moustakas, and P. Komninou, "Compositional and strain analysis of In(Ga)N/GaN short period superlattices," *J. Appl. Phys.*, vol. 123, no. 2, p. 024304, 2018.

[68] T. Suski, T. Schulz, M. Albrecht, X. Q. Wang, I. Gorczyca, K. Skrobas, N. E. Christensen, and A. Svane, "The discrepancies between theory and experiment in the optical emission

of monolayer In(Ga)N quantum wells revisited by transmission electron microscopy," *Appl. Phys. Lett.*, vol. 104, no. 18, p. 182103, 2014.

[69] I. Gorczyca, T. Suski, N. E. Christensen, and A. Svane, "Theoretical study of nitride short period superlattices," *J. Phys. Condens. Matter*, vol. 30, no. 6, p. 063001, 2018.

[70] I. Vurgaftman and J. R. Meyer, "Band parameters for III–V compound semiconductors and their alloys," *J. Appl. Phys.*, vol. 89, no. 11, p. 5815, 2001.

[71] M. A. Reshchikov and H. Morkoç, "Luminescence properties of defects in GaN," *J. Appl. Phys.*, vol. 97, no. 6, p. 061301, 2005.

Appendix A: Description of Research for Popular Publication

Optical properties of ultrathin QW: The size and shape matters

Huge advances in growing high quality nanostructures were achieved in recent years. These structures allow scientist and engineers from all around the world to create modern devices that, in most cases, outperform the corresponding solutions from previous generations. But why do we care so much about nano-sized structures? The answer is pretty simple: in most cases, the smaller device we can create, the better. Imagine yourself trying to choose the device that satisfies your needs, and you have two options to consider that are completely identical in terms of functionality. However, one is the size of a gallon of milk and the other is not larger than your cellphone. I believe most people will choose the smaller version even though the price of it might be a bit larger. The desire to make things smaller while maintaining their functionality pushed the size of individual components to the limit of atomic size objects. The words that are used for these objects are "nanostructures" or "quantum structures" and are basically saying that we are dealing with the atomic-size world that has its own nature and laws.

Most people can recall the experiment that involves gold nanoparticles with different size. While everyone knows the color of gold, the color of gold nanoparticles in the solution can be red, orange, or even blue. This easy experiment is used to demonstrate that nanoworld physics is quite different. Naturally, this leads to the unique physical properties that are exploited to design and fabricate the devices.

At the University of Arkansas Institute for Nanoscience and Engineering, the group of talented students under the supervision of Dr. Gregory Salamo strive to answer fundamental questions related to the nanoworld. Potentially, even a nano bit of new knowledge in this area can improve the parameters of the existing devices or develop the novel applications to push science forward.

This work focuses on the smallest possible size that any material can be in one direction – a one atomic layer thick quantum well (QW), which our group called an ultrathin QW. The research and laboratory capabilities of the research group led by Dr. Salamo made it possible to grow and study these challenging structures by utilizing various methods and analysis techniques. The main challenge is to answer the question: What is happening within ultrathin QWs? As for now, there are two justified models to structurally represent an ultrathin QW: the islands of one atomic layer height or vertical and lateral chemical intermixing. The schematics of both models are shown in Figure 1. This research exposed the possibility to show that the intermixing takes place by designing a special set of samples. Overall, the ultrathin QW

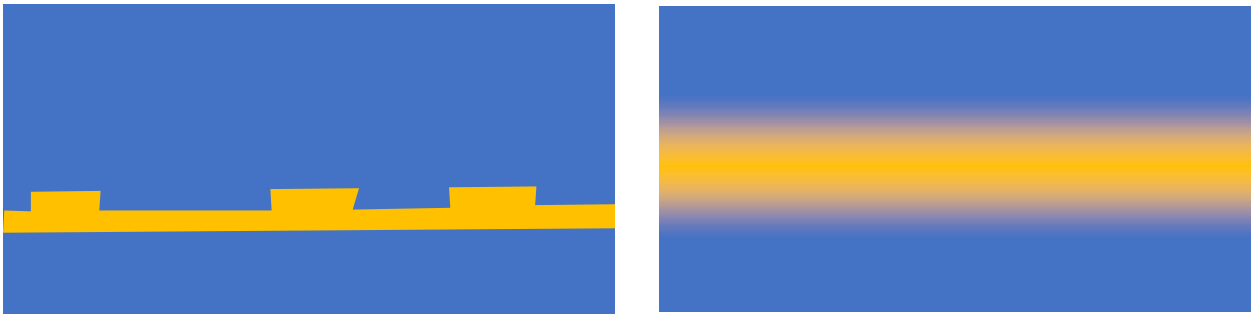

Figure 1. The schematic diagram of the two possible models of formation of ultrathin QW.

have been systematically investigated by changing the chemical depth profile as well as the total amount of material within the QW. It is amazing to realize that the unique and easy-to-use techniques for probing and controlling the chemical depth profile of material within QWs can be potentially exploited to design and fabricate modern devices.

Appendix B: Executive Summary of Newly Created Intellectual Property

Understanding and controlling the structural characteristics ultrathin quantum wells can have a substantial impact on improving the quality of the numerous existing devices as well as on developing promising novel devices based on the ultrathin QW incorporations into the base material. The key ideas presented in this dissertation and listed below are established based on the analysis of ultrathin In(Ga)As/GaAs and In(Ga)N/GaN QWs. However, the same concept can be applied to any relevant structures based on ultrathin layers incorporation.

1. The linear photoluminescence peak redshift occurred when the thickness of InAs/GaAs QW increased from 0.5 ML to 1.4 ML. Before this observation was explained using InAs islands coupling model. In this work indium and gallium intermixing model was introduced as a possible alternative. It was also shown that experimental optical data cannot provide enough support to confirm any of the mentioned models.
2. The ultrathin In(Ga)As/GaAs QW structures with the constant total amount of indium were designed for the first time to prove that indium and gallium intermixing is taking place. This was done by introducing the unique and non-destructive PL technique that involves experimental PL data supported by the effective bandgap simulation.
3. It was confirmed that the growth temperature plays the major role in In/Ga intermixing process. The quantitative parameters of intermixing were determined by the PL technique described above. For the first time it was shown that the indium content profile can be effectively modified by controlling the thickness of the low-temperature GaAs cap layer.

4. The study of ultrathin In(Ga)N/GaN QWs revealed that the emission energy can be controlled in range from 2.5 eV (496 nm) to 3.3 eV (376 nm) by increasing the growth temperature from 500 °C to 575 °C. It was shown by simulation that the total amount of indium incorporated to the QW can be changed in a wide range by only controlling the growth temperature, which was not previously reported.

Appendix C: Potential Patent and Commercialization Aspects of Listed Intellectual Property Items

C.1 Patentability of Intellectual Property

Some of the four key results of this dissertation could be potentially patented with the following reasoning:

1. The fact of structural model equivalency holds strictly physical interest and, therefore, cannot be patented in terms of possible applications or methods.
2. The described PL technique that involves experimental PL data supported by the effective bandgap simulation could be patented as a newly acquired characterization process.
3. The fact that growth temperature significantly affects In/Ga interdiffusion process was already described qualitatively and quantitatively and, therefore, cannot be patented. The possibility to control and modify the depth profile of indium by changing the thickness of low-temperature GaAs cap layer could potentially be patented.
4. The notion of total amount of indium incorporation change with the growth temperature cannot be patented at the current stage as no feasible practical applications are found.

C.2 Commercialization Prospects

The items listed as the intellectual property in this dissertation were considered of whether or not the item should be patented.

1. NA.

2. The described PL technique that involves experimental PL data supported by the effective bandgap simulation should not be patented since this method only simplifies the analysis of ultrathin QW structures and does not present a commercializable pathway.
3. The possibility to control and modify the depth profile of indium by changing the thickness of low-temperature GaAs cap layer should not be patented since at the current form it is only applicable to the single QW. The generalization of this method in case of superlattice, which present a commercialization value, requires additional research.
4. NA.

C.3 Possible Prior Disclosure of IP

All of the items listed in the IP were discussed and evaluated at research meetings and public forums. All items are either published or planned to be published in peer reviewed journals.

1. The fact of structural model equivalency and optical analysis of ultrathin In(Ga)As/GaAs QWs was published in Journal of Applied Physics 124, 235303 (2018).
2. The described PL technique that involves experimental PL data supported by the effective bandgap simulation will be published in near future.
3. The possibility to control and modify the depth profile of indium by changing the thickness of low-temperature GaAs cap layer will be published together with the previous item.

4. The notion of the total amount of indium incorporation change with the growth temperature is currently in the planning stage to be published.

Appendix D: Broader Impact of Research

D.1 Applicability of Research Methods to Other Problems

Research methods presented in this dissertation can and should be applied to other nanostructures exploiting quantum confinement effect in their basis. In particular, the unique and non-destructive PL technique that involves experimental PL data supported by the effective bandgap simulation provides a general recipe of materials intermixing within the QW. Additionally, the sample design that is based on the constant total amount of the key element provides a general notion of how to precisely determine and control the depth content profile. The precise description of the dependence of the emission energy on the shape of the depth profile as well as the total amount of material incorporated in the QW can potentially be utilized for bandgap engineering.

D.2 Impact of Research Results on U.S. and Global Society

The numerous applications that involve ultrathin QWs as a basis include lasers, solar cells, photodetectors, and light emitting diodes. However, the full realization of the physical potential of ultrathin QW-based structures remains in vain. This dissertation focuses on the ground understanding of the effect of structural characteristics of ultrathin layers on the emission properties of the structure. The author believes that this potentially can lead to the more accurate design of ultrathin QW structures with desired characteristics. In the long run, the intellectual property generated in this study can provide substantial improvement for existing devices or develop novel applications with the physical properties that are unreachable at the current moment.

D.3 Impact of Research Results on the Environment

The research methods and structure growth procedures that have been used in this dissertation do not have any negative environmental impact. The MBE growth of As-based structures is a closed-cycle process and, therefore, does not negatively affect the environment. The end product is the solid structure mostly consisting of GaAs and since it is not in a powder form, it is safe for health. Solving the 'green gap' problem can greatly reduce the power consumption for numerous devices.

Appendix E: Microsoft Project for PhD MicroEP Degree Plan

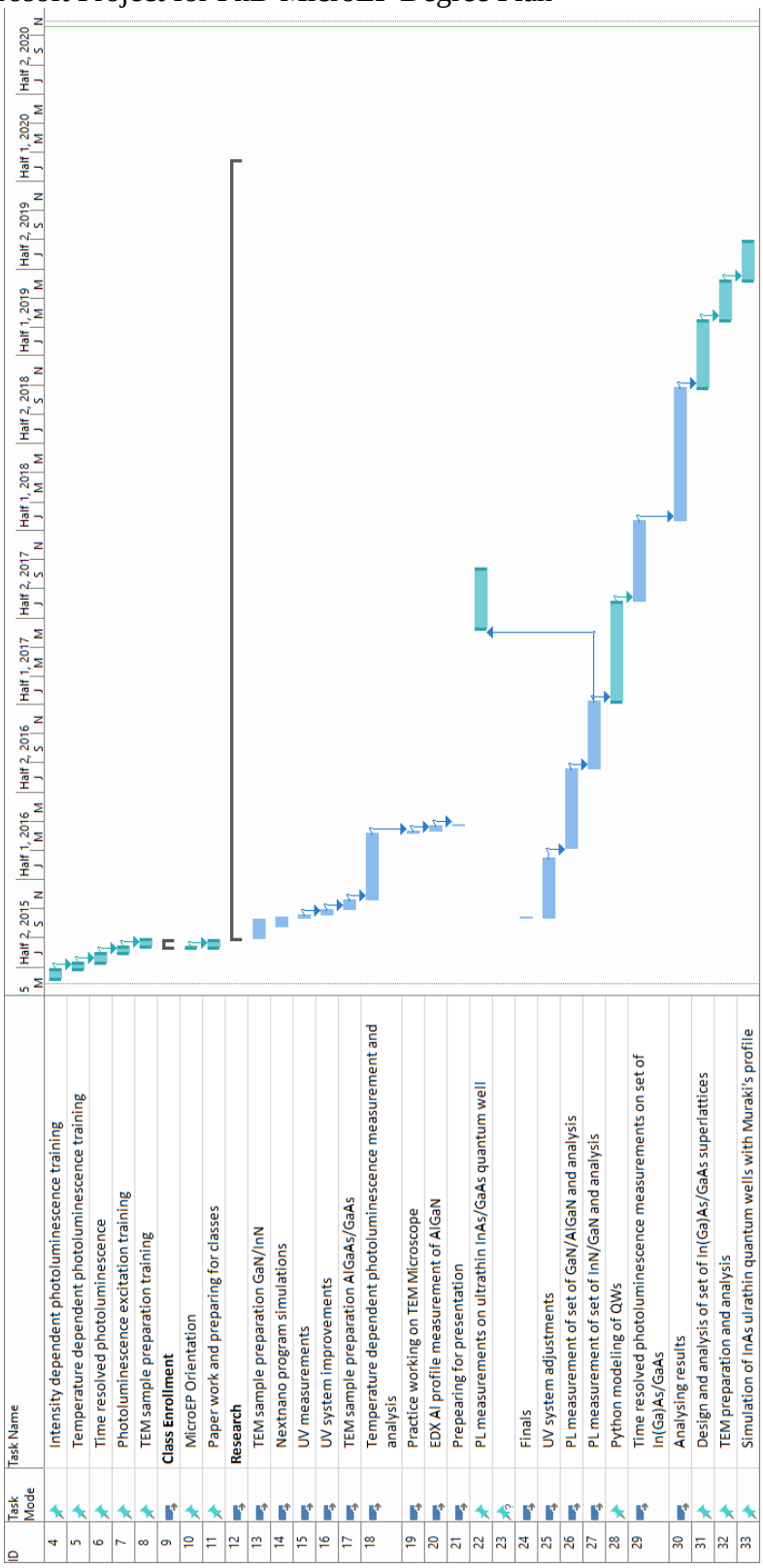

ID	Task Mode	Task Name
34		Article writing
35		**Read Publications**
36		Free exiton emition in GaN
37		Band parameters for III-V compound semiconductors and their alloys
38		InN/GaN multiple quantum well properties
39		AlN/GaN superlattice TEM and analysis
40		InAs/GaAs optoelectronic measurements and analysis
41		k.p method for determining properties of heterostructures
42		**Candidacy Exam**
43		Written Candidacy Exam
44		Oral Presentation Prep
45		Oral Presentation
46		**Dissertation writing**
47		Chapter 1: Background of area
48		Chapter 2: Description of Experiment
49		Chapter 3: Results
50		Chapter 4: Analysis
51		Chapter 5: Conclusion
52		Appendix
53		**END GAME**
54		Review by Major Professor
55		Correct issues found
56		Final approval by Major Professor
57		Send Title, Abstract & Scheduling Information to MicroEP
58		Send dissertation to committee members
59		Public presentation
60		Defense

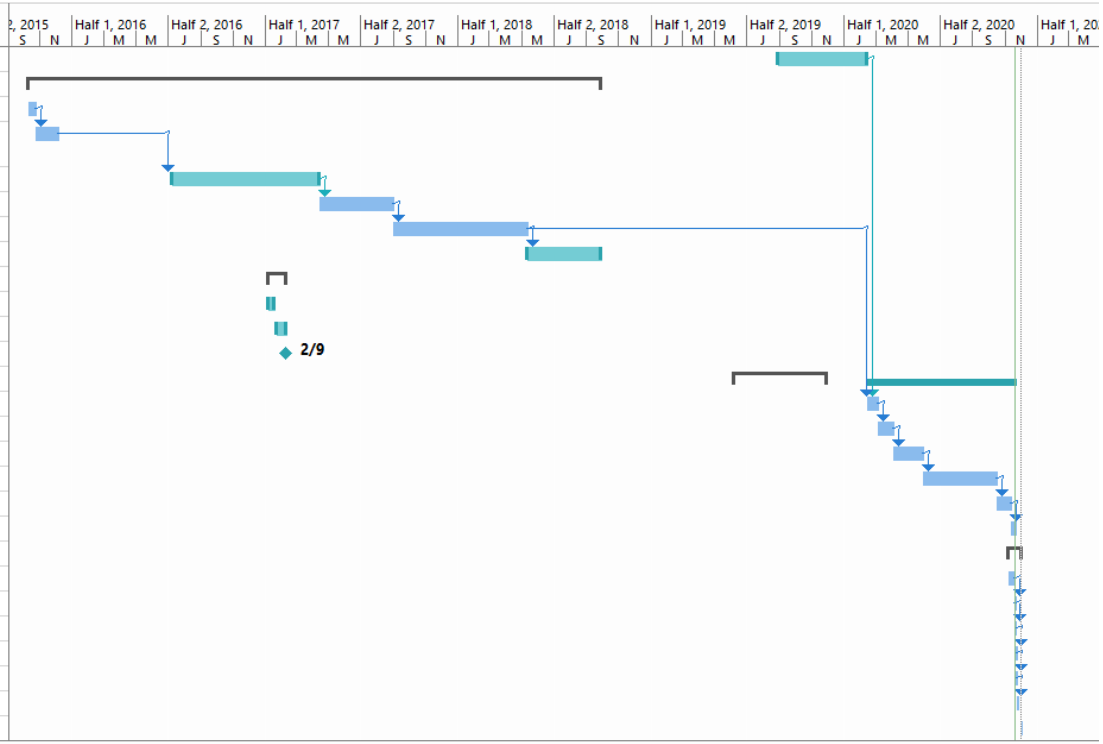

Appendix F: Identification of All Software Used in Research and Dissertation Generation

Computer #1:

Model Number: Dell Optiplex 3020
Serial Number: 1W5Q382
Location: NANO109
Owner: Yurii Maidaniuk

Software #1:

Name: Microsoft Office 365
Purchased by: University of Arkansas Site License

Software #2:

Name: NextNano
Purchased by: Prof. Morgan Ware

Software #3:

Name: OriginPro 2020
Purchased by: Prof. Morgan Ware

Appendix G: All Publications Published, Submitted and Planned

1. Kondratenko, S, Kozak, O, Rozouvan, S, Mazur, Y, Maidaniuk, Y, Wu, J, Wu, S, Wang, Z, Chan, S, Kim, D, others. "Carrier dynamics and recombination in silicon doped InAs/GaAs quantum dot solar cells with AlAs cap layers". Semiconductor Science and Technology 2020; 35(11):115018.

2. Su, L, Liang, B, Wang, Y, Yuan, Q, Guo, Q, Wang, S, Fu, G, Huffaker, D, Mazur, Y, Ware, M, others. "Abnormal photoluminescence for GaAs/Al0. 2Ga0. 8As quantum dot-ring hybrid nanostructure grown by droplet epitaxy". Journal of Luminescence 2018; 195:187–192.

3. Onno, A, Wu, J, Jiang, Q, Chen, S, Tang, M, Maidaniuk, Y, Benamara, M, Mazur, Y, Salamo, G, Harder, NP, others. "Al0. 2Ga0. 8As solar cells monolithically grown on Si and GaAs by MBE for III-V/Si tandem dual-junction applications". Energy Procedia 2016; 92:661–668.

4. Guo, D, Jiang, Q, Tang, M, Chen, S, Mazur, Y, Maidaniuk, Y, Benamara, M, Semtsiv, M, Masselink, W, Salamo, G, others. "Two-colour In0. 5Ga0. 5As quantum dot infrared photodetectors on silicon". Semiconductor Science and Technology 2018; 33(9):094009.

5. Kolomys, O, Tsykaniuk, B, Strelchuk, V, Naumov, A, Kladko, V, Mazur, Y, Ware, M, Li, S, Kuchuk, A, Maidaniuk, Y, others. "Optical and structural study of deformation states in the GaN/AlN superlattices". Journal of Applied Physics 2017; 122(15):155302.

6. Li, C, Maidaniuk, Y, Kuchuk, A, Mazur, Y, Benamara, M, Ware, M, Salamo, G. "Effect of indium accumulation on the growth and properties of ultrathin In (Ga) N/GaN quantum wells". Materials & Design 2020; 190:108565.

7. Wang, Y, Sheng, X, Guo, Q, Li, X, Wang, S, Fu, G, Mazur, Y, Maidaniuk, Y, Ware, M, Salamo, G, others. "Photoluminescence Study of the Interface Fluctuation Effect for InGaAs/InAlAs/InP Single Quantum Well with Different Thickness". Nanoscale Research Letters 2017; 12(1):229.

8. Kim, D, Tang, M, Wu, J, Hatch, S, Maidaniuk, Y, Dorogan, V, Mazur, Y, Salamo, G, Liu, H. "Si-doped InAs/GaAs quantum-dot solar cell with AlAs cap layers". IEEE Journal of Photovoltaics 2016; 6(4):906–911.

9. Wu, J, Jiang, Q, Chen, S, Tang, M, Mazur, Y, Maidaniuk, Y, Benamara, M, Semtsiv, M, Masselink, W, Sablon, K, others. "Monolithically integrated InAs/GaAs quantum dot mid-infrared photodetectors on silicon substrates". ACS Photonics 2016; 3(5):749–753.

10. Kumar, R, Maidaniuk, Y, Kuchuk, A, Saha, S, Ghosh, P, Mazur, Y, Ware, M, Salamo, G. "Excitation intensity and thickness dependent emission mechanism from an ultrathin InAs layer in GaAs matrix". Journal of Applied Physics 2018; 124(23):235303.

11. Saha, S, Kumar, R, Kuchuk, A, Alavijeh, M, Maidaniuk, Y, Mazur, Y, Yu, SQ, Salamo, G. "Crystalline GaAs Thin Film Growth on a c-Plane Sapphire Substrate". Crystal Growth & Design 2019; 19(9):5088–5096.

12. Stanchu, H, Kuchuk, A, Mazur, Y, Li, C, Lytvyn, P, Schmidbauer, M, Maidaniuk, Y, Benamara, M, Ware, M, Wang, Z, others. "Local strain and crystalline defects in GaN/AlGaN/GaN (0001) heterostructures induced by compositionally graded AlGaN buried layers". Crystal Growth & Design 2018; 19(1):200–210.

13. Yuan, Q, Liang, B, Luo, S, Wang, Y, Yan, Q, Wang, S, Fu, G, Mazur, Y, Maidaniuk, Y, Ware, M, others. "Type-II GaSb quantum dots grown on InAlAs/InP (001) by droplet epitaxy". Nanotechnology 2020; 31(31):315701.

14. Chen, W, Deng, Z, Guo, D, Chen, Y, Mazur, Y, Maidaniuk, Y, Benamara, M, Salamo, G, Liu, H, Wu, J, others. "Demonstration of InAs/InGaAs/GaAs quantum dots-in-a-well mid-wave infrared photodetectors grown on silicon substrate". Journal of Lightwave Technology 2018; 36(13):2572–2581.

15. Ghosh, P, Stanchu, H, Maidaniuk, Y, Sarollahi, M, Aldawsari, M, Kuchuk, A, Mazur, Y, Salamo, G, Ware, M. "Investigation of the Structural and Optical Properties of Compositionally V-Graded Strained InxGa1–xN Layers". physica status solidi (b) 2020; 257(4):1900591.

16. Onno, A, Wu, J, Jiang, Q, Chen, S, Tang, M, Maidaniuk, Y, Benamara, M, Mazur, Y, Salamo, G, Harder, NP, others1.7 eV Al0. 2Ga0. 8As solar cells epitaxially grown on silicon by SSMBE using a superlattice and dislocation filters. In Physics, Simulation, and Photonic Engineering of Photovoltaic Devices V 2016 (pp. 974310).

17. Wang, Y, Sheng, X, Yuan, Q, Guo, Q, Wang, S, Fu, G, Liang, B, Huffaker, D, Mazur, Y, Maidaniuk, Y, others. "Carrier dynamics in hybrid nanostructure with electronic coupling from an InGaAs quantum well to InAs quantum dots". Journal of Luminescence 2018; 202:20–26.

18. Stanchu, H, Kuchuk, A, Lytvyn, P, Mazur, Y, Ware, M, Maidaniuk, Y, Benamara, M, Wang, Z, Salamo, G. "Kinetically controlled transition from 2D nanostructured films to 3D multifaceted InN nanocrystals on GaN (0001)". CrystEngComm 2018; 20(11):1499–1508.

19. Li, C, Maidaniuk, Y, Kuchuk, A, Shetty, S, Ghosh, P, White, T, Morgan, T, Hu, X, Wu, Y, Ware, M, others. "Kinetically controlled indium surface coverage effects on PAMBE-growth of InN/GaN (0001) quantum well structures". Journal of Applied Physics 2018; 123(19):195302.